

INAUGURAL-DISSERTATION

zur

Erlangung der Doktorwürde

der

Naturwissenschaftlich-Mathematischen Gesamtfakultät

der

Ruprecht-Karls-Universität

Heidelberg

vorgelegt von

Md. Nuruzzaman Khan Hira, M.Sc.

aus Dhaka, Bangladesch

Tag der mündlichen Prüfung: 07.02.2014

DISSERTATION

Submitted to the
Combined Faculties of Natural Sciences and Mathematics
Ruprecht-Karls-University Heidelberg, Germany
for the degree of
Doctor of Natural Sciences (Dr. rer. nat.)

Presented by

Md. Nuruzzaman Khan Hira, M.Sc.

Born in Dhaka, Bangladesh

Oral examination: 07.02.2014

Chemical Lithography with Monomolecular Templates

This dissertation was carried out at the
Department of Applied Physical Chemistry

Referees

apl. Prof. Dr. Michael Zharnikov

Prof. Dr. Petra Tegeder

Kurzfassung

Motivation für diese Arbeit was die Entwicklung einer neuen Präparationsmethode, um eine Einzelstrang-DNA (engl.: *single stranded DNA*, ssDNA) innerhalb eines biokompatiblen Templats zu immobilisieren und zudem ssDNA-Muster beliebiger Form und Größe herzustellen. Als Ansatz wurde eine strahlungsinduzierte Austauschreaktion (engl.: *irradiation promoted exchange reaction*, IPER) im Rahmen des konzepts der Chemischen Lithographie verwendet. IPER ermöglicht es mittels Elektronenbestrahlung, das Ausmaß der Austauschreaktion zwischen einer primären, das Substrat bedeckenden selbstorganisierten Monoschicht (engl.: *self-assembled monolayer*, SAM) und einem molekularen Substituent je nach Dosis zu steuern. Physikalisch bedeutet IPER die Erzeugung von chemischen und strukturellen Defekten in dem primären SAM, die die Austauschreaktion fördern. In dieser Arbeit wurde der IPER Ansatz auf eine kontrollierte und ortsspezifische Immobilisierung von ssDNA auf Au(111)-Substraten erweitert. Um eine unspezifische Adsorption außerhalb der ssDNA bedeckten Bereiche zu verhindern, wurde als Ausgangsmatrix eine biokompatible Oligoethylenglykol-substituierte Alkanthiol (OEG-AT) Monolage verwendet.

Im ersten Abschnitt wurden thiol-terminierte ssDNA als Substituenten eingesetzt. IPER mit diesen Substituenten und einem OEG-AT-SAM als Vorlage führten zu homogen gemischten ssDNA/OEG-AT Filmen der gewünschten Zusammensetzung, die anhand der eingestellten Dosis angepasst werden konnte. Basierend auf diesen Ergebnissen wurde IPER mit Elektronenstrahlolithographie (EBL) verwendet, was die Herstellung komplexer ssDNA-Muster mit der gewünschten Form und Nanometergröße (bis zu 25-50 nm) innerhalb der biokompatiblen Matrix erlaubte. Diese Muster wurden dann als Vorlagen für die oberflächeninitiierte, enzymatische Polymerisation (SIEP) eingesetzt, was die Präparation von komplexen, räumlichen ssDNA Bürsten erlaubte.

Ausgehend von den genannten Ergebnissen wurde die Möglichkeit überprüft, IPER mit kommerziell verfügbaren ssDNA-Disulfid Substituenten durchzuführen. Zunächst wurde eine Studie unter Verwendung eines Referenzfilms aus einem nicht-substituierten AT auf Gold und einem symmetrischen COOH-substituierten Dialkyldisulfid als Substituent durchgeführt. Dabei wurde festgestellt, dass IPER mit Disulfid-Substituenten in der gleichen Weise wie mit Thiolen durchgeführt werden kann. Es konnte gezeigt werden, dass die Kinetik der Austauschreaktion in beiden Fällen ähnlich ist, wenn auch das Ausmaß der Reaktion bei den Disulfiden geringer war. Dennoch konnten gemischten SAMs mit einer Konzentration der substituenten Spezies von bis zu 60% hergestellt werden.

Basierend auf diesen Ergebnissen wurde die Möglichkeit verschiedener symmetrischer wie asymmetrischer ssDNA-Disulfide als Substituenten für IPER untersucht, wobei beide Systeme sich als geeignet für die IPER erwiesen. Die asymmetrischen Disulfide zeigten ähnlich hohe Wirkungsgrade, während die Effizienz der symmetrischen Disulfide insbesondere bei niedrigen Bestrahlungsdosen ($< 0,6 \text{ mC/cm}^2$) deutlich niedriger war.

Die Verwendung von IPER erfordert Hochvakuum und im Fall komplexer Strukturierung aufwändige Versuchsaufbauten wie Rasterelektronenmikroskop. Daher wurde in einem weiteren Abschnitt UV-Licht als Initiator für die Austauschreaktion zwischen der primären OEG-AT Matrix und den ssDNA Substituenten eingesetzt. UV-Licht wurde zur homogenen und lithographischen Strukturierung, zur Herstellung gemischter ssDNA/OEG-AT Filme und ssDNA Muster eingebettet in eine biokompatible OEG-AT Matrix verwendet. Auch hierbei konnte die Zusammensetzung der gemischten Filme durch die Wahl der Dosis eingestellt werden. Es wurde auch gezeigt, dass das UV-Licht unterschiedlicher Wellenlängen (254 oder 365 nm) neue Möglichkeiten für die Lithographie eröffnet.

Zuletzt wurde eines der Systeme, ssDNA Polymerbürsten gekoppelt an ein monomolekulares ssDNA Templat, im Rahmen dieser Arbeit detailliert untersucht. Eine Kombination von mehreren komplementären spektroskopische Techniken wurde verwendet, um die chemische Integrität, Reinheit und molekulare Ausrichtung dieser mittels SIEP hergestellten Objekte zu untersuchen. Die Spektren der

Polymerbürsten waren nahezu identisch mit denen der monomolekularen ssDNA Vorläufer und wiesen keine Spuren von Verunreinigungen auf. Neben der wohldefinierten chemischen Integrität und dem kontaminationsfreien Charakter, zeigten die Bürsten eine vergleichsweise hohe Orientierungsordnung, mit vorzugsweise aufrechter Ausrichtung der einzelnen Stränge.

Die entwickelten Herstellungsmethoden bieten die Möglichkeit, ssDNA/OEG-AT Filme und Muster für die Bindung und den Nachweis der komplementär ssDNA Stränge sowie für die Erkennung von DNA-bindenden Proteinen zu präparieren, was unter anderem eine Grundlage für Sensorfabrikation bildet. Ferner dienen sie als vielseitige Plattform für Nanofabrikation, wie anhand der komplexen ssDNA Bürste in dieser Arbeit demonstriert wurde.

Abstract

The motivation behind this work was the development of a new approach to immobilize single stranded DNA (ssDNA) within a biorepulsive template in a broad range of compositions and to fabricate ssDNA patterns of arbitrary shape and size imbedded into biorepulsive matrix. This approach relies on so called irradiation promoted exchange reaction (IPER) within the general concept of Chemical Lithography. The key idea of IPER is tuning the extent of the exchange reaction between the primary self-assembled monolayer (SAM) covering the substrate and a molecular substituent in solution by electron irradiation, which allows fabrication of binary mixed SAMs of variable compositions depending on the selected dose. The physics behind this method is the creation of chemical and structural defects in the primary SAM, which promote the exchange reaction. Within this thesis work, the IPER approach was extended to a specific task of controlled and site specific immobilization of ssDNA on Au (111) substrate. To suppress the nonspecific adsorption events beyond the seeded ssDNA species, a biorepulsive oligo(ethylene glycol) substituted alkanethiolate (OEG-AT) monolayer was used as the primary matrix for the exchange reaction.

In the first sub-project within this framework, thiolated ssDNA were used as substituents. IPER with these substituents and an OEG-AT monolayer as template resulted in homogeneously mixed ssDNA/OEG-AT films of desired composition that could be precisely adjusted by selected dose. Based on these results, IPER was combined with electron beam lithography (EBL), which allowed fabricating complex ssDNA patterns of desired shape and nanosize (down to 25-50 nm) in the biorepulsive matrix. These patterns were used as templates for surface-initiated enzymatic polymerization (SIEP), which resulted sculpturing of complex 3D ssDNA brush patterns.

Inspired by the above results, a possibility to perform IPER with a disulfide ssDNA substituent was tested, in view of the commercial availability of such molecules. Before these experiments, a reference study utilizing a film of a non-substituted AT on gold as the primary template and symmetric $-COOH$ substituted dialkyldisulfide as the substituent was performed as an independent sub-project. It was found that IPER could be successfully conducted with disulfide substituents in the same manner as in the case of thiols. The kinetics of the exchange reaction was found to be similar in both cases but the extent of this reaction was smaller for disulfides. Nevertheless, mixed SAMs with a concentration of the substituent-stemming species up to 60% could be prepared.

Based on the above results, the ability of different disulfide ssDNA precursors to serve as substituents in IPER was demonstrated for both asymmetric and symmetric ssDNA disulfides. Both these precursors were found to be suitable for the promoted exchange reaction. The asymmetric disulfide exhibited similar, quite high efficiency as thiolated ssDNA, while the efficiency of the symmetric disulfide was noticeably lower, especially at low irradiation doses ($< 0.6 \text{ mC/cm}^2$).

The application of the IPER approach requires high vacuum and, in the case of advanced patterning, relies on complex experimental setups such as scanning electron microscope with pattern generator system. Consequently, in a further sub-project, not the electrons but UV light was used as the primary tool for the promotion of the exchange reaction between the OEG-AT matrix and ssDNA substituents. The UV light was employed both in homogeneous and lithographic fashion resulting in the fabrication of mixed ssDNA/OEG-AT films and ssDNA patterns in the biorepulsive OEG-AT background, respectively. Significantly, the composition of the mixed films could be precisely adjusted in almost entire composition range by the UV dose. It was also demonstrated that the procedure can be performed with UV light of different wavelengths (254 or 365 nm), which opens new possibilities for lithography.

Finally, one of the novel systems addressed within this thesis, viz. ssDNA brushes grown on the monomolecular ssDNA templates, was studied in more detail. A combination of several complementary

spectroscopic techniques was employed to probe the chemical integrity, purity and possible internal alignment of these brushes prepared by SIEP. The spectra of these brushes were found almost identical to those of the monomolecular ssDNA precursor, with no unambiguous traces of contamination. Apart from the well-defined chemical integrity and contamination-free character, the brushes were found to have comparably high degree of orientational order, with preferable upright orientation of individual strands.

The developed methodology opens the way to fabricate ssDNA/OEG-AT films and patterns, which can be used for binding and detection of their complementary ssDNA targets and recognition of DNA binding proteins, providing a basis for sensor fabrication. Also they can serve as a versatile platform for nanofabrication, as demonstrated by the preparation of the complex ssDNA brush patterns.

List of Publications related to this work

Journals articles

Khan, M. N.; Tjong, V.; Chilkoti, A.; Zharnikov, M. Fabrication of ssDNA/oligo (ethylene glycol) Monolayers and Complex Nanostructures by Irradiation Promoted Exchange Reaction. *Angewandte Chemie International Edition* **51**, 10303-10306 (2012).

Khan, M. N.; Zharnikov, M. Irradiation Promoted Exchange Reaction with Disulfide Substituents. *The Journal of Physical Chemistry C* **117**, 14534-14543 (2013).

Khan, M. N.; Tjong, V.; Chilkoti, A.; Zharnikov, M. Spectroscopic Study of a DNA Brush Synthesized in Situ by Surface Initiated Enzymatic Polymerization. *The Journal of Physical Chemistry B* **117**, 9929-9938 (2013).

Khan, M. N.; Zharnikov, M. Fabrication of ssDNA/Oligo(ethylene glycol) Monolayers and Patterns by Exchange Reaction Promoted by Ultraviolet Light Irradiation. *The Journal of Physical Chemistry C* **117**, 24883-24893 (2013).

Khan, M. N.; Zharnikov, M. Fabrication of ssDNA/Oligo(ethylene glycol) Monolayers by Promoted Exchange Reaction with Thiol and Disulfide Substituents. *The Journal of Physical Chemistry C*, submitted.

Weber, T.; Meyebroeker, N.; Khan, M. N.; Zharnikov, M.; Terfort, A. UV-Mediated Tuning of Surface Biorepulsivity in Aqueous Environment. *Angewandte Chemie International Edition*, submitted.

Conference proceedings

Khan, M. N.; Tjong, V.; Chilkoti, A.; Zharnikov, M. Programming of Complex 3D DNA Nanostructures on Chemical Template and Extension by Enzymatic Polymerization. Proceedings, 19th International Vacuum Congress, Paris, France, Sep 9-13, 2013.

Khan, M. N.; Zharnikov, M. Complex Sculpturing 3D DNA Nanostructures on Protein Repelling Matrix Using Electron Beam Chemical Nanolithography. 2nd International Conference of Biosensors & Bioelectronics, Chicago, USA, June 17-19, 2013, *J. Biosens. Bioelectron*, 4 (3), p 125.

Khan, M. N.; Zharnikov, M. Novel Approach to the Fabrication of Mixed Monomolecular Films and Chemical Patterns. Proceedings, DPG Spring Meetings, University Regensburg, Germany, March 10-15, 2013, p 368.

Khan, M. N.; Tjong, V.; Chilkoti, A.; Zharnikov, M. New Approach to the Fabrication of ssDNA/Oligo(ethyleneglycol) Monolayers and Complex Nanostructures. Proceedings, DPG Spring Meetings, University Regensburg, Germany, March 10-15, 2013, p 375.

Contents

1 Introduction	1
2 Theoretical background	7
2.1 Surfaces in nanoscience.....	7
2.2 SAMs as component of nanoscience and nanotechnology.....	7
2.2.1 Protein-resistant SAMs	9
2.2.2 Mixed SAMs	10
2.3 Patterning strategies.....	10
2.3.1 E-Beam chemical lithography	12
2.4 Surface initiated polymerization	13
2.4.1 Controlled / living radical polymerization.....	13
2.4.2 Atom transfer radical polymerization.....	14
2.4.3 Surface initiated enzymatic polymerization	16
3. Characterization methods	17
3.1 X-ray photoelectron spectroscopy	17
3.1.1 Basics.....	17
3.1.2 Construction of apparatus	18
3.1.3 Surface sensitivity analysis.....	20
3.1.4 Determination of the stoichiometric composition	20
3.1.5 Determination of layer thickness of thin film	21
3.2 Near edge X-ray absorption fine structure spectroscopy	22
3.2.1 Principles.....	22
3.2.2 Angular dependence of NEXAFS resonance intensity.....	23
3.3 Spectral ellipsometry	24
3.4 Scanning electron microscopy.....	26
3.5 Atomic force microscopy	29
3.5.1 Basic principles.....	29
3.5.2 Imaging modes.....	29
3.6 Contact angle goniometry	30

4. Fabrication of ssDNA/oligo(ethylene glycol) monolayers and complex nanostructures by irradiation promoted exchange reaction	33
4.1 Preparation and characterization procedures.....	34
4.1.1 Preparation of mixed A25SH/EG3 films and patterns by IPER-EBL.....	34
4.1.2 Hybridization experiments.....	34
4.1.3 Fabrication of ssDNA brushes.....	35
4.2 Results and discussion	35
4.2.1 Characterization of the A25SH/EG3 films: XPS	35
4.2.2 Characterization of the A25SH/EG3 films: NEXAFS spectroscopy	36
4.2.3 Hybridization ability of mixed A25SH/EG3 films.....	37
4.2.4 Characterization of ssDNA Brush	38
4.2.5 ssDNA patterns on EG3 templates.....	39
4.3 Conclusions	41
5. Irradiation promoted exchange reactions with disulfide substituents	43
5.1 Preparation and characterization procedures.....	43
5.1.1 Preparation of monolayers on Au	43
5.1.2 Irradiation promoted exchange reaction and EBL	44
5.1.3 Fabrication of polymer brushes by SI-ATRP	44
5.2 Results and discussion	45
5.2.1 Outcome and kinetics of IPER	45
5.2.2 IPER with a disulfide bearing an initiator for SIP.....	47
5.2.3 SIP on IPER-generated chemicals templates.....	49
5.3 Conclusions	52
6. Fabrication of ssDNA/oligo(ethylene glycol) monolayers by promoted exchange reaction with disulfide substituents.....	53
6.1 Preparation and characterization procedures.....	53
6.1.1 Preparation of disulfide DNA films on Au	53
6.1.2 IPER with symmetric and asymmetric disulfides DNA precursors.....	53
6.2 Results and Discussion.....	54
6.2.1 A25S films.....	54
6.2.2 Outcome of IPER	57
6.3 Conclusions	60

7. Fabrication of ssDNA/Oligo(ethylene glycol) monolayers and patterns by exchange reaction promoted by ultraviolet light irradiation.....	61
7.1 Preparation and characterization procedures.....	61
7.1.1 Preparation of mixed A25SH/EG3 films by UVPER	61
7.1.2 Fabrication of ssDNA nanostructures by UVPER.....	62
7.1.3 Fabrication of ssDNA brushes	62
7.2 Results and Discussion.....	62
7.2.1 Extent of UVPER	63
7.2.2 Characterization of the A25SH/EG3 films: XPS	64
7.2.3 Characterization of the A25SH/EG3 films: NEXAFS spectroscopy	66
7.2.4 UVPER based patterning	69
7.2.5 Characterization of ssDNA brushes.....	70
7.3 Conclusions	70
8. Spectroscopic study of ssDNA brushes prepared on ssDNA templates	73
8.1 Preparation and characterization procedures.....	73
8.1.1 Preparation of adenine powder film.....	73
8.1.2 Fabrication of ssDNA brushes on ssDNA templates	74
8.1.3 Preparation of ssDNA patterns	74
8.2 Results and discussion	74
8.2.1 Characterization of ssDNA brush by XPS	75
8.2.2 Characterization of ssDNA brush by NEXAFS spectroscopy.....	78
8.2.3 Brush thickness and density effects.....	81
8.2.4 Characterization of Brush patterns.....	82
8.3 Conclusions	83
9. Summary and outlook.....	85
10. Experimental part	89
10.1 Preparation of self-assembled monolayers on Au	89
10.1.1 Substrates and chemicals.....	89
10.1.2 Preparation of EG3 and A25SH monolayers	90
10.1.3 Preparation of DDT, MUDA, DTUDA, and DTBUD monolayers.....	90
10.2 Preparation of two components monolayer on Au.....	90
10.2.1 Preparation of A25SH/EG3 films by IPER.....	90
10.2.2 Preparation of A25SH/EG3 films by UVPER	91
10.3 Fabrication of patterns on chemical templates.....	92

10.3.1 Fabrication of nanostructures by EBL	92
10.3.2 Fabrication of nanostructures by UVPER	92
10.4 Fabrication of Polymer Brushes.....	93
10.4.1 pNIPAAm brushes	93
10.4.2 pHEMA brushes.....	93
10.4.3 pEGDMA brushes	94
10.4.4 ssDNA brushes	94
10.5 Analytical techniques.....	95
10.5.1 Spectral Ellipsometry	95
10.5.2 Contact angle goniometry.....	95
10.5.3 AFM Measurements.....	95
10.5.4 Scanning electron microscopy	95
10.5.5 Optical microscopy.....	95
10.5.6 X-ray photoelectron spectroscopy.....	95
10.5.7 NEXAFS spectroscopy.....	97
List of abbreviations	99
Bibliography	101
Acknowledgement.....	119
Financial Supports	121

1 Introduction

There is a significant demand to miniaturize devices, in order to provide intelligent and multifunctional services in most efficient and less expensive way. In particular, the capability to generate small structures has become crucial for microelectronics industry and many other fields of modern technology. The major technique to meet these demands is lithography, including photolithography,¹ interference lithography,² UV and extreme UV lithography,³⁻⁴ X-ray lithography,⁵ electronbeam lithography,⁶ nanoimprint lithography,⁷ microcontact printing,⁸ and scanning probe methods (for example, dip-pen nanolithography, “constructive” nanolithography, and near field photolithography).⁹⁻¹¹

Among these methods, photolithography is probably the most popular approach for micro-fabrication,¹²⁻¹³ especially in semiconductor industry, since its invention in 1959. Most of the integrated circuits are currently made by this technology,¹⁴ and most recently, also by popular immersion lithography¹⁵⁻¹⁶ (a sort of a resolution enhanced photolithography approach). Today, it is possible to integrate more than 2 billion transistors of a structure size of 32 nm on a chip. Consequently, continuous shrinking of feature sizes and other technological restrictions pose new challenges on photolithography. In this contest, X-ray lithography⁵ and electron-beam lithography (EBL)⁶ are currently discussed to realize further miniaturization. These lithographic tools are capable of much higher lateral resolution (down to a few nanometers).¹⁷ In particular, EBL¹⁸ developed in the 1960s using existing scanning electron microscope (SEM) technology, can be performed both in proximity printing geometry using a stencil mask and by direct writing with a focused electron beam as it scans line by line across a resist-coated substrate, with a lateral resolution limited mostly by the diameter of the beam. Of course, EBL is not suited well for the chip mass production as it requires expensive instruments, ultra high vacuum for operation, and the inherently serial patterning, but it is the only technique to create sub-microscale patterns with nanometre precision and it is also popular in other areas such as research, micro-optics, cell receptors, biotechnology, micro reactors, biochips, micro sensor fabrication, etc.

Within the EBL approach, the resist material is one of the limiting factors for the lateral resolution, since it is not only determined by the diameter of the electron beam, but also by the thickness of the resist film, due to so-called proximity effect. As a result of this effect, mediated by scattered and backscattered electrons, the size of the effectively exposed area is always larger than the diameter of the electron beam. The higher the energy of the electron beam, the larger distortion by backscattered electrons. On the other hand, lowering the energy of electron beam will decrease its focusability and, result in a lower penetration depth into the resist material which will be no longer completely exposed. In particular, the minimum film thickness for the standard PMMA resist deposited by spin-coating is ~50 nm, which requires an electron energy of at least 5 keV and, because of the proximity effect, results in a resolution of about 100 nm.¹⁹ In order to produce smaller structures by EBL, a completely different resist material must be used. The introduction of such materials, complementary to

the currently used photopolymers can improve the current technology as well as enable the development of principally new lithographic approaches.

In this context, promising resist materials are self-assemble monolayers (SAMs) which are a perfect platform for the micro- and nanostructure fabrication due to the possibility to adjust their performance as resists, nanometer thickness, and the molecular size of their elements. Molecules capable to build SAMs consist usually of three major parts, viz. a head group that anchors the molecule to the substrate, a tail group that defines the surface properties of the entire system, and a spacer connecting the head and tail groups and facilitating the self-assembly process (figure 1.1).²⁰⁻²¹ Within this general architecture, flexible combination of different functional moieties is possible depending on a specific application, including a broad variety of different tail groups. A certain tail group means specific chemical and physical properties of the surface or interface, which are redefined, as compared to the original substrate, upon the SAM formation. An additional flexibility appears if the molecules bearing different tail groups are mixed in a SAM. This allows tuning a specific property between the ultimate values associated with both groups; such a tuning can be easily performed by varying the portions of both constituents in the mixed monolayer.

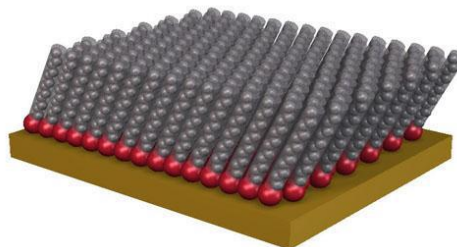


Figure 1.1 Self-assembled monolayer on a gold substrate (yellow) with a thiolate head group (red), a spacer group (gray) and an optional end group.

In addition to the standard approaches to prepare mixed SAMs, such as coadsorption,²²⁻²⁹ adsorption of asymmetric two-chain molecules (e.g., disulfides),³⁰⁻³³ or subsequent adsorption of both components,³⁴⁻³⁶ Zharnikov and coworkers developed recently a new technique named irradiation-promoted exchange reaction (IPER).³⁷⁻³⁸ The key idea of this method is tuning the extent of the exchange reaction between the primary SAM covering the substrate and a potential molecular substituent by electron irradiation, which allows fabrication of binary mixed SAMs of variable composition depending on the selected dose. The physics behind this method is the creation of irradiation-induced, chemical and structural defects in the primary SAM, which promote the subsequent exchange reaction with the substituent molecules.³⁸ For example, as shown in the figure 1.2 a binary mixed SAM of dodecanethiol (DDT) and mercaptoundecanoic acid (MUDA) was fabricated by the homogeneous irradiation of the primary DDT template. Since irradiation can be performed not only homogeneously but by a focused electron beam as well, IPER can be directly implemented in

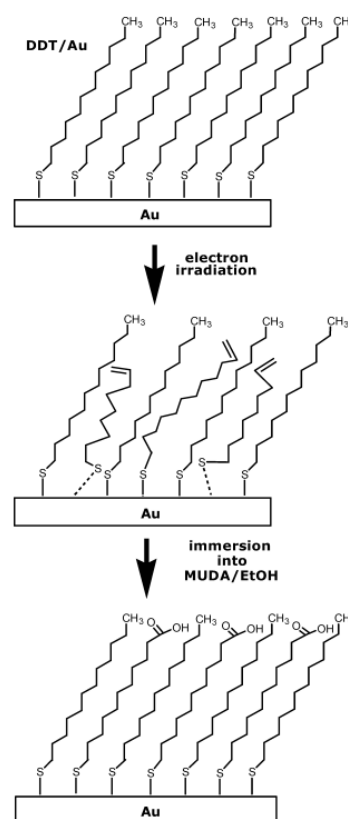


Figure 1.2 Schematic sketch of the irradiation-promoted exchange reaction[38].

the lithographic framework and used for the fabrication of different chemical patterns down to the nanometer scale.

As impressive example for the possibilities of the IPER technique, preparation of protein patterns down to micrometer scale has been demonstrated.³⁹ In these experiments, a protein repelling oligo(ethylene glycol) substituted alkanethiolate (OEG-AT) SAM on gold substrate was used as the primary template and the biotin-terminated OEG-AT molecules served as the substituents.³⁹ These components could be mixed by IPER in a broad range of compositions, resulting in precise control over the amount of the biotin terminated molecules imbedded into the protein-repelling OEG-AT matrix.⁴⁰ In combination with EBL, this allowed the preparation of specific protein affinity patterns, as mentioned above and gradient protein pattern as shown in figure 1.3. This approach could be modified further to utilize not only electrons but also UV light as the primary modification and writing tool by using a combination of UV-promoted exchange reaction (UVPER) and UV lithography with the OEG-based matrix for protein patterning⁴¹. These techniques were proven to be suitable for the fabrication of arbitrary large arrays of proteins with nanometer scale precision. In other studies, EBL was used as a writing tool for the generation of patterns over a length scale ranging from centimeters to nanometers,⁴²⁻⁴⁵ with no limitations to the pattern shape.⁴³⁻⁴⁴

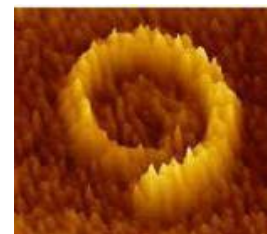


Figure 1.3 AFM images (3D) of complex, gradient-like protein patterns fabricated by EBL in EG6 matrix.[39]

Another important class of biomolecules, crucial for the fabrication of biosensors and biological assays are DNA, relying on site- sequence-specific hybridization.⁴⁶⁻⁴⁸ Accordingly, the immobilized of various single stranded DNA (ssDNA) probes on solid support can be applied to the production of multichannel biosensors due to the diversity of complementary ssDNA conjugates, thus making it suitable in a DNA chip for the detection of target genes⁴⁹ and in a protein chip for the detection of target antigens. The ssDNA chip can be converted into a protein chip via site specific hybridization of antibody-ssDNA conjugate and the protein surface can be converted back into a DNA surface by dehybridizing the complementary DNA (as shown in figure 1.4).⁵⁰⁻⁵¹ In this context, controlled immobilization of ssDNA on solid support is an important issue of practical relevance.

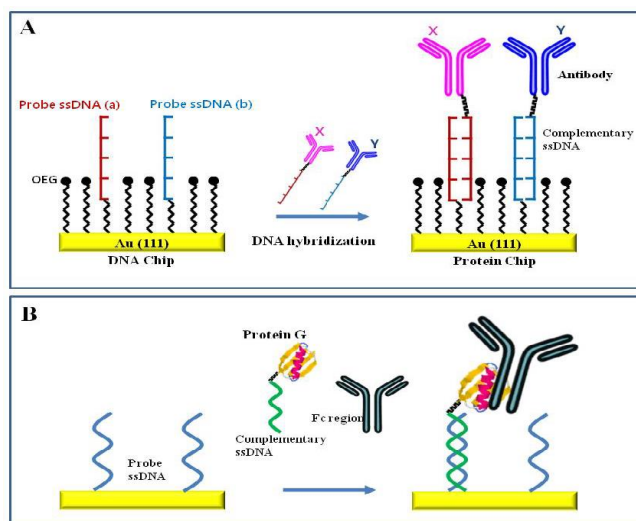


Figure 1.4 Schematic of (A) DNA-directed immobilization of DNA-protein conjugates using complementary hybridization of DNA, and (B) DNA-directed antibody immobilization by the protein G-DNA conjugate.[50,51]

Subsequently, motivated by the recent works on protein patterning by IPER-EBL (see above),^{37,39-40} a dedicated approach was developed within the given thesis work to prepare mixed ssDNA/OEG-AT films in a broad range of compositions and ssDNA/OEG-AT patterns of arbitrary shape. As a primary test system, thiolated ssDNA were used. The mixing of OEG-AT and thiolated ssDNA occurred through the exchange reaction between the primary OEG-AT molecules assembled in the SAM fashion on a gold substrate and ssDNA species in solution. The extent and rate of this reaction could be precisely tuned by preliminary electron irradiation of the primary OEG-AT monolayer with a suitable dose, resulting in a homogeneously mixed ssDNA/OEG-ATs monolayer of desired composition. Noticeably, the cross section of the ssDNA strand (120-190 Å²) is about 10 times larger than that of the OEG-AT species (~21.4 Å²),⁵² so that the exchange of the e-beam modified OEG-AT species for thiolated ssDNA is not a trivial process, involving presumably several molecules in the OEG-AT matrix in the single event.⁵³ In addition to the development of new nanolithographic method, the versatility of the approach was demonstrated by its combination with TdT catalyzed surface-initiated enzymatic polymerization (SIEP) that allowed amplification of the ssDNA/OEG-AT patterns, including gradient ones, in the z-direction. Importantly, the ability to introduce gradients in the surface concentration of the ssDNA by IPER allows the formation of nanostructures with a structural complexity that is not possible by other nanofabrication methodologies.

The above procedures rely on the specific affinity of thiolated ssDNA to gold, provided by the thiol anchor group. However, thiolated ssDNA are not the only precursors for the formation of ssDNA monolayers on coinage metal substrates. Alternatively, and even more frequently, asymmetric and symmetric disulfides, including commercial ones are used for this purpose,⁵⁴⁻⁵⁷ relying on the substrate mediated cleavage of the disulfide bond and formation of the thiolate bonds with the substrate for both chain parts. As compared to thiols, disulfides are less prone to oxidation and can therefore be better preserved or stored for a prolonged time. The resulting SAMs exhibit usually similar properties as those formed from thiols, which makes both these precursors equally good. In this context it was important to test the possibility to perform IPER with disulfide ssDNA precursors, which should broaden significantly the application range of IPER.

As a reference system and as an independent study, the possibility to perform IPER with a disulfide substituent was tested by using films of non-substituted alkanethiolates (AT) on gold as templates and symmetric dialkyldisulfides substituted with -COOH and bromoisobutyrate (BIB) groups as the substituents. The results were compared to the well-studied reference system of the same primary matrix and -COOH substituted ATs as substituent.⁴⁵ The effect of electron irradiation and exchange process were monitored in detail, which gave information about both kinetics of the substitution reaction and composition of the resulting mixed films. The usefulness of the approach was demonstrated by the fabrication of complex chemical templates for the growth of polymer micro- and nanobrushes. These templates were prepared by IPER-EBL using as substituent a disulfide molecule bearing the BIB group serving an initiator for surface initiated polymerization.

Based on the above results, ssDNA/OEG-AT monolayers from ssDNA-based disulfide precursors were prepared and tested. These precursors served as substituents for the OEG-AT matrix exposed to electrons within the framework of the IPER approach. As test ssDNA

moieties, a well defined adenine-based thiolated homo-oligonucleotide (25-mer) (reference), asymmetric disulfide, and symmetric disulfide were chosen. In all cases, the ssDNA strands were connected to the anchor group by a short alkyl chain. In the case of the asymmetric disulfide, the second chain part was comprised of mercaptohexanol; this moiety is sometimes described as a protective group.⁵⁸ Along with the application of the above precursors in the framework of the IPER approach, a detailed study was performed for the comparative characterization of the ssDNA monolayers fabricated on the basis of the same ssDNA molecules within the standard immersion procedure.²⁰

The application of the IPER approach requires high vacuum and, in the case of advanced patterning, relies on complex experimental setups such as scanning electron microscopes (SEM) with pattern generator systems.^{39,53,59-60} In contrast, the use of this approach in combination with ultraviolet (UV) lithography does not need such complex equipment and can be performed under ambient conditions.^{41,61} Similar to electrons, UV light is capable to introduce defects into the aliphatic SAMs and OEG-AT monolayers in particular.^{41,61-64} The primary processes are photooxidation of the thiolate headgroups, resulting in significant weakening of the headgroup-substrate bond,⁶⁵⁻⁶⁷ and, in the case of the OEG-AT SAMs, noticeable damage of the OEG segments.^{41,61-62} Both these processes are well suitable to promote exchange reaction between the damaged SAM constituents in the film and potential substituents in solution,^{41,61} providing a basis for UVPER and related lithography with the OEG-AT SAMs as primary templates. Significantly, nanometer scale and large area patterning are in principle possible with UV light if laser-based lithography setups, possibly in combination with diffraction equipment, are used.⁶²⁻⁶⁴ In view of the above arguments, fabrication of ssDNA/OEG-AT monolayers and patterns by UV light promoted exchange reaction (UVPER) approach was tried. The UV irradiation was performed at two different wavelengths, viz. 254 and 365 nm. UV light with a wavelength of ~254 nm is most frequently used for SAM patterning, requiring, however, quite expensive UV laser sources and UV compatible optics in the case of high resolution patterning.^{64,68-69} UV light with a wavelengths of ~365 nm or even higher (up to 390 nm) is also suitable for SAM patterning^{41,61} and can be potentially combined with well-developed standard optics as well as with commercial patterning strategies such as maskless lithography.⁷⁰⁻⁷¹

In contrast to surface-initiated polymerization (SIP) of synthetic polymers, there have been limited efforts dedicated to the *in situ* synthesis of biopolymer brushes on solid supports. Although DNA and peptides can be chemically synthesized on a solid support, these methods are limited to less than 150 nucleotides and 40 amino acids in length. Therefore, they do not allow the surface-initiated synthesis of high molecular weight polynucleotides and polypeptides. In this context, the methods to grow these types of polymers directly at an interface are of great interest. Motivated by this rationale, Chilkoti and coworkers developed recently surface-initiated enzymatic polymerization (SIEP) of deoxyribonucleic acids (DNA) polynucleotides.^{53,72-74} Whereas, the fabrication methodology and application of TdT for SIEP of ssDNA are fairly well developed, there is significantly less information about the structure of these DNA brushes. To this end a detailed spectroscopic characterization of ssDNA brushes, polymerized by SIEP was performed using a combination of synchrotron-based X-ray photoelectron spectroscopy (XPS) and angular-resolved near-edge X-ray absorption fine structure (NEXAFS) spectroscopy. Whereas XPS gives information on the chemical composition

of the samples, relying on the specific core level photoemissions and their chemical shifts, NEXAFS spectroscopy provides analogous information by sampling the unoccupied molecular orbitals, which in some cases are more specific than the core levels probed by XPS. In addition, relying on the symmetry selection rules for the transitions between the primary core level and unoccupied molecular orbitals, NEXAFS spectroscopy gives access to molecular orientation and orientational order in the system of interest. In view of this specificity, XPS and NEXAFS spectroscopy as well as their combination are frequently used for the characterization of the ssDNA systems, resulting in specific, molecular level information.^{53-55,57-58,75-79}

In summary, this thesis describes a new and potentially universal approach to prepare both mixed ssDNA/OEG-AT films in broad range of compositions and complex ssDNA/OEG-AT patterns of arbitrary shape by a combination of the promoted exchange reaction with electron beam and UV light printing tools. The contents of the thesis are presented as follows,

Chapter 2 provides basic information regarding SAMs, mixed films, and the relevant patterning techniques.

Chapter 3 is a general overview of different analytical techniques applied for the characterization of the relevant SAMs system, fabricated patterns and polymer brushes.

Chapter 4 presents a new approach based on IPER for the preparation of mixed ssDNA/OEG-AT films and ssDNA/OEG-AT patterns of arbitrary form on micrometer and nanometer length scale. Among other issues, the characterizations of the mixed ssDNA/OEG-AT films by XPS and NEXAFS spectroscopy are discussed.

In chapter 5 the results of IPER with disulfide precursors are presented. Here the preparation of mixed SAMs of non-substituted AT and symmetric dialkyldisulfides substituted with –COOH and BIB groups is reported and the results are compared to the well-studied reference system of the same primary matrix and –COOH substituted AT as substituent. The effects of electron irradiation and exchange process are discussed in detail.

Chapter 6 describes IPER with disulfide ssDNA precursors and the characterization of prepared mixed OEG-AT and disulfide-stemming ssDNA films by XPS and NEXAFS spectroscopy.

In chapter 7 the preparation of mixed ssDNA/OEG-AT films and ssDNA/OEG-AT patterns by UVPER is reported. The UV irradiation was performed at two different wavelengths, viz. 254 and 365 nm.

In chapter 8 a detailed spectroscopic characterization of ssDNA brushes, prepared by SIEP on ssDNA templates is described.

Major results and achievements of the given thesis work are summarized in chapter 9. It also includes certain considerations and suggestions for the future work.

Finally, in chapter 10, the experimental part of this thesis is presented.

2 Theoretical background

In the following section, the existing knowledge in literatures related to this work will be reviewed. First, the concept of surface modification with organic layer will be discussed. In the following sections, different patterning techniques and an overview of surface initiated polymerization process will be given.

2.1 Surfaces in nanoscience

Nanometerscale structures have a very distinguishing characteristic, that is, a high percentage of their constituent atoms are at the surface, unlike macroscopic materials. Molecules and atoms at the surface of a material experience diverse environment from those in the bulk and thus have different free energies, electronic states, reactivities, mobilities, and structures.⁸⁰ Many physical properties, viz, thermal and electrical conductivity, hardness, and plasticity are determined by the structure and chemical composition within macroscopic objects. In contrast, the physical properties of nanostructures depend to a much greater extent on their surface and interfacial environment than do bulk materials.²⁰ Bare surfaces of metals and metal oxides tend to lower the free energy of the interface between the metal or metal oxide and the ambient environment by adsorbing adventitious organic materials. These materials also alter interfacial properties and can have a significant influence on the stability of nanostructures of metals and metal oxides; the organic material can act as a physical or electrostatic barrier against aggregation, decrease the reactivity of the surface atoms.

In this context, a reproducible and defined modification of surfaces can be achieved, e.g. by applying an organic monolayer. A well-known and extensively studied example for organic layer is the self assembled monolayer (SAM).

2.2 SAMs as component of nanoscience and nanotechnology

Molecular self assembly is the spontaneous arrangement of molecules under defined conditions. In nature the self assembly mechanism is widely spread. Protein folding to tertiary structures, the DNA double strand formation or the formation of a virus are just a few examples.⁸¹ Nuzzo and Allara (in 1983) were among the first who reported the spontaneous self assembly of alkanethiols on surfaces.⁸² Many self assembled systems have been investigated over the years, but monolayers of alkanethiols on gold are probably the most studied.⁸³ Most of these studies deal with the formation of the alkanethiol monolayer on ultrasmooth thin gold surfaces (Figure 2.1).⁸⁴⁻⁸⁶ The most commonly used organo-thiol contains three different parts, a terminal functional group or tail group, a spacer and a ligand or head group. For SAM preparation the substrate is simply immersed into a dilute (approx. 1mM) solution of the adsorbate at room

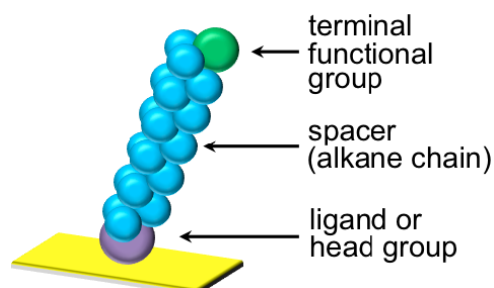


Figure 2.1 Alkanethiol (AT) supported on a gold surface

temperature.⁸⁷ The formation of SAMs relies on a strong specific interaction between the head group and the substrate. The main driving force of this accumulation is the formation of the gold-sulfur bond with a binding energy of about 44 kcal/ mol.⁸⁸ Within a few seconds to minutes after the immersion in the solution an undefined monolayer is formed. If this process proceeds, a van der Waals forces between spacers of the molecules in our case single alkane thiols cause the aggregation of the molecules and a crystalline monolayer is formed (Figure 2.2).⁸⁸

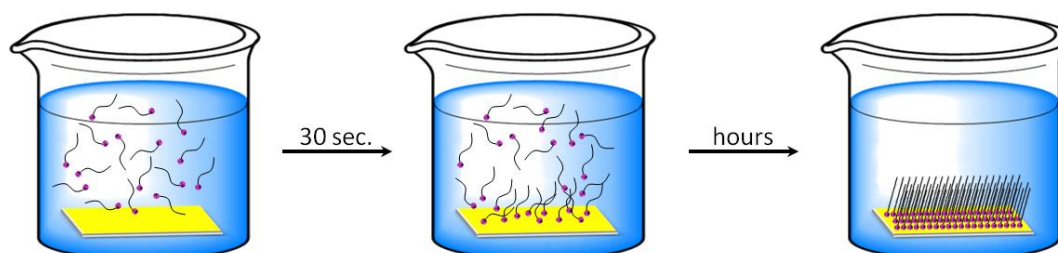


Figure 2.2 self assembled monolayer (SAM) formation process in the lab.

The spacing between the alkanethiol chains is reported to be 4.97\AA for Au(111) substrates, what is nearly three times the van der Waals diameter of a sulfur atom (1.85\AA).^{83,89} During the process of ordering dust molecules are displaced and defects in the packing density are reduced.⁹⁰ The terminal functional group determines the resulting surface properties of the organic monolayers. Fourier transform infrared spectroscopy (FTIR) studies revealed that the alkyl chains are tilted about 30° to 35° from the surface normal to maximize their van der Waals interactions.⁹¹ Electron diffraction, low energy and scanning tunneling microscopy studies showed that the thiol bonding on Au(111) is generally based on a $(\sqrt{3} \times \sqrt{3}) R30^\circ$ over layer structure where the sulfur atoms are positioned in the 3-fold hollow of the gold lattice (Figure 2.3).^{20,88} It has to be noted that the thiol molecules are bound equally to the Au lattice sites but with some variation in the molecular orientation.⁹²⁻⁹³

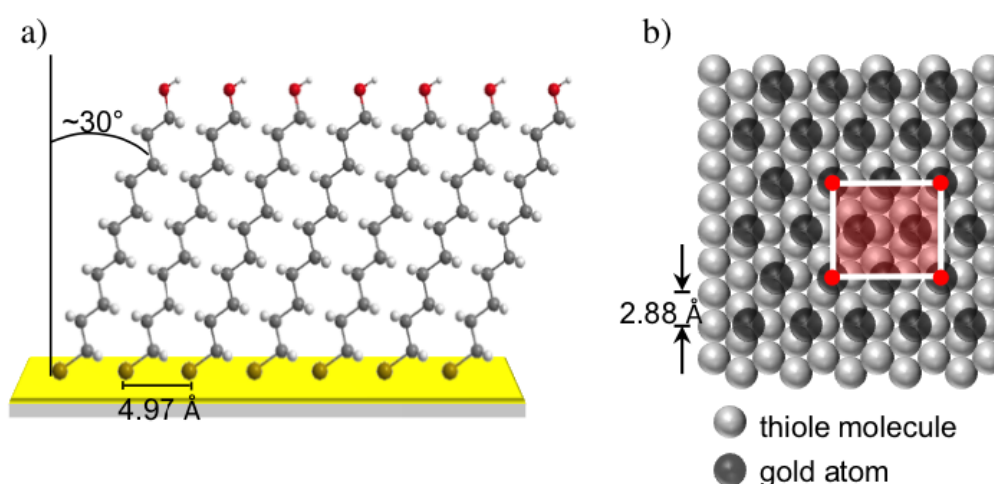


Figure 2.3 a) SAM monolayer anchored to the Au(111) substrate via a sulfur-gold bond, b) Surface structure of undecanethiol SAM on Au(111). (after ref 88)

Camillone *et al.* Observed a $c(4 \times 2)$ super lattice structure and proposed a model to explain this observation.⁹⁴ In the model, alkanethiol molecules are arranged in a $(\sqrt{3} \times \sqrt{3}) R30^\circ$ structure where all sulfur head groups are bound to identical hollow sites of the Au substrate but with alternating twist angles. Not only gold can serve as a substrate for the formation of SAMs, but also Ag can be utilized.⁹⁵ Unfortunately, compared to Au(111) less is known about the self assembly of thiols on Ag(111). Although the substrates show similarities in the symmetry or lattice spacing, alkane thiol films formed on Ag(111) display differences such as a different packing density of the sulfur atoms. In this case the over layer structure was found to be $(\sqrt{7} \times \sqrt{7}) R10.9^\circ$.^{89,96} Although the range of the reported tilt angle ranges from 0° to 14° ,⁹⁵ it may be concluded that on a Ag(111) substrate the thiols are practically standing upright on the surface.⁹⁷ Since surface properties are generally considered to be controlled by the outmost 5Å to 10Å of a film,⁹⁸ SAMs are used as well suited model surfaces to study interfacial phenomena due to the ability of fine controlling the surface properties.⁸³ In the following section one of the most popular protein-resistant SAM will be discussed in particular.

2.2.1 Protein-resistant SAMs

In diagnostic tests and biosensors based on specific recognition of antigen/antibody pairs, suppression of nonspecific protein adsorption is crucial for achieving sufficient bioassay selectivity and sensitivity. Elimination of protein adsorption requires a system where repulsive interactions between proteins and the surface overcome the attractive ones. Due to the diversity of the interactions between proteins and surfaces, a preferred strategy for blocking the adsorption of proteins is to self-assembly of oligo(ethylene glycol) -terminated alkanethiols (OEG-AT) on the gold surface. The monolayer shields the surface, introducing a high activation barrier for the proteins to adsorb. A dense film of OEG-AT on a gold surface can be formed by immersing a gold-coated wafer for 24h in ethanolic solution of the OEG in a concentration regime of several millimole per liter (Figure 2.4).

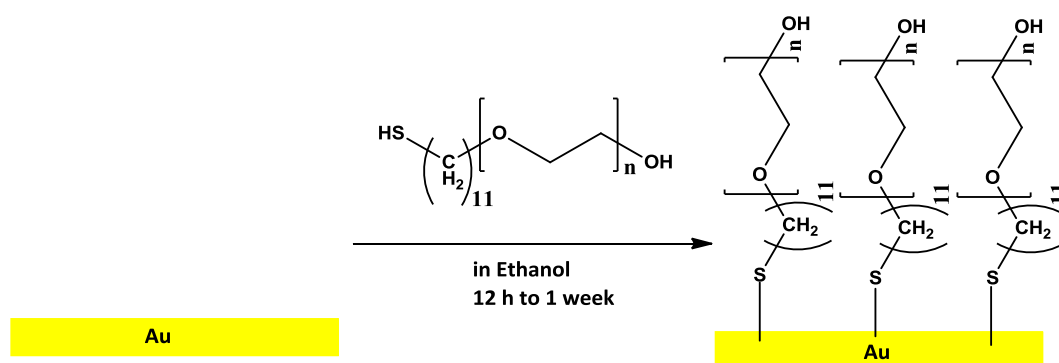


Figure 2.4 Self-assembly process of OEG-AT molecules on gold.

These OEG-AT monolayers form a dense “non-fouling” brush that confers protein resistance to the gold surface, and are arguably the best non-fouling systems that are currently available.⁹⁹⁻¹⁰⁰ Furthermore, the protein resistance ability of OEG-AT monolayers on gold significantly increase with higher length of OEG chain (3 or 7 EG units).⁴¹ In the next section, a closer look will be given on the tailoring the surface properties by one of the popular means i.e. mixing different molecules containing different tail groups in a SAM.

2.2.2 Mixed SAMs

As discussed in the previous section, Self-assembled monolayers (SAMs) provide a convenient, flexible, and simple system to tailor the interfacial properties of metals, metal oxides, and semiconductors. An additional flexibility appears if molecules containing different tail groups are mixed together in a SAM. Mixed SAMs are monolayers containing at least two different molecules. There are several different popular approaches to prepare mixed SAMs, such as coadsorption from a solution containing different thiols or the use of asymmetric sulfides or disulfides. When using coadsorption for preparation of mixed SAMs the ratio of molecules in the monolayer can be influenced by the mole fraction of the respective molecules in solution.¹⁰¹ However, this method is not very reliable since certain molecules adsorb more readily than others, as they form more stable structures. Also, it is reported that sometimes phase segregation is occurring with this method, i.e. molecules of one sort aggregate in one area instead of forming a homogeneous mixture with the other molecules.¹⁰² This last problem can be avoided by using asymmetric disulfides for the assembly of mixed SAMs. These molecules presumably split in two parts and form thiolate-gold-bonds when adsorbed, just like thiols. Using this method also generates a higher probability of getting mixed SAMs with a 1:1 ratio, although this is not guaranteed, since adsorption is reversible and consequently, the thermodynamically more stable SAMs form.³³ Another disadvantage of disulfides is their low solubility. Preparing mixed SAMs with sulfides as another approach is very limited due to the weak bonding interactions with the gold surface (sulfides remain intact and no thiolate is formed). However, monolayers with 1:1 ratios are easily obtained.¹⁰³

Judging from the available ways to prepare mixed SAMs, it is obvious that other methods are required to produce mixed SAMs with custom-made compositions and certain structures, e.g. gradient-like structures or even patterns. Such surface modifications are achieved by the use of lithography or printing tools. Mixed SAMs with custom-made composition can then be fabricated by dipping pre-patterned (using printing tools, lithography or other techniques) pure monolayer surfaces into a solution of a different molecule. An alternative approach to prepare mixed SAMs is irradiation promoted exchange reaction (IPER).³⁷ The key idea of the approach is tuning the extent of the exchange reaction between the primary SAM covering the substrate and a potential molecular substituent by electron irradiation, which allows fabrication of binary mixed SAMs of variable composition depending on the selection of doses. The physics behind this method is the creation of irradiation-induced chemical and structural defects in the primary SAM, which promote the exchange reaction.³⁸ In this current work, IPER approach was employed for the fabrication of mixed SAMs. In the following section a general discussion about modification of surface structure by employing lithographic methods will be given.

2.3 Patterning strategies

In last few decades, one important challenge in modern science and technology is to generate small structures. There are many methods that might be employed to make new types of small structures or by downsizing existing structures. Therefore modern lithography techniques are a vital candidate to modify structures of surfaces. The structuring of surfaces can be

accomplished by diverse methods. Table 2.1 gives an overview over most important ways of structuring surfaces. Most of these techniques listed are applicable for patterning self-assembled monolayers.

Table 2.1: Overview of different lithography methods

Method	Resolution	Area
Microcontact printing (μ CP) ¹⁰⁴⁻¹⁰⁵	100nm	>1 cm ²
Nanoimprint lithography (NIL) ¹⁰⁶⁻¹⁰⁷	10nm	> 1 cm ²
Inkjet printing (IP) ¹⁰⁸	30 μ m	> 1 cm ²
Magnetolithography (ML) ¹⁰⁹⁻¹¹⁰	10nm	> 1 cm ²
UV lithography ¹¹¹	50 nm	> 1 cm ²
Lithography with electrons, ions	1 -10 nm	> 1 cm ²
Electron beam lithography (EBL) ¹¹²⁻¹¹³		
Focused ion beam lithography (FIB) ¹¹⁴		
AFM/STM-based lithography ¹¹⁵	1nm	nm ² – cm ²
Dip-pen lithography ¹¹⁶		
Nanographing ¹¹⁷		
STM lithography ¹¹⁸		

SAMs are used as irradiation sensitive films (so-called resists), since they change their chemistry upon irradiation. If the irradiated area of the resist is easily removable from the substrate through etching or the use of solvents, then, it is a positive resist. Vice versa, if the irradiated area is not removable or less removable, then, it is a negative resist. Different types of optical lithography with UV light¹¹¹ and X-ray lithography exist¹¹⁹ but these methods usually require a huge technical effort. The advantage is that these are fast methods by which high resolutions and good aspect ratios can be achieved.

A higher resolution can only be achieved by using dip-pen lithography,¹²⁰ nanographing¹¹⁶ or scanning tunneling microscopy (STM) lithography.¹¹⁸ However, these methods are much slower and not applicable to structure large areas. Other printing or stamping techniques which utilize self-assembly processes are inkjet printing,¹⁰⁸ nanoimprint lithography¹⁰⁶ and microcontact printing.¹⁰⁴ For the latter, a conformal contact between the stamp and the surface of the substrate is essential to transfer the 'ink' to the surface. By backfilling the non-patterned areas with a different alkanethiol, binary-component SAMs are formed. This printing has the advantage of simplicity and convenience. Once a stamp is available, multiple copies of the pattern can be produced and it is, with this method, possible to structure larger areas.¹²¹ However, the roughness and the dimensions of the elastomeric stamps limit the resolution of the resulting patterns.¹²² Also, the mechanism of the patterning has an influence since after the transfer the alkanethiols can spread from the contact region of

the stamp into noncontact areas, like ink spreads on a piece of paper.¹²³ Higher efficiency can be achieved by linking so-called bottom up techniques like self-assembly with top down techniques like e-beam lithography.

2.3.1 E-Beam chemical lithography

E-beam lithography is one of the most powerful techniques for patterning down to nanometer scale. There are two different methods available to structure surfaces via e-beam, viz, proximity printing and direct writing with a focused e-beam. Proximity printing is a parallel technique; the large surface areas are accessible by a broad e-beam which irradiates the substrate covered by a mask with a constant irradiation dose. Here the resolution is limited to $\sim 100\text{nm}$ due to the accuracy of the used masks. The later method, that is, direct writing is a serial mode technique, where, a better resolution down to a few nm is possible. The drawback is that this serial mode is limited in speed.¹²⁴ The important parameter for both methods is the choice of the right electron energy. Figure 2.5 shows the 'universal' curve for the penetration depth of electrons in some metals which depends on the electron energy.¹²⁵

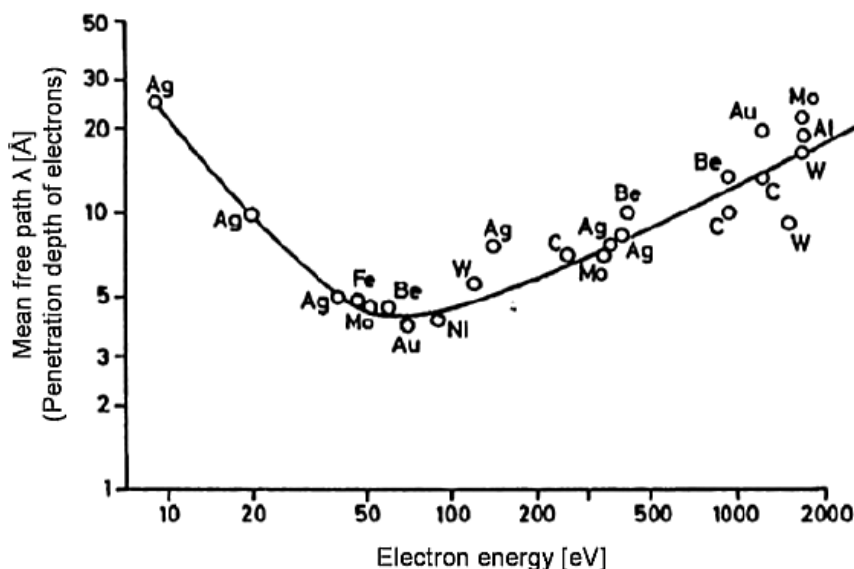


Figure 2.5 Penetration depth of electrons in dependence of primary electron energy and the irradiated material. (after ref 125)

The lowest penetration depth of $\sim 50\text{nm}$ could be observed in the range of 50 eV to 100 eV independent of the material of the substrate. Elastic and inelastic scattering processes lead to a generation of secondary electrons which are scattered in all directions (proximity effect). This leads to a broadening of the primarily irradiated area. Hence the higher the energy of the electrons is, the higher the penetration depth is and thereby the lateral scattering. On the other hand beams of higher electron energies are better focusable since the electrons interact less with each other leading to a smaller spot size.

In this thesis, chemical lithographic with E-beam was used to prepare patterns on chemical template. This process was first described by Eck *et al.* for the generation of amino groups on aromatic self-assembled monolayers by low energy electron beams.¹²⁶ They

described that terminal nitro functional groups in 4'-nitro-1,1'-biphenyl-4-thiol SAMs can be converted into amino groups by a proper electron dose. Basically, the interaction of low energy electrons (50eV-3KeV) with SAMs leads to various effects. Aliphatic and aromatic SAMs can be used for this procedure and both can either act as a positive or negative resist. (Secondary) electrons with energies between 10 eV and several keV cleave C-H and C-C bonds in the organic monolayer. This predominantly causes cross-linking reactions between the aromatic moieties in aromatic SAMs, resulting in selective deposition or etching in the regions that were not irradiated, analogous to using a negative resist in conventional lithography.¹²⁷ In contrary, in aliphatic SAMs dose-dependent fragmentation and desorption are the predominant phenomenon, which make them useful as positive resist material for EBL¹²⁸. Irradiation of thiolated SAMs results in degradation of the monolayer, forming various fragments, unsaturated bonds, and sulfides.¹²⁹ Aromatic and aliphatic SAMs show different behaviour to electron beam exposer. Aromatic SAMs remain mostly intact under electron irradiation only chemical modification of tail groups occur,¹²⁶ whereas for aliphatic SAMs, irradiation results mostly in fragmentation and disordering of the surface molecules.⁴³

2.4 Surface initiated polymerization

The surface functionalization with polymer brushes can be performed according to two strategies, the *grafting to* and *grafting from* techniques. In the *grafting to* approach, end-functionalised polymer chains are chemically or physically attached to the surface. In *grafted from* coatings, polymer brushes are grown from surface-bound polymerization initiators. This method, also called surface-initiated polymerization (SIP), has the advantage of a better control over the type of grafted polymers, the surface-grafting density and the chain-length. The resulting materials display a large array of characteristic features. Being very robust and solvent-stable, polymer brushes have various potential applications. Grafted from nanoparticles, they have been used for controlling colloidal stability and particle self-assembly, while polymer brushes on planar surfaces have the ability to produce stimulus-responsive films with application in sensing¹³⁰ and nanoactuation¹³¹. Furthermore, they can also be used for lubrication and antibacterial and protein-resistant¹³² coatings.

In the vast majority of SIP¹³³ studies, controlled or living radical polymerization¹³⁴ (CLRP) has been used to grow well-defined polymer brushes. As mentioned above, this technique requires surface bromide/chloride groups as initiators.

2.4.1 Controlled / living radical polymerization

A living polymerization is defined by two requirements. Firstly, it can proceed if a second charge of monomer is added after the first charge has been consumed, with no new chains being formed. Second, propagation proceeds in the absence (or suppression) of irreversible chain transfer or chain termination, i.e. the growing chain end will only undergo reaction with monomer. As a result living polymerization allows excellent control over polymer chain length, architecture and composition. It allows the synthesis of well-defined block copolymers and to deliberately choose the end group of the chain, so that various types of polymer architectures can be obtained by living polymerization.¹³⁵ In the last two decades several CLRP processes have been published, with the most famous being nitroxide-mediated polymerisation,¹³⁶

reversible addition-fragmentation chain transfer polymerization (RAFT)¹³⁴ and atom transfer radical polymerization¹³⁷⁻¹³⁸ (ATRP). In this thesis, the prepared various patterns on the DDT/Au template were extended to the Z-direction by SI-ATRP method.

2.4.2 Atom transfer radical polymerization

Atom Transfer Radical Polymerization (ATRP) is the most widely employed technique for the formation of polymer brushes via SIP. ATRP is compatible with a variety of functionalised monomers, and the living/ controlled character of the ATRP process yields polymers with a low polydispersity (M_w/M_n), that are end functionalised and so can be used as macroinitiators for the formation of di- and triblock copolymers. Equally important, surface-initiated ATRP is experimentally more accessible than for example, the living anionic and cationic polymerizations, which require rigorously, dry conditions. The controlled nature of ATRP is due to the reversible activation–deactivation reaction between the growing polymer chain and a copper–ligand species. The polymer brush formed by using SI-ATRP combines the advantages of SAMs, namely their high surface density and ease of formation, with those of polymers — thicker and more robust films with versatile architecture and chemistry. SI-ATRP is one example of the grafting from strategy in preparing polymer brushes on surfaces. ATRP belongs to the class of living polymerization and has proved to be one of the methods for precision polymer synthesis. Since the initiation is faster than or at least comparable to the propagation rate, the obtained polymers have a narrow molecular weight distribution (MWD). Hence, a polymer film generated on a surface by ATRP will have an almost equal overall thickness. ATRP can be carried out under mild reaction conditions and allows a wide range of functional groups to be present in the monomer, solvent, or initiator, and thus can be applied to a broad spectrum of polymeric systems.

In general, a wide range of monomers can be polymerised by ATRP including (substituted) styrenes, (meth)acrylates, (meth)acrylamides, vinylpyridines and acrylonitrile. It can be carried out in various solvents, such as benzene, toluene, anisole, ethyl acetate, ethylene carbonate, acetone, dimethyl formamide (DMF), alcohol, water and supercritical carbon dioxide. The initiators are typically chlorides or bromides. They can be either small molecules or functionalised polymers. In the latter case they are called *macroinitiators*.

The reaction is initiated by the homolytic cleavage of the carbon-halogen bond in the organic halide via one electron oxidation of the metal center ($M^nX_nL_m$) to form an initiating radical species ($R\bullet$). The $R\bullet$ reacts with the unsaturated species (monomer) to generate a radical species $[R-CH_2-C(R_1)(R_2)\bullet]$. This radical intermediate attacks the next monomer successively and generates a polymer chain (Fig. 2.6).¹³⁹ The key factors in preventing a high polydispersity index are the low concentration of the radical intermediates and their fast but reversible transformation into a dormant species before undergoing successive addition to monomers.

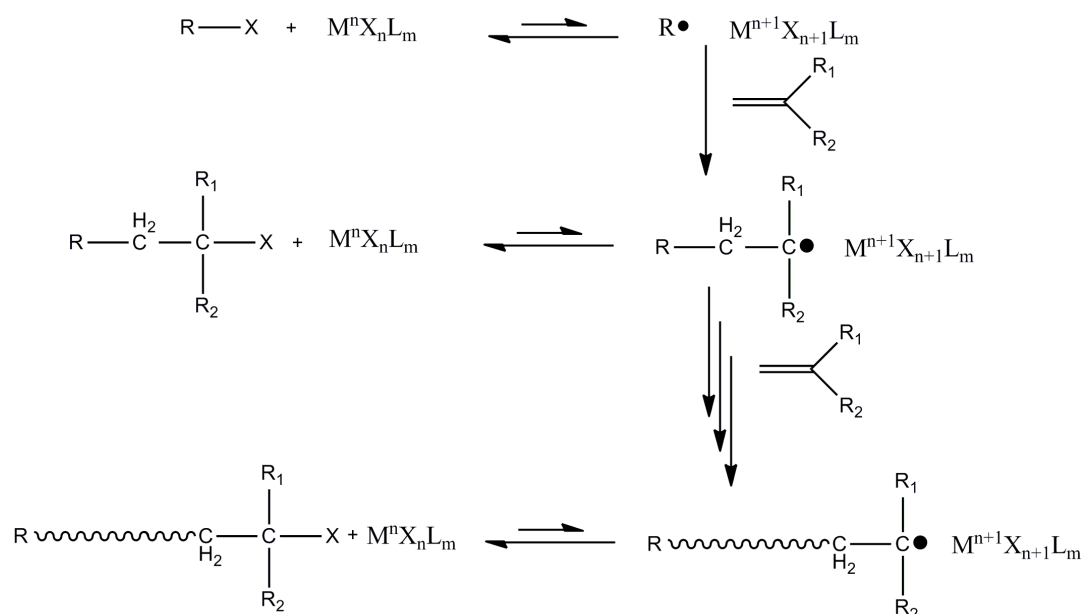


Figure 2.6 Mechanism of ATRP by Kamigaito *et al.* (after ref 139)

ATRP-polymerization on a surface is realized by the immobilization of the initiator molecules onto a surface, followed by polymerization of the desired monomer solely from the surface with help of a transition-metal catalyst (Fig. 2.7).

Matyjaszewski and co-workers described controlled polymerizations without added free initiator;¹⁴⁰ instead a Cu^{II} ligand complex was added to act as a deactivator. The addition of these complexes to the polymerization solution increased the initial Cu^{II} concentration to the same end as the addition of free initiator. Evidence of a controlled reaction was gained from a linear increase in ellipsometric thickness with time; identical yet separate experiments to form polymer in solution gave a graph showing a linear relationship between M_n and brush thickness.

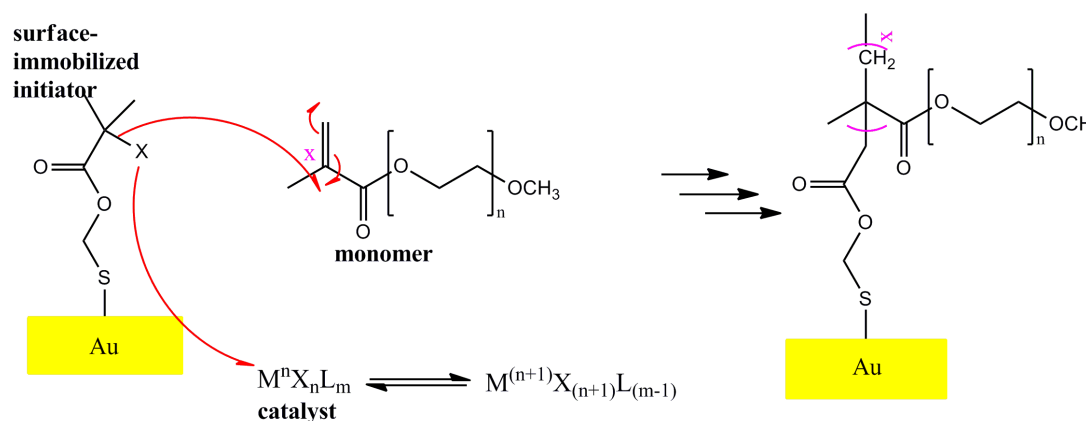


Figure 2.7 Scheme of surface initiated atom transfer radical polymerization (SI-ATRIP) on gold.

However, calculations of anticipated brush height for extended chains from polymer in solution showed that tethered polymer has a height of approximately one sixth of that calculated. Slower growth of the surface bound polymer due to geometric constraints resulting from high surface density of the chains could account for this observation. Alternatively, termination reactions from the dense initiator monolayer could play a role. Termination reactions throughout the polymerization would result in the loss of the terminal bromine atom from the chain thus preventing the re-initiation of the polymer brush to form block copolymer brushes. The introduction of surface-initiated polymerizations in aqueous media resulting in controlled polymer brush growth at room temperature, even for water insoluble polymers such as PMMA and PGMA. Surface polymerization at lower temperatures has several advantages; firstly these polymerizations are compatible with substrates that are sensitive to elevated temperatures, for example, thiol SAMs on gold. Water accelerated ATRP was shown to be able to grow very thick polymer films in short reaction times. Huang *et al.* used surface initiated ATRP from SAMs on Au to grow 700 nm thick PHEMA films in just 12 hours.¹⁴¹ Room temperature ATRP was utilised by Bruening and coworkers to grow cross-linked films of ethylene glycol dimethacrylate (EGDMA).¹⁴² These brushes have pendant methacrylate groups which lead to cross-linked polymer films that have better mechanical and chemical stability than linear polymer brush analogues.

2.4.3 Surface initiated enzymatic polymerization

Surface-initiated enzymatic polymerization (SIEP) of deoxyribonucleic acids (DNA) exploits the ability of a template independent polymerase.⁷²⁻⁷³ The key component of this strategy is the enzyme i.e. terminal deoxynucleotidyl transferase (TdT), which catalyzes the stepwise addition of deoxynucleotide (dNTP) to the 3'-OH termini of single-stranded DNA (ssDNA) chains, following the reaction stoichiometry shown in Figure 2.8. TdT requires an exposed 3'-OH presented by single stranded (ss) oligonucleotide that can be as short as 3 nucleotides, and TdT can extend this primer to create long (up to kilobases) polynucleotides with high monodispersity but with a strong preference for dATP and dTTP. TdT was discovered in 1960 when it was isolated from the calf thymus gland as a unique deoxynucleotide-polymerizing enzyme.¹⁴³

Bollum *et al.* have investigated the nature of the TdT reaction and kinetics by looking at initiators and substrate properties, buffer conditions, the effect of divalent metal ions, pH, and inhibitors on DNA polymerization by TdT.¹⁴⁴ The unique characteristic of TdT is that, it is a template independent DNA polymerase that catalyzes an irreversible reaction with pyrophosphate as the side product. Based on the study by Bollum *et al.*, the TdT reaction requires a primer initiator with a minimum of three phosphate groups and three deoxy residues, it incorporates a wide range of dNTPs and it requires metal cofactors. The characterization of TdT using homopolymer tailing (<50 bases) revealed that TdT acts more efficiently on protruding ends compared to recessive or blunt ends.¹⁴⁵

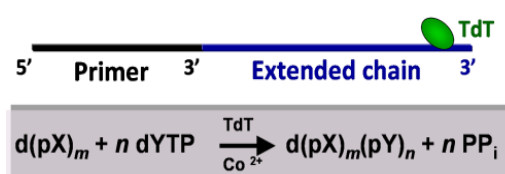


Figure 2.8 TdT reaction stoichiometry, where the length of the extended chain is determined by the ratio of monomer to initiator concentration. The TdT reaction is a linear condensation polymerization reaction.

3. Characterization methods

In this chapter the analytical techniques are described, which were used in the framework of this research project to characterize various surface properties of the prepared homogeneous monolayers, mixed films and polymer brush patterns on the Au surfaces.

3.1 X-ray photoelectron spectroscopy

X-ray photoelectron spectroscopy (XPS), also called electron spectroscopy for chemical analysis (ESCA) is the most widely used surface characterization method. It exploits the photoelectric effect to analyze the chemical composition of surfaces. Einstein's explanation of this effect was honored in 1921 with the Nobel Prize in Physics. In XPS, the sample is irradiated with low-energy (~ 1.5 keV) X-rays, in order to provoke the photoelectric effect. Irradiated atoms emit photoelectrons after direct transfer of energy from the photon to the core-level electrons. The energy spectrum of the emitted photoelectrons is determined by means of a high-resolution electron spectrometer. The amount of photoelectrons emitted depends on the concentration of the emitting atom in the sample. The analysis is conducted in an ultrahigh vacuum (UHV) chamber typically at $p < 10^{-8}$ bar. XPS is very surface-sensitive and only the topmost layer of only a few nanometers is measured. What makes the XPS particular interest is the fact that the energy of the photoelectrons additionally depends on the chemical environment. This leads to a chemical shift depending on the oxidation state, hybridization or inductively acting substituents on the atom.

3.1.1 Basics

When a photon imposes on an atom, one out of three events can take place (Figure 3.1).¹⁴⁶ The photon can pass through without interaction, it can be scattered by an atomic

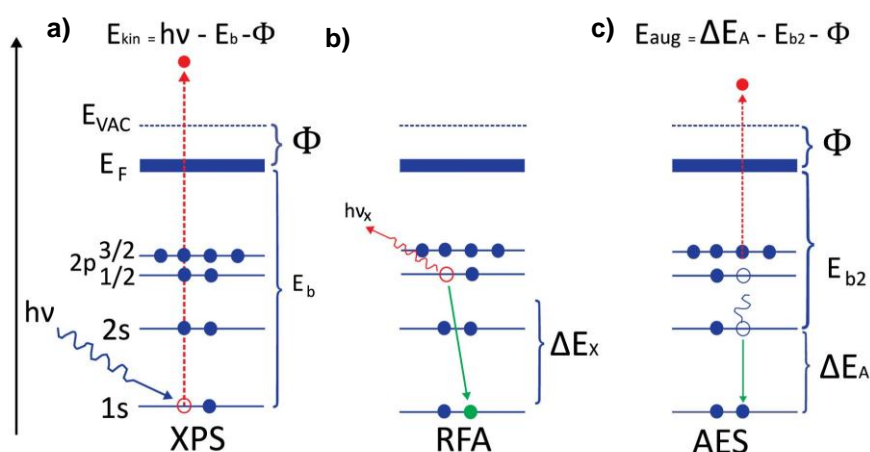


Figure 3.1 Energy level diagram of the photoelectron spectroscopy (XPS), a) excitation of a photoelectron by an X-ray photon; b) relaxation by fluorescence; c) relaxation by emission of an Auger electron; E_F Fermi energy; E_{VAC} vacuum energy; $h\nu_x$, ΔE_x energy of the photoelectron or of the fluorescence photon. (After ref 146)

orbital electron leading to partial energy loss or it can interact with an atomic orbital electron with total transfer of the photon energy to the electron, leading to electron emission from the atom. The second possibility is referred to as Compton scattering and can be important in high-energy processes. The third process describes the photoemission process, which is the basis of XPS.

Each element has a characteristic threshold level at which electrons can be ejected from an atom. The frequency of excitation, thus, has to be equal or greater than this value. If the energy of the excitation photon is too low, no photoemission will be observed. However, if the threshold frequency is exceeded, the number of electrons emitted will be proportional to the intensity of the incoming photo flux and to the density and cross section of the respective element. The kinetic energy of the emitted electrons is linearly proportional to the frequency of the exciting photons. This photoemission process from excitation to emission is extremely rapid (10^{-16} s).

When a surface is irradiated by X- rays, the core level electrons of surface atoms absorb the X-ray photon energy, $h\nu$. If the binding energy overcome ($h\nu > E_B$), electrons are emitted from the surface with a defined kinetic energy E_{kin} .

Einstein's described the process by the following equation,¹⁴⁷

$$E_B = h\nu - E_{kin} - \Phi \quad (3.1)$$

Where E_B is the binding energy of the electron in the atom, $h\nu$ is the energy of the X-ray source (known value) and E_{kin} is the kinetic energy of the emitted electron (measured in the XPS). Φ is the work function of the instrument. Their kinetic energy is characteristic of the chemical element from which it was emitted. Therefore both E_{kin} and Φ are measured to determine the E_B . Consequently, the binding energy which is usually expressed in electron volts ($1 \text{ eV} = 1.6 \times 10^{-19}$ joules) is easily determined and Φ is the minimum energy required to eject an electron from the highest occupied level in vacuum.

3.1.2 Construction of apparatus

A schematic diagram of an X-ray photoelectron spectrometer is shown in figure 3.2. XPS measurements must be performed under vacuum because photoelectrons must be able to transfer from the sample to the detector without colliding with any gas phase molecules. To avoid contamination of the sample vacuums of 10^{-9} - 10^{-10} bar, depending on the reactivity of the surface, is necessary. Basically, an XPS spectrometer consists of three elements: the X-ray source, the energy analyzer and the detector. As discussed in the last section, that the kinetic energy of the photoelectron depends on the wavelength of X-rays, so it is important to use x-ray radiation at low energy defined as the line width. Most commonly Mg and Al are used as anode material, which have emission K alpha line at 1253.6 eV with a FWHM of 0.7 eV and at 1486.6 eV with a FWHM of 0.85 eV respectively (table 3.1). Using a monochromator allows the half-width of < 0.3 eV lower, but it will narrow the energy spread of X-rays striking the sample and reduce intensity of the X-rays. Therefore, it is usually omitted in standard spectrometers

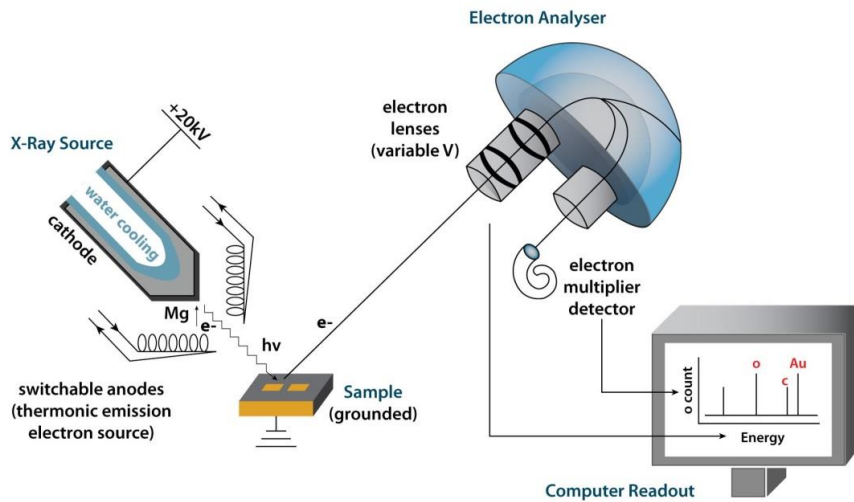


Figure 3.2 Schematic of an XPS instrument

on the monochromator equipped with efficient collection lens, energy analyzer and multi-channel detector system.

Table 3.1 General properties of Mg K α and Al K α X-ray radiation source¹⁴⁶

X-ray source	Energy (eV)	Width (eV)
Mg K α	1253.6	0.70
Al K α	1486.6	0.85

The most important component in XPS is the energy analyzer, the kinetic energy of photoelectrons emitted from the sample is determined. Electrostatic hemisphere analyzer is most commonly used consisting of two concentric metal hemispheres with the inner and outer radius r_1 and r_2 . A potential of ΔV is placed across the hemispheres such that the outer hemisphere is negative and inner hemisphere is positive with respect to the potential applied at the center line,

$$R_o = \frac{r_1 + r_2}{2} \quad (3.2)$$

The center line potential is known as pass energy. Most measurements are done with constant pass energy. This will maintain a constant absolute resolution, ΔE , for all photoelectron peaks. Typically 5-25eV pass energies are used for high resolution spectra, while 100-200 eV pass energies are used to acquire survey scans.

The detector counts the number of electrons reaching it per unit of time through the energy analyzer. The XPS spectrum is produced by varying the voltages on the lenses and the analyzer so that the trajectories of electrons ejected from the sample at different energies are brought to a focus at the analyzer exit slit. A channeltron type electron multiplier behind the exit slit of the analyzer amplifies individual electrons by 10^5 - 10^6 , and each such pulse is transferred to an external conventional pulse counting electronics and into a computer. The

computer also controls the lens and analyzer voltages. A plot of electron pulses counted against analyzer voltage yields the photoelectron spectrum.

3.1.3 Surface sensitivity analysis

Excited electrons in X-ray PE can travel only short distances through solids before losing energy due to collisions with atoms. Only photoelectrons ejected from atoms close-by the surface escape unscattered and appear in the XPS peaks. Electrons originating from deeper regimes have correspondingly reduced chances of escaping unscattered and mostly end up in the background at lower KE after the XPS peak, as shown in figure 3.3a.

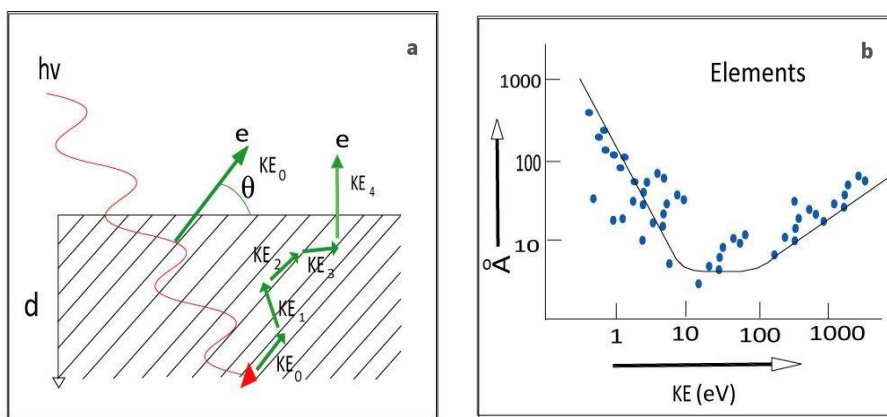


Figure 3.3 a) Schematic of inelastic electron scattering occurred as a photoelectron tries to escape from the solid, starting at different depths. b) Mean free path lengths λ_e as a function of the kinetic energy of the emitted electrons. (After ref 147)

Thus, the peaks originate mostly from atoms near the surface, the background mostly from the deeper regime of the sample. This is the reason for the surface sensitivity of XPS.

The inelastic mean free path length (λ_e), which determines quantitatively exactly how surface sensitive the measurement is, depends on the kinetic energy (KE) of the emitted electron and the material through which it travels. Empirical relationships between KE and λ_e are plotted in Figure 3.3b for a variety of elements.

3.1.4 Determination of the stoichiometric composition

There are two available models system for the evaluation of stoichiometric composition of SAMs. The stoichiometric ratio of a layer A and an underlying layer B is then calculated from the measured intensities according to equation.

$$\frac{N_A}{N_B} = \frac{I_A}{I_B} \cdot \frac{\sigma_B}{\sigma_A} \cdot \frac{d_A}{\lambda_A} \cdot \frac{\exp\left(-\frac{d_A}{\lambda_B}\right)}{1 - \exp\left(-\frac{d_A}{\lambda_A}\right)} \quad (3.3)$$

$N_{A,B}$	Stoichiometric factors
$I_{A,B}$	Signal intensity
$\sigma_{A,B}$	Element specific cross section for the emission of a photoelectron
$\lambda_{A,B}$	Attenuation length [\AA] of a photoelectron at a given energy E_A, E_B
d_A	Film thickness of a component A [\AA]

For analysis of disordered, undefined or unknown systems the statistical model is used, which assume a homogeneous distribution of two elements A and B in the substrate.

$$\frac{N_A}{N_B} = \frac{I_A}{I_B} \cdot \frac{\sigma_B}{\sigma_A} \cdot \frac{\lambda_B}{\lambda_A} \quad (3.4)$$

3.1.5 Determination of layer thickness of thin film

The photoemission signal can be attenuated with the upper over layer, and its intensity is directly related to the attenuation length of the photoelectron as explain¹⁴⁶ in Figure 3.4. The layer thickness of films can be evaluated by the attenuation of the Au_{4f} signal according to Lambert- Beer's law (Figure 3.4a),

$$I(d) = I_0 \cdot \exp\left(-\frac{x}{\lambda}\right) \quad (3.5)$$

$$d = x \cdot \cos \theta$$

X :	Mean free path
$\lambda_{A,B}$:	Attenuation length of a photoelectron [\AA]
I_0 :	Entrance signal intensity
$I(d)$:	Signal intensity after attenuation
Θ :	Angle of exit with respect to the surface normal
d :	Layer thickness of the substance

For $\theta = 0$ the film thickness equal to the mean free path. As gold reference, the intensity of the Au_{4f} signal of a gold. The thickness of the upper overlayer can also be calculated by a slight modification of Beer's law as explain in figure 3.4b.

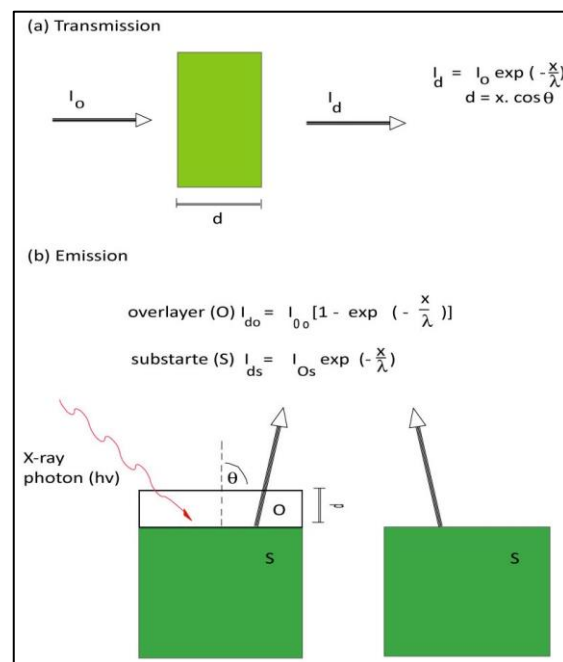


Figure 3.4 a) For electrons transmitted through a sample, Beer's law of molecular absorption explains the total intensity loss for electrons that lose no energy in traversing the sample. b) For electron emission from a thick sample, modifications of Beer's law can explain the photoemission intensity from an overlayer or from the substrate covered by an overlayer. (After ref 146)

3.2 Near edge X-ray absorption fine structure spectroscopy

Near-Edge X-ray Absorption Fine Structure (NEXAFS) spectroscopy is a surface characterization technique by evaluation of unoccupied electronic states. NEXAFS is also called X-Ray Absorption Near Edge Structure, XANES. Now a days, the term NEXAFS is typically used for soft x ray absorption spectra and XANES for hard x-ray spectra. NEXAFS refers to the details of how x-rays are absorbed by an atom at energies near the core-level binding energies of that atom. Specifically, NEXAFS is the modulation of an atom's x-ray absorption probability due to the chemical and physical state of the atom. NEXAFS spectra are especially sensitive to the formal oxidation state, coordination chemistry, and the distances, coordination number and species of the atoms immediately surrounding the selected element. Because of this dependence, NEXAFS provides a practical and relatively simple way to determine the chemical state and local atomic structure for a selected atomic species.

3.2.1 Principles

NEXAFS refers to the absorption fine structure close to an absorption edge about the first 30 eV above the actual edge. This region usually shows the largest variations in the X-ray absorption coefficient and is often dominated by intense narrow resonances. In NEXAFS, the X-ray photon energy is scanned over a core-level absorption edge, and the absorbed X-ray intensity is measured by probing the excitation of the core electron to unoccupied states.¹⁴⁸ This method requires a tunable monochromatic light source with smooth characteristics in the energy regions of interest, as well as high intensity and energy resolution, Synchrotron radiation sources are therefore well suited for NEXAFS spectroscopy.

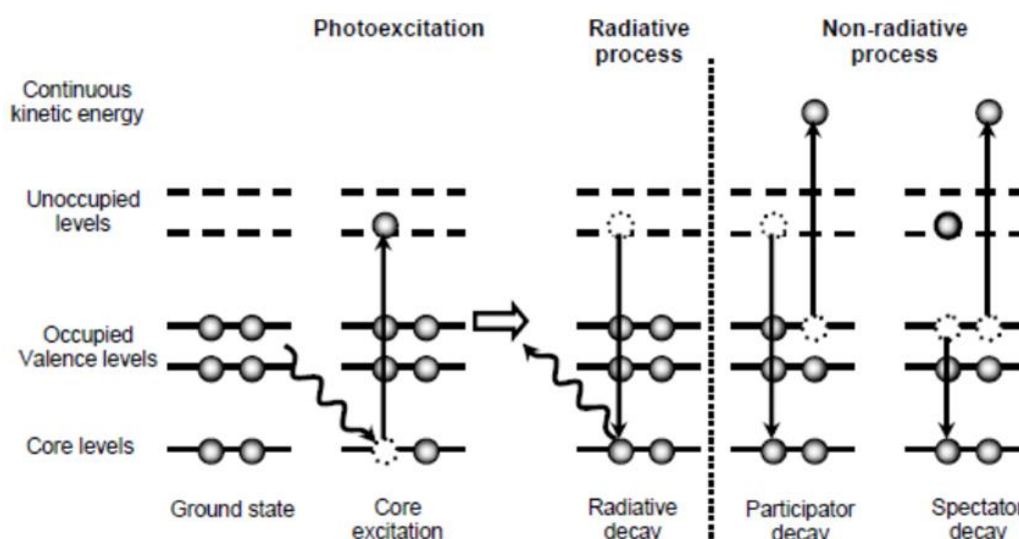


Figure 3.5 Schematic diagram of photoexcitation and recombination processes. The photon generated core hole is filled by an electron from a higher shell either radiatively by emission of a photon, or non-radiatively by emission of an Auger electron.

This technique relies on a two-step process. In the first step the photon excites a core electron to the unoccupied state, hence creating a core hole, and in the second step the

recombination process of the core hole takes place. There are many possible channels for the core hole recombination process (Figure 3.5); viz, the radiative type, producing the emission of photons (fluorescence), or the non-radiative type (Auger-like transitions), producing the emission of electrons, which can be collected from the surface with suitable detector.¹⁴⁹ In our experiment, the latter type was measured. There are two kinds of the Auger-like transitions in this case: participator decay in which the excited electron participates in the core-hole decay process and spectator decay in which the excited electron remains in the normally unoccupied level and two valence electrons are removed. The number of generated Auger electrons is directly proportional to X-ray absorption cross section.¹⁴⁸

Several techniques can be chosen to detect the absorption. The most common method is an electron yield measurement which measures the emitted electrons that are created by the absorbed X-ray. There are several ways to perform electron yield measurements: Total electron yield (TEY), Partial electron yield (PEY) or Auger electron yield (AEY). In the TEY method, all Auger electrons and photoelectrons are measured. This results in a high signal rate but a very small signal-to-noise ratio. In the PEY method, by placing a retarding voltage in front of the electron detector, a fraction of Auger electrons are measured. Because of the flexibility in choosing the retarding voltage, one can avoid the interference from the low kinetic energy electron, increasing signal-to-noise ratio. In the third method, the AEY method, Auger electrons are measured by setting the energy analyzer at a specific Auger transition energy. This method offers the largest signal-to-noise ratio of all electron-yield techniques, but the smallest signal rate. Another technique to measure the X-ray absorption spectra is a transmission measurement. This can be done by measuring the current to the sample after photons are transmitted through it. This technique requires a thin sample while the electron yield technique can be used for conventional samples. In this work, the PEY method was employed.

3.2.2 Angular dependence of NEXAFS resonance intensity

The second important property of NEXAFS spectra is that, the interaction of the X-ray radiation has a spatial anisotropy with the MOs of the sample that is, the cross section depends on the angle and direction of the transition dipole moment (TDM) of excitation (more precisely the symmetry of the unoccupied MOs and the orientation of the SAMs with respect to the surface normal). In gas phase the intensities of the fine structure obtained by linearly polarized X-ray radiation are independent of incident angle, since the orbitals are evenly distributed in all directions in space. This leads to an angle-dependent intensity distribution of the fine structure and the possibility to determine an orientation of the molecule relative to the surface. The correlation between the spatial position of an aromatic π^* system and the orientation of the incident X-ray is shown in Figure 3.6.

The system can be considered as a combination of three coordinate systems, where the substrate plane represents the main coordinate. With respect to the z-axis, on the one hand, the coordinate system of the molecule, consisting of the molecular axis and the transition dipole moments (TDMs), and on the other hand, the coordinate system of the incident X-ray radiation consisting of the direction of propagation c and the field vectors E , and B .

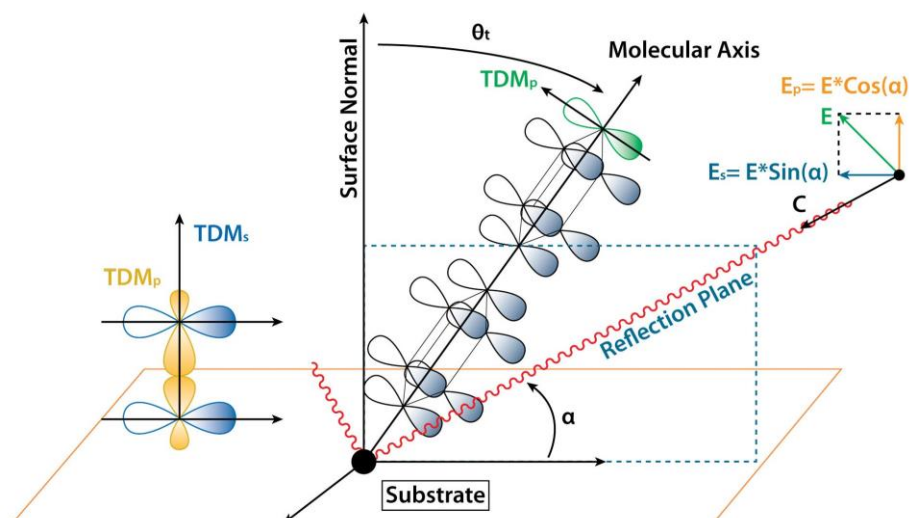


Figure 3.6 Relationship between the tilt angle Θ_t , the angle of incidence α of the X-ray radiation and intensity of the interaction. TDM are the transition dipole moments with respect to a molecular orbital, E is the electric component of the linearly polarized X-ray radiation with the direction of propagation c.

When monolayers are in parallel to π^* orbitals (and thus their TDMs) and σ^* MOs perpendicular to the substrate plane, or have an inclination corresponding to the tilt angle, mathematically, the relationship, taking into account that the molecular axis is defined only in terms of the tilt angle θ_t and assume any position in the XY-plane with the same probability for π^* -systems represented by the following equation,¹⁴⁸

$$I(\alpha, \theta_t) \propto P \cdot [1 - \cos^2 \theta_t \cdot \cos^2 \alpha - 0.5 \cdot (\sin^2 \theta_t \cdot \sin^2 \alpha)] + \left(0.5 - \frac{P}{2}\right) \cdot (1 + \cos^2 \alpha) \quad (3.6)$$

Where, A is a constant, P is the polarization factor of the synchrotron light, and θ_t is the tilt angle of the molecular orbital. For X-ray, the polarization factor, P is in the range $0 \leq P \leq 1$ and the experiments were conducted at 0.91. If P and θ are known, the intensity obtained from the measurement, the average tilt angle α of the TDM of the molecules on the surface can be determined.

3.3 Spectral ellipsometry

Spectroscopic ellipsometry is an optical method to determine the film thickness and refractive index of transparent thin films. The key feature is the measurement of changes in the polarization state of light upon light reflection on a sample (or light transition by a sample) (Figure 3.7).¹⁵⁰ The scheme of Ellipsometric setup is explain in Figure 3.8. This change is represented as the amplitude ratio Ψ and the phase difference Δ . The measured response depends on optical properties and thickness of individual materials. Thus,

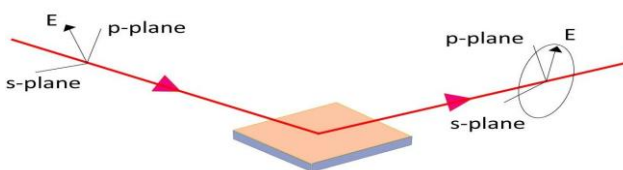


Figure 3.7 Ellipsometry working principle. The linear polarized light is reflected by the sample and gets elliptically polarized. Image inspired by ref 150.

ellipsometry is primarily used to determine film thickness and optical constants.¹⁵¹

Light can be described as an electromagnetic wave and its electric field is always orthogonal to the propagation direction. Therefore, a wave traveling along the z-direction can be described by its x- and y- components. When the light has completely random orientation and phase, it is considered to be unpolarized. When two orthogonal light waves are in-phase, the resulting light will be linearly polarized¹⁵² (Figure 3.9a). The relative amplitudes determine the resulting orientation. If the orthogonal waves are 90° out-of-phase and equal in amplitude, the resultant light is circularly polarized (Figure 3.9b). The most common polarization is 'elliptical', one that combines orthogonal waves of arbitrary amplitude and phase¹⁵⁰ (Figure 3.9c). This is where ellipsometry gets its name. The next question to be answered is what happens with polarized light moving through matter. Therefore a reflection plane has to be defined and the polarization of light is defined in terms of the spatial orientation of the electric field component E, which can be parallel (*p*-wave or transverse magnetic) or perpendicularly (*s*-wave or transverse electric) to the plane of incidence.

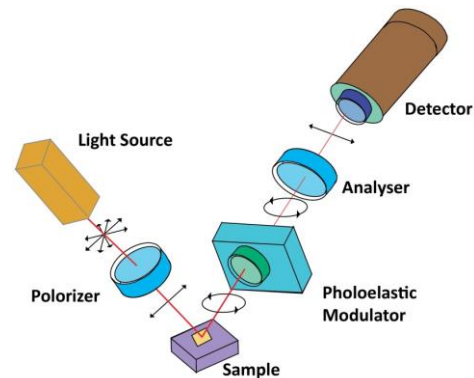


Figure 3.8 Scheme of ellipsometry setup. The source emits light which is linear polarized. After reflection from the sample the light is elliptically polarized. The light polarization direction is sorted by the rotating analyser and its intensity by the detector. The PC can collect the circular dependent intensity and calculate the layer thickness using models.

Any intermediate orientation between *s* and *p* waves can be described by a linear combination of the base vectors E_p and E_s . After reflection and interaction with the substrate, the phase of the *s*- and *p*-polarized part is shifted so that it gets elliptically polarized.¹⁵³ The change in polarization can be expressed by the ratio of the reflection coefficient ρ , which can be described by the fundamental equation of ellipsometry.¹⁵⁰

$$\rho = \left(\frac{r_p}{r_s} \right) = \tan \Psi \exp i(\Delta) \quad (3.7)$$

where $\tan(\Psi)$ is the amplitude ratio upon reflection and Δ denotes the phase shift between the *s*- and *p*-polarized wave. In general the measured values of Ψ and Δ cannot be converted directly into the optical constants of the sample. A regression analysis has to be performed, at which a layer model has to be established considering the optical constants and thickness parameters of all individual layers

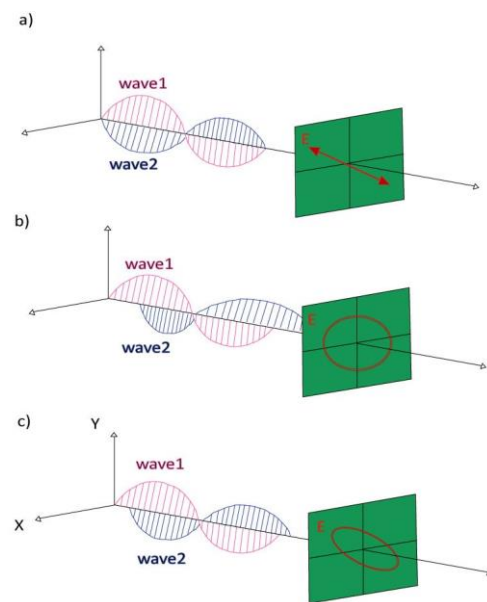


Figure 3.9 Orthogonal waves combined to demonstrate polarization: a) linear, b) circular and c) elliptical [after ref 152].

of the sample. By using an iterative procedure unknown optical constants and/or thickness parameters are varied and Ψ and Δ values are calculated using the Fresnel equation.¹⁵⁴

$$r_s = \frac{n_0 \cos \theta_0 - n_1 \cos \theta_1}{n_0 \cos \theta_0 + n_1 \cos \theta_1}, r_p = \frac{n_1 \cos \theta_0 - n_0 \cos \theta_1}{n_1 \cos \theta_0 + n_0 \cos \theta_1}, \quad (3.8)$$

The calculated Ψ and Δ values which match the experimental data best provide the optical constants from which e.g. the film thickness can be modeled. It is possible to determine film thicknesses down to the nanometer regime but in the case of multilayers each layer has to be modeled individually. For different wavelengths the optical constants of a material vary and have to be described at all wavelengths probed with the ellipsometer. A table of optical constants can be used to predict the material's response at each wavelength, but it is not convenient to adjust unknown optical constants on a wavelength-by-wavelength basis. It is more advantageous to use all wavelengths simultaneously. A dispersion relationship often solves this problem by describing the optical constant shape versus wavelength. The adjustable parameters of the dispersion relationship allow the overall optical constant shape to match the experimental results. Compared to fitting individual n and k values at every wavelength, this greatly reduces the number of unknown 'free' parameters. For transparent materials ($k = 0$), the refractive index is often described using the Cauchy relationship.¹⁵⁵

$$n(\lambda) = A + \frac{B}{\lambda^2} + \frac{C}{\lambda^4} \dots \dots \dots \quad (3.9)$$

where A, B and C are adjusted to match the refractive index of the material. One of the remarkable features of ellipsometry is the high precision of the measurement and high thickness sensitivity (0.1 Å).

3.4 Scanning electron microscopy

Scanning electron microscopy (SEM) is a widely used technique of major significance throughout the scientific and technological communities.¹⁵⁶ This microscope can achieve large magnifications by scanning the sample with a focused electron beam instead of light in a raster scan pattern. The electrons of the beam interact with the electrons in the sample and the intensity of reflected and secondary electrons produced by the incident beam can be detected and analyzed. Detection limitations, e.g. the spatial resolution d of microscopic techniques, are closely linked to the wavelength λ of the incident beam via the lens specific numerical aperture NA,

$$d = \frac{\lambda}{2.N.A} \quad (3.10)$$

This, in turn, is determined by the opening angle α of the lens and the refractive index of the medium n ,¹⁵⁷

$$N A = n \cdot \sin \alpha \quad (3.11)$$

Taking advantage of the de Broglie relation,

$$\lambda = \frac{h}{p} = h/\sqrt{2m_e E_e} \quad (3.12)$$

where λ is the electron wavelength, h Planck's constant, p the electron momentum, E_e the electron energy and m_e the electron mass, electrons are used instead of photons, achieving shorter wavelengths and thereby better resolutions.¹⁵⁸ If, for example, electrons are accelerated with 100 eV, a wavelength of 0.122nm is achieved, which is far below the wavelength of visible light applied in light microscopy. Although the use of electrons theoretically has no limitations with respect to the resolution, the spherical aberration of the lenses limits it. The key components of all SEM instrument include an electron source ('gun'), electronic lenses, a measurement chamber and a detector for all signals of interest (Figure 3.10). A beam of electrons is produced by the electron gun, a cathode emitting electrons which

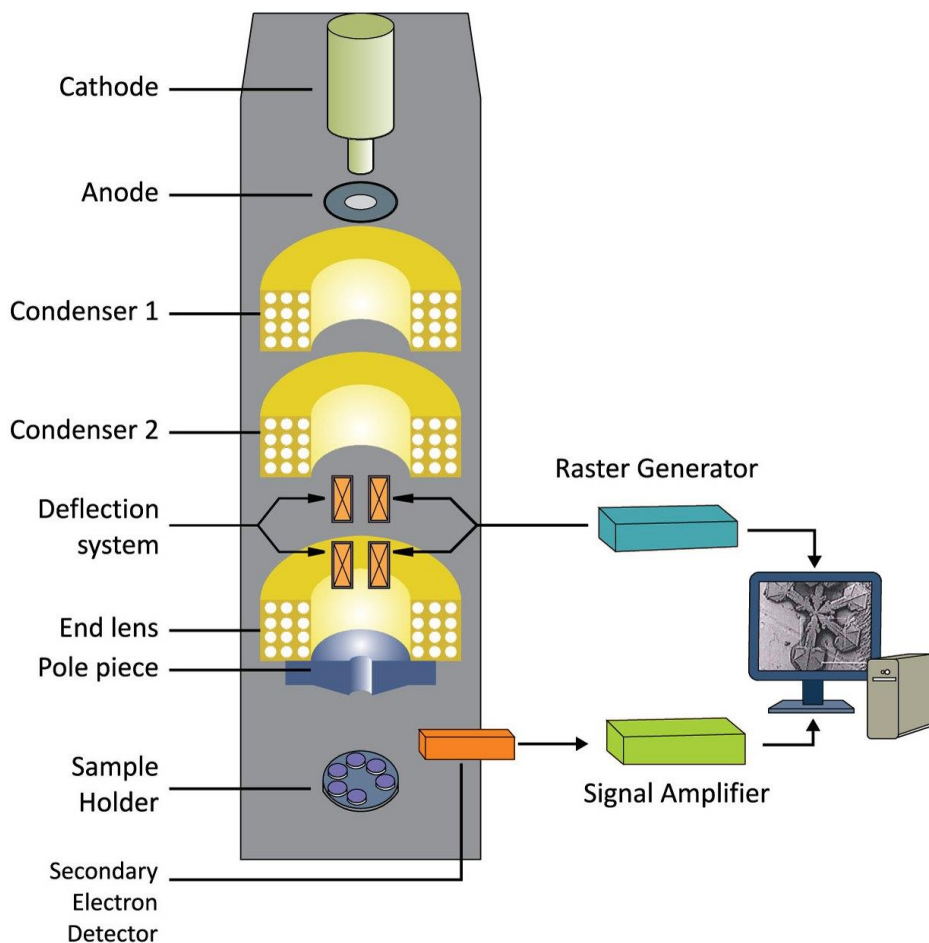


Figure 3.10 Scheme of an SEM microscope (after ref 159)).

are accelerated towards the anode.¹⁵⁹ The emission can be excited either thermally (thermodynamic emission) or by applying high voltage (field emission). In conventional electron guns, the cathode, usually consisting of tungsten (W) or lanthanum hexaboride (LaB₆), is heated until a stream of electrons is produced. The disadvantages of this system are the short lifetime of the filament and the high emission energy distribution.¹⁵⁶ The electron beam

follows a vertical path through the microscope, which is kept under vacuum. The beam travels through electromagnetic fields and lenses, which focus the beam down toward the sample and correct symmetric defects of the beam with respect to the optical axis. When primary electrons hit the surface of an object, interaction through elastic and inelastic scattering takes place. Secondary electrons (SE) and back-scattered electrons (BSE) with different energies are created, which are collected by various detectors. The penetration depth of the primary electrons depends on their energy, on the thickness and on the nature of the material.

Different detector designs are available to collect BSE or SE which generate different contrasts due to their interaction depth with the material. The inlens detector is ring-shaped and situated above the sample in the column and detects secondary electrons that are emitted back into the column. With this detector it is possible to achieve high-resolution images (in the nm range) at small acceleration voltages of the beam due to the low working distance. This makes it possible to achieve images faster and more gentle than with other detectors. Since SE generally is low energy electrons, they only emerge from the outermost layer of the sample and carry information about the material contrast with them due to the different material-dependent attenuation lengths. Another type of SE-detector is the SE2 detector which is able to achieve a topographic contrast and a high spatial resolution. Although the name is misleading, this detector detects not only SE but also few BSE. In contrast to the inlens detector the picture information here originates from deeper penetration depths. The electrons are accelerated towards the detector, are collected by a positively biased collector grid and create a number of electrical impulses. The SE2 detector is mounted at the sideways above the sample with a tilt angle of 45° and provides a very naturally, 3D image. BSE are electrons which are scattered elastically on atomic cores down to 10nm under the sample surface. The BSE detector usually is a 4-quadrant-semiconductor and since it is situated in the measurement chamber, it is important to work with a high accelerating voltage (min. 5 keV) for obtaining good signal intensity. Dependent on the circuit of the semiconductor crystals different topographic contrasts can be achieved, whereas deep areas seem to be darker. The property that heavy elements reflect the electrons more than lighter ones is used to draw conclusions from the chemical nature of the surface.

There are some limitations of Scanning electron microscopy. The samples have to be viewed in a vacuum (10^{-5} torr to 10^{-6} torr), as the air molecules would scatter the electrons. A second point is that for conventional SEM imaging the sample has to be electrically conductive, at least at the surface, and electrically grounded to prevent the accumulation of electrostatic charge at the surface. Therefore nonconductive substrates tend to charge when they are imaged by the electron beam, and especially in the secondary electron imaging mode, this causes scanning defaults and other image artifacts. They are therefore usually coated with an ultrathin coating of electrically conductive material like graphite or gold.

3.5 Atomic force microscopy

Scanning probe microscopy (SPM) was developed in 1981 at IBM, Zurich by Binnig and Rohrer with the invention of the scanning tunnelling microscope (STM).¹⁶⁰⁻¹⁶¹ These earned them Nobel Prize in Physics in 1986. The two most common forms of SPM are scanning tunneling microscopy (STM) and atomic force microscopy (AFM). The scanning tunnelling microscope is (in general) restricted to conducting materials. The surfaces of insulators, structures in liquids and biological samples can be imaged nondestructively with high resolution by the atomic force microscope (AFM) (also often scanning force microscope, SFM), which was developed in 1986 by Binnig, Quate and Gerber.¹⁶²

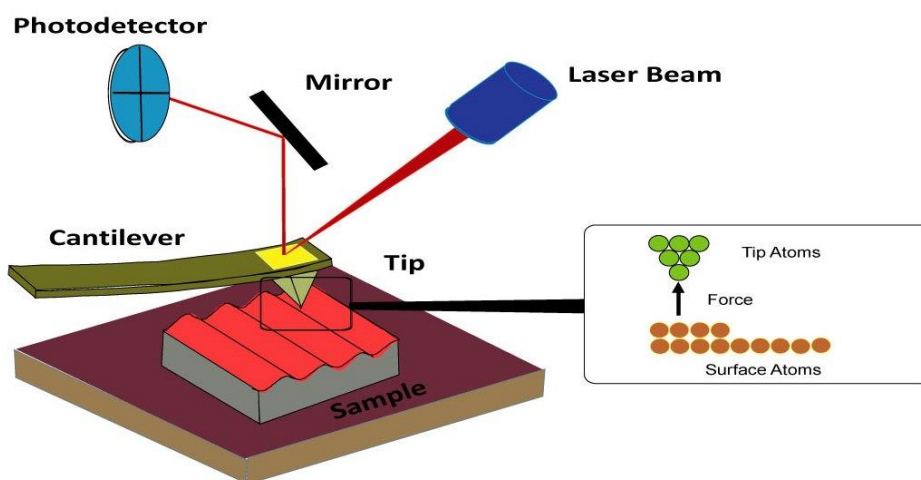


Figure 3.11 Scheme of an AFM microscope (after ref 158). The tip is attached to a cantilever, and is scanned over a surface. The cantilever deflection due to tip-surface interactions is monitored by a photodiode sensitive to laser light reflected at the tip backside.

3.5.1 Basic principles

AFM is the most commonly used tool to obtain 3D images of structured surfaces in the range of a few micrometer to single nanometers with a very high resolution. This technique exploits the fact that a tunnelling current through a potential barrier of the width d is proportional to e^{-d} (provided a constant and final height of the potential barrier). A sharp tip at the end of a cantilever is scanned over the substrate, which detects ultras-small forces (less than 1 nN) present between the tip and the surface.¹⁶³ The topography of the substrate causes deflections of the cantilever and goes along with changing interactions between the tip and the surface, such as van der Waals or electrostatic forces. A visible laser beam is reflected from the backside of the cantilever to a detector, also called position sensitive device (PSD), so that very small deflections of the substrate can be observed (Figure 3.11).¹⁵⁸ The obtained line deflection can be combined together to topographic images of the substrate.

3.5.2 Imaging modes

There are three different operation modes in AFM, namely the contact, noncontact and tapping mode.¹⁶⁴ In the contact or static mode the tip is brought into direct physical contact

with the sample.¹⁶⁵ The topographical information is detected and transferred to a piezoceramic element which adjusts the cantilever in a way that the force acting on the surface stays constant. This is called 'feedback loop'.¹⁶³ As the tip scans across the surface, varying topographic features cause deflections of the cantilever, which are measured and visualized as image information. The disadvantage of this mode is that the constant force can deform soft biological samples or material can be wiped away or smeared over of the surface. To avoid these effects, the non-contact or dynamic mode can be used. In this mode the cantilever oscillates above the sample at its resonance frequency. When the tip gets closer to the surface, very weak van der Waals attractive forces change the oscillation amplitude of the tip. These changes can be detected and used to generate an image.¹⁶⁴ In this mode the tip-substrate interactions are very small and the lateral resolution is lower than in other operation modes. However, the greatest drawback is that it can only be used on dry samples. A small water layer disturbs the detachment of the tip from the sample because of the small oscillating amplitude.¹⁶⁶ In the tapping mode, the cantilever is driven to oscillate up and down near its resonance frequency.¹⁶⁷ When the tip gets closer to the surface, van der Waals forces, dipole-dipole interactions, electrostatic forces, etc. interact with the cantilever and with this change the amplitude and the phase of the oscillation. Mostly, this change in the amplitude is used to regulate the signal during the scan process. This means piezoceramics are used to control the height of the cantilever to keep the amplitude constant. Due to the fact that shear forces are eliminated and vertical forces are reduced significantly, this mode is advantageous to investigate sensitive materials (e.g. biological surfaces) or unstable surface features (e.g. small particles).¹⁶⁸

3.6 Contact angle goniometry

Contact angle goniometry is a technique to determine the wettability of solid surfaces by liquids.¹⁶⁹ It is very sensitive to the molecular structure of the underlying substrate and the contact angle (CA), Θ can vary from 0° to 114° dependent on the surface chemistry of the substrate.¹⁷⁰ It is defined as the angle between the tangent to the solid-liquid interface and the tangent to the liquid-gas interface (Figure 3.12).¹⁷¹ A small contact angle displays a high wettability and therefore a strong interaction of the liquid with the solid. There are different models describing the CA closest to reality, also called apparent CA. More than 200 years ago, Young described the forces acting on a liquid droplet spreading on an ideal surface.¹⁷²

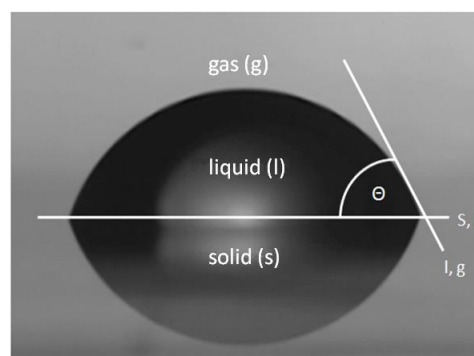


Figure 3.12 Schematic description of the contact angle.

The Young CA Θ_Y

$$\Theta_Y = \frac{\gamma_{sl} - \gamma_{sg}}{\gamma_{lg}}, \quad (3.13)$$

where γ_{sl} , γ_{sg} and γ_{lg} are the solid-liquid, solid-gas and liquid-gas interfacial tensions respectively, describes the physico-chemical nature of the wetting system. However, equation 3.13 is a clear oversimplification of the real situation, since it is only valid for atomically smooth and chemically homogeneous surfaces which do not change their characteristics due to interactions with the liquid. On real surfaces that are rough or contaminated, the local CA varies from place to place on the surface. This means that the adhesion energy varies locally and the liquid has to overcome local energy barriers in order to wet the surface. One consequence of these barriers is the CA hysteresis.¹⁷³ The extent of wetting, and therefore the observed CA, depends on whether the liquid is advancing or receding on the surface. The value of Θ classifies whether a substrate is hydrophilic ($\Theta < 90^\circ$) or hydrophobic ($\Theta > 90^\circ$). Extremes of both categories are the superhydrophobic and superhydrophilic surfaces. The latter one is particularly interesting as it characterizes surfaces that are nearly completely non-wettable ($\Theta > 150^\circ$) (Figure 3.13a).¹⁷⁴ Not only the chemical composition influences the contact angle, but also Surface structure has an impact on the wetting behavior and two different regimes can be described. In the Wenzel regime the liquid wets the surface, but the measured CA differs from the 'true' one.

The Wenzel CA, Θ_W ,

$$\cos \Theta_W = r \cos \Theta_Y, \quad (3.14)$$

is determined by the surface roughness ratio r , which is defined as the ratio between actual and projected surface area ($r = 1$ for smooth surfaces, $r > 1$ for rough surfaces) and the Young

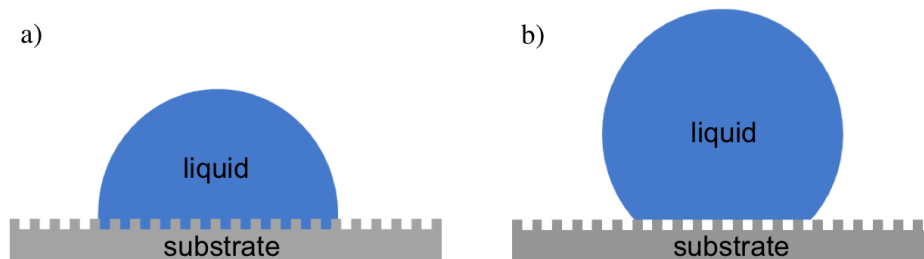


Figure 3.13 Scheme of the Wenzel (a) and the Cassie-Baxter (b) principle. In the Wenzel model the surface roughness contributes to the contact angle. In the Cassie-Baxter model the droplet does not fully wet the substrate due to surface roughness. (inspired by 171).

contact angle Θ_Y of a flat surface from the same material. Equation 3.14 predicts that in this wettability regime the hydrophobicity is enhanced by roughness ($\Theta_W > \Theta_Y$) when Θ_Y is larger than 90° . On the other hand, hydrophilicity is increased by roughness when Θ_Y is smaller than 90° .¹⁷³

When the surface is made of small pillars, which cannot be filled by the liquid and thus stay filled with air, the wettability enters the Cassie-Baxter regime¹⁷⁵ (Figure 3.13b) and can be described by

$$\cos \Theta_C = \varphi(\cos \Theta_Y + 1) - 1. \quad (3.15)$$

Here the Cassie CA Θ_C is dependent on the surface contact fractions φ of the liquid droplet and the surface characteristic contact angle Θ_Y . However, since the pores are filled with air, which is hydrophobic, the CA always increases, relative to the behavior seen on a flat substrate with identical chemical composition. Hence, it has to be considered that surface morphology can have an effect on the wettability of the substrate.

4. Fabrication of ssDNA/oligo(ethylene glycol) monolayers and complex nanostructures by irradiation promoted exchange reaction

The macromolecular structure of DNA, its ability to hybridize, the diversity of unnatural nucleotides with unique functional groups that are available to perform chemistry on it and enzymes that are available to manipulate its sequence, structure and topology provide rich opportunities for its use in clinical diagnostics, biosensors, gene therapy and drug delivery.¹⁷⁶⁻¹⁷⁸ Some of these applications rely on the immobilization of single-stranded (ssDNA) onto a solid support, which is subsequently used for binding and detection of its complementary ssDNA target or for the recognition of DNA binding proteins.^{57,76} A commonly used method for immobilization of ssDNA is to functionalize it with a terminal reactive group that is selective for a surface of interest.^{57,76} The hybridization activity of supported ssDNA depends on the packing density and molecular organization which can be tuned by mixing ssDNA with other diluent molecules that present the same reactive group.^{57,179-180} For gold, the diluent molecules of choice are short-chain alkanethiols (ATs)^{57,181-184} or thiolated oligo(ethylene glycol)s (OEG-ATs).^{46,185-189} OEG-ATs are especially attractive for applications wherein the DNA comes into contact with complex biological fluids because of their ability to resist the adsorption of proteins. Strategies to prepare such mixed films include co-deposition,^{46,185,189} backfilling,¹⁹⁰ and post-deposition by substitution.¹⁸⁸ In an alternative approach, ssDNA can be covalently conjugated to a terminal reactive functional group presented by the monolayer. OEG-ATs are also frequently used to provide a protein-repelling background to ssDNA patterns. These patterns are usually prepared by one of the standard techniques such as microcontact printing, UV lithography, or drop casting by a syringe or microarrayer.^{73,190} The preparation of the OEG-ATs background typically occurs by backfilling after deposition of the ssDNA on the surface.

In this chapter a new and potentially universal approach to prepare both mixed ssDNA/OEG-AT films in a broad range of compositions and based on this mixing ssDNA/OEG-AT patterns of arbitrary form are described. The approach relies on irradiation promoted exchange reaction (IPER) and electron beam lithography (EBL). Generally, IPER enables to control the extent and rate of the molecular exchange between the primary monolayer and a potential substituent by electron irradiation of the monolayer with a suitable dose.⁴⁵ The strength of the approach is demonstrated by combining it with surface-initiated enzymatic polymerization (SIEP) and sculpturing complex DNA nanostructures. A primary monolayer of a OEG-AT compound, HO(CH₂CH₂O)₃(CH₂)₁₁SH (termed EG3) and thiolated homooligonucleotide, 5'-SH-(CH₂)₆-d(A)₂₅-3' (termed A25SH) were taken as test systems for the experiments.

ssDNA compounds	Description
A25SH	thiol-C6-5'-AAAAAAAAAAAAAAAAAAAAAAAAAAAA-3'
A25	5'-AAAAAAAAAAAAAAAAAAAAAAAAAAAA-3'
T25	5'-TTTTTTTTTTTTTTTTTTTTTTTTTTT-3'

4.1 Preparation and characterization procedures

4.1.1 Preparation of mixed A25SH/EG3 films and patterns by IPER-EBL

A detail description of EG3 and A25SH SAMs preparation can be found in chapter 10. The EG3 films were either homogeneously irradiated (IPER; mixed A25SH/EG3 films and homogeneous poly(A) brushes) or patterned by a focused electron beam (IPER-EBL; A25SH/EG3 and poly(A) nanostructures). Homogeneous irradiation was performed with 10 eV electrons provided by a flood gun, and the doses were estimated by multiplication of the exposure time with the current density ($\sim 22 \mu\text{A}/\text{cm}^2$). EBL was performed by a LEO 1530 scanning electron microscope with a Raith Elphy Plus Pattern Generator System. The e-beam energy was chosen at 1 keV. Exchange reactions were carried out by immersion of irradiated EG3 films in a $3 \mu\text{M}$ solution of A25SH in 1 M CaCl_2 -TE buffer (1 M CaCl_2 , 10 mM Tris-HCl, 1 mM EDTA, pH 7.0) for 3 h at a temperature of 37°C . After immersion, the samples were carefully rinsed with Millipore-grade water, sonicated for 60 s followed by rinsing with water for 60 s to remove loosely bound ssDNA species. Finally, they were blown dry in an Argon stream. Non-irradiated EG3 films were immersed in A25SH as well, to check so called zero dose exchange reaction.¹⁸⁵ The possibility of exchange with A25 was checked, under the same conditions as in the case of A25SH. Further, the adsorption of A25 on the bare Au substrate was monitored, under the same conditions as in the case of the EG3 functionalized substrates.

4.1.2 Hybridization experiments

Hybridization experiments were performed in accordance with literature protocols.^{57,76} Briefly, one component A25SH and mixed A25SH/EG3 films intended for hybridization were placed in a $3 \mu\text{M}$ solution of T25 in 1 M TE-NaCl buffer for 8 h under static conditions. Afterwards, the samples were then rinsed with the buffer for 1 min to remove excess and weakly bound ssDNA strands, followed by rinsing with 1 mL of Milli-Q water (resistivity $> 18.2 \text{ M}\Omega \text{ cm}$) and dried with stream of argon.

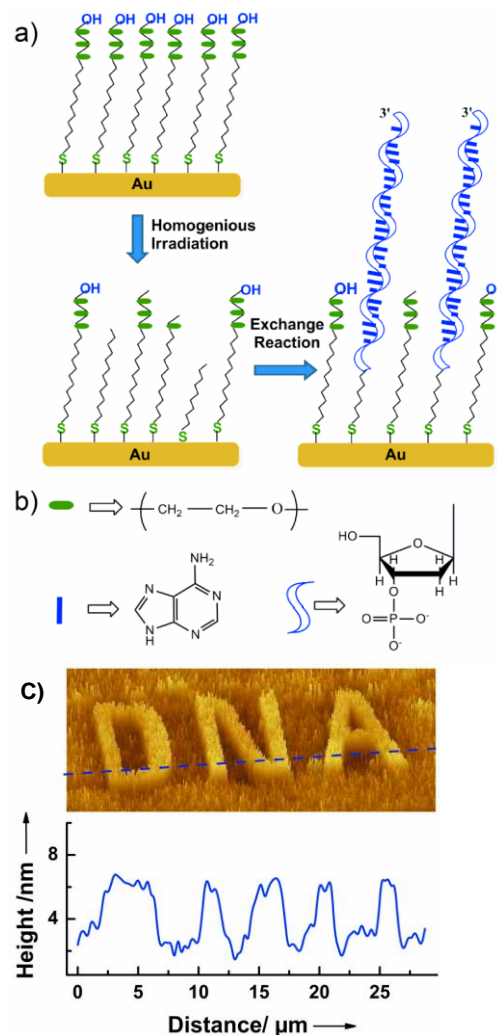


Figure 4.1 a) Schematic illustration of the approach. Irradiation-induced defects in the primary OEG-AT matrix promote an exchange reaction with the ssDNA substituents. Irradiation can be performed homogeneously, resulting in mixed ssDNA/OEG-AT monolayers of controlled composition (a), or by EBL, resulting in patterned ssDNA/OEG-AT features imbedded in biologically inert matrix (c); b) chemical formula of monolayer components; c) AFM image of a representative A25SH/EG3 pattern prepared by IPER-EBL together with the height profile along the line shown in the image (5 s; $18 \times 30 \mu\text{m}^2$).

4.1.3 Fabrication of ssDNA brushes

A detail description of growth of polymer brushes on mixed A25SH/EG3 templates and A25SH/EG3 patterns can be found in chapter 10. Substrates bearing A25SH and A25SH/EG3 films as well as A25SH/EG3 patterns were exposed to SIEP reaction which comprises of 0.1 U/ μ l TdT, 100 μ M dATP and 0.1% Tween 20 in 1x TdT buffer (100mM potassium cacodylate, 1 mM CoCl₂, and 0.2 mM DTT, pH 7.2) for 1 h at 37°C. The samples were then rinsed in 1x PBS buffer with 0.1% Tween 20, followed by rinsing with Milli-Q water (resistivity > 18.2 M Ω cm) and dried with stream of nitrogen.

4.2 Results and discussion

The procedure is illustrated in Figure 4.1a. A primary monolayer of a test OEG-AT compound, EG3 (show protein-resistance^{59,191}) was irradiated with electrons homogeneously or in the EBL fashion resulting in preferential damage of the OEG chain and cleavage of thiolate-gold bonds.^{39,59} Next, the film was incubated in a solution of a thiolated homooligonucleotide, A25SH for the exchange reaction promoted by the above defects. EBL was used to visually demonstrate the efficiency of IPER in substituting A25SH in an EG3 matrix. AFM and optical microscopy clearly shows the formation of a nanoscale A25SH pattern against a bio repulsive background of the EG3 that spells DNA (Figure 4.1c). ssDNA stems protrude clearly (by 4-5 nm) over the EG3 matrix forming their own name.

Laboratory XPS was used to monitor the outcomes of IPER and hybridization experiments. The measurements were performed using Mg K α X-ray source and a LHS 11 analyser. One component and mixed monolayers were additionally characterized by high-resolution XPS (HRXPS) at the MAX lab, Sweden. Homogeneous poly(A) brushes were characterized by synchrotron-based XPS at BESSY II in Berlin, Germany. One component and mixed monolayers were additionally characterized by NEXAFS spectroscopy at the MAX-lab synchrotron radiation facility. Homogeneous poly(A) brushes were characterized by NEXAFS spectroscopy at BESSY II. A detail description and used experimental parameter can be found in chapter 10.

4.2.1 Characterization of the A25SH/EG3 films: XPS

The proportion of the A25SH component in the mixed A25SH/OEG monolayer can be precisely controlled by selection of the irradiation dose. As shown in Figure 4.2a, N1s photoemission (PE) spectra of the one-component A25SH monolayer and mixed A25SH/EG3 films prepared by IPER exhibit characteristic two-peak signature of adenine at 399.3 and 401.1 eV^{55,76} and the intensity of this signal increases with increasing irradiation dose, demonstrating the respective increase of the A25SH component in the film (Figure 4.3). Significantly, no exchange occurs without irradiation as seen by the lack of the characteristic adenine signal for

the control, non-irradiated sample (0 mC/cm²) in Figure 4.2a. The thiolate anchoring of A25SH to gold in the mixed monolayers was proven by another control experiment where an irradiated EG3 film was exposed to non-thiolated homo-oligonucleotide (A25) as the substituent in IPER. No adenine signal was detected from this sample (second spectrum from the top in Figure 4.2a). At the same time, in accordance with literature data,⁵⁵ A25 is capable to bind directly on Au (the top spectrum in Figure 4.2a), but this does not occur when the gold is passivated and obscured by EG3 film (even after the irradiation) because of the large steric requirement to bind A25 to gold as compared to a gold-thiolate bond.⁵⁵ However, even in the case of thiolated ssDNA, its cross-section

(~154 Å²;) is significantly larger than that of the OEG-AT species (~21.4 Å²), which suggests that every exchange event within the IPER framework involves several SAM constituents. The most probable scenario is that the damaged OEG-AT species, which are only few in the given dose range, serve as initiator sites for the exchange reaction, which, driven thermodynamically, is initially mediated by the alkanethiol tail (no IPER for A25) and later involves partial squeezing or expelling of the neighbouring OEG-AT species.

4.2.2 Characterization of the A25SH/EG3 films:

NEXAFS spectroscopy

Further evidence for the formation of high-quality A25SH/EG3 monolayers is provided by NEXAFS spectroscopy. As shown in Figure 4.2b, N K-edge spectra of the mixed films exhibit characteristic π^* resonances of adenine at ~399.4 and ~401.3 eV,^{76,192} mimicking the spectrum of the one-component A25SH monolayer. The C K-edge NEXAFS spectra of the mixed films can be reproduced as linear combinations of the spectra of the both constituents, viz. EG3 and A25SH (Figure 4.4), which shows that their electronic structures are not affected by the mixing. The spectra of the mixed EG3/A25SH films represent linear combinations of the

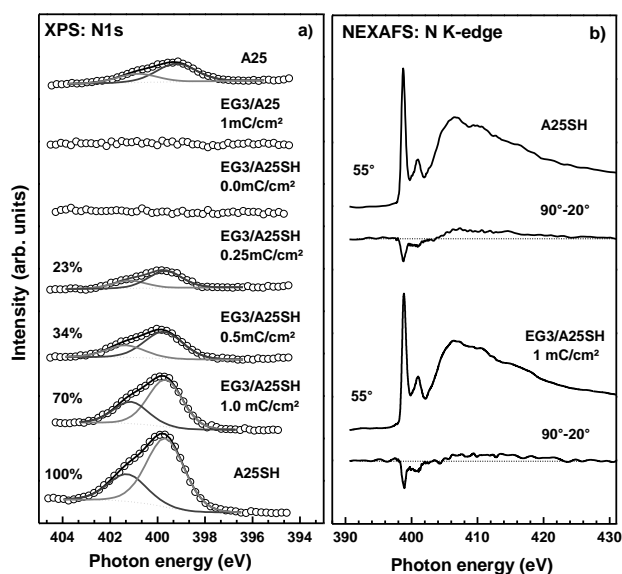


Figure 4.2 a) from bottom to the top: N 1s PE spectra of the reference A25SH monolayer, mixed EG3/A25SH films prepared by IPER at different doses, non-irradiated (0 mC/cm²) EG3 monolayer exposed to A25SH, irradiated (1 mC/cm²) EG3 monolayer exposed to A25, and Au substrate exposed to A25. The proportions of A25SH in the reference and mixed films are given at the respective curves. b) N K-edge NEXAFS spectra (55°) of the reference A25SH monolayer and mixed EG3/A25SH film prepared by IPER (1 mC/cm²) along with the respective difference (90°-20°) spectra.

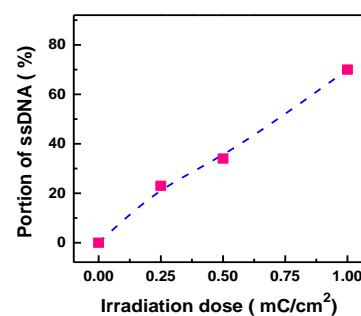


Figure 4.3 A25SH content in the mixed EG3/A25SH films prepared by IPER as a function of irradiation dose. The content increases progressively, in an almost linear fashion, with the dose

spectra of the both constituents, viz. EG3 and A25SH. The relative weights of the respective contributions vary in accordance with the expected film composition. Furthermore, the N K-edge NEXAFS spectra of the mixed films exhibit noticeable linear dichroism, similar to the spectra of the one-component A25SH monolayer, as manifested by the differences between the spectra acquired at the normal (90°) and grazing (20°) incidence angles of X-rays in Figure 4.2b. The negative peaks at the positions of the π^* resonances of adenine indicate a parallel-to-the-substrate orientation of the nucleobases,^{76,148} corresponding to an upright orientation of the DNA strands both in the one-component A25SH monolayer and most importantly, in the mixed A25/EG3 films prepared by IPER.

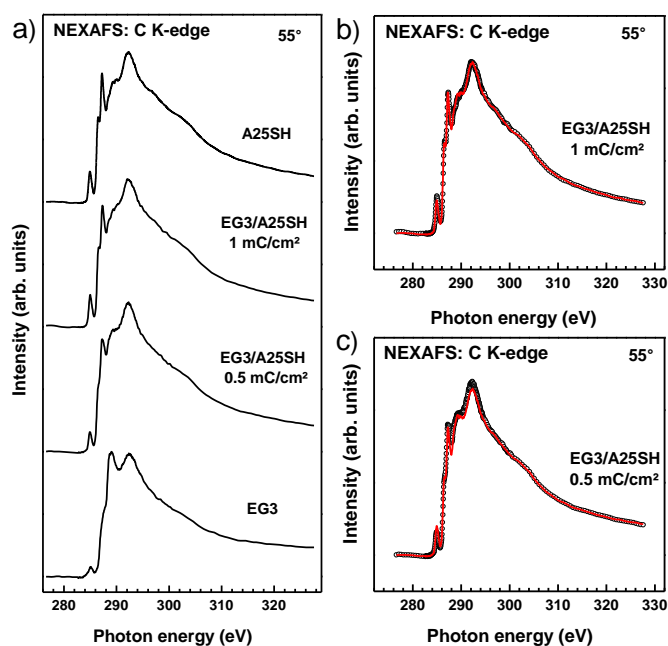


Figure 4.4 a) C K-edge NEXAFS spectra (55°) of the reference A25SH (top) and EG3 (bottom) monolayers as well as mixed EG3/A25SH films prepared by IPER with the doses given at the spectra. b) fits of the spectra of the mixed films (black) by a linear combination of the spectra of the individual components (red). The relative weights of the A25SH and EG3 spectra are 50% and 50% at 0.5 mC/cm² and 80% and 20% at 1 mC/cm²

4.2.3 Hybridization ability of mixed A25SH/EG3 films

The mixed A25SH/EG3 films generated by IPER were tested for hybridization by exposing them to their complementary d(T)₂₅ strand, that is abbreviated as T25. This exposure

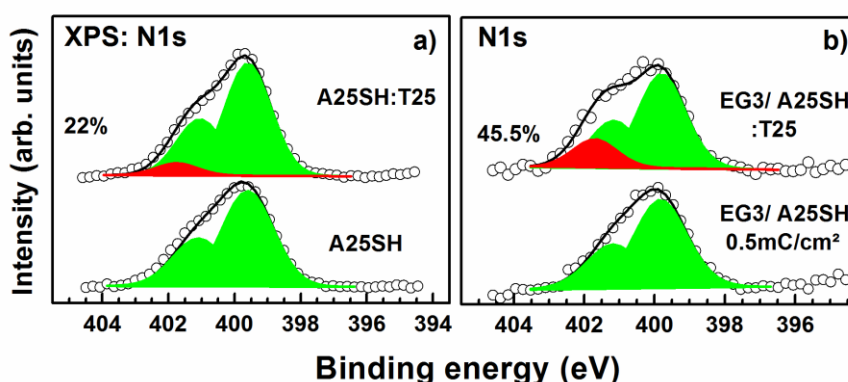


Figure 4.5 N 1s PE spectra of the reference A25SH monolayer (a; bottom curve) and mixed EG3/A25SH film fabricated by IPER with a dose of 0.5 mC/cm² (b; bottom curve) along with the spectra of the same films after the hybridization with T25. The spectra are decomposed into individual contributions which are shaded green and dark red for adenine and thymine, respectively. Note that the spectra in the bottom traces were used as references for the decomposition of the spectra in the top traces.

resulted in the appearance of the characteristic emission of thymine (T) at ~ 401.0 eV in the N 1s PE spectra^{55,76} as shown in Figure 4.5b. The degree of hybridization was estimated at $\sim 45.5\%$ for the A25SH/EG3 monolayers prepared by IPER with a dose of 0.5 mC/cm². The efficiency of hybridization for this monolayer is much higher than that of the one-component A25SH film ($\sim 22\%$) (Figure 4.5a). This behaviour can be attributed to the lower packing density of the ssDNA strands in the mixed films, which improves the steric access and diminish electrostatic repulsion.

4.2.4 Characterization of ssDNA Brush

The above results demonstrate that mixed A25SH/EG3 monolayers of desirable composition can be successfully fabricated by IPER as far as irradiation is performed homogeneously and the dose is controlled. Then IPER was adapted in combination with EBL to fabricate complex nanopatterns of A25SH embedded in a protein-resistant EG3 matrix (Figure 4.1c). Using these patterns as the template, these were grown in the z -dimension into 3D DNA nanostructures by using the 3'-ends of the surface-bound ssDNA (A25SH in this case) as initiation sites for SIEP of DNA by an enzyme, terminal deoxynucleotidyl transferase (TdT).⁷²⁻⁷³ This step exploits the ability of TdT to sequentially add mononucleotides (Adenine (A) in this case) to the 3'-end of a ssDNA,¹⁴⁴ and the polymerization of DNA, which can be tuned from a few to several thousand bases.⁷⁴ It was found that the density of ssDNA controls the feature height that is observed in the z -direction; for patterned regions with a high density of the initiator strands, the growing chains form a DNA brush with significant height, while a low density of initiator resulted in chains that are not confined, forming a structure with lower height.³⁷ For constant reactant concentration and time during SIEP, the height of the DNA brush should be proportional to the amount of A25SH in the mixed A25SH/EG3 films, as is indeed the case (Figure 4.6). The height increases progressively with the irradiation dose, following the content of A25SH in the mixed EG3/A25SH films. The identity and contamination-free character of the poly(A) brush is manifested by the characteristic P 2p emission of ssDNA at 134.1 eV,⁵⁶ characteristic π^* resonances of adenine in the N K-edge NEXAFS spectra (Figures 4.7 and 4.8). No brush-related features or signals from phosphorus containing contamination were observed for the one-component EG3 film (top spectrum, Figure 4.7), even after its exposure to A25SH solution (without preliminary irradiation, i.e. at 0 mC/cm²; top but one spectrum). No exchange occurs without irradiation (Figure 4.2a) so that the A25SH species, serving as initiators for the poly(A) brush growth, are not available. In addition, the EG3 substrate is contamination-free, which is presumably related to its protein-repelling properties.

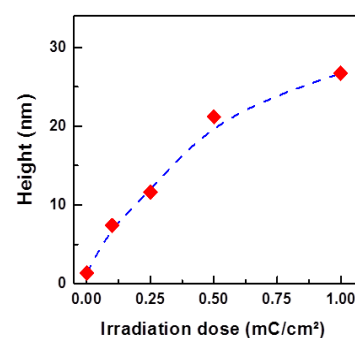


Figure 4.6 The ellipsometric height of homogeneous poly(A) brushes grown on EG3/A25SH substrates prepared by IPER as a function of irradiation dose.

The spectra of the brushes grown on the A25SH and EG3/A25SH substrates exhibit the characteristic π^* resonances of adenine at 399.4 and 401.3 eV (Figure 4.8).^{56,192} The intensity of the signal does not change for the thick brushes and is somewhat smaller for thinner brushes for which the saturation of the partial electron yield (PEY) signal is not achieved. Not

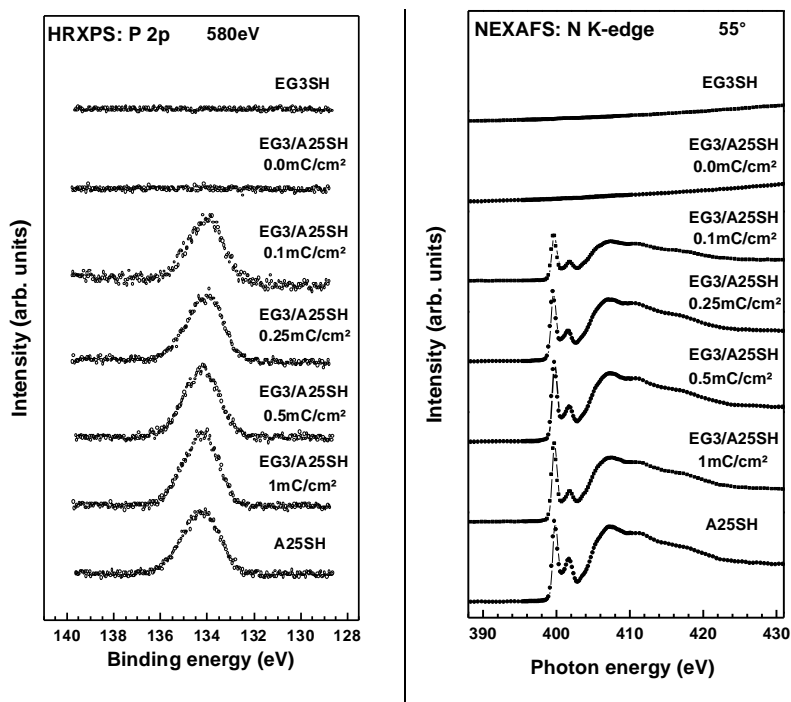


Figure 4.7 P 2p XPS spectra of homogeneous poly(A) brushes grown on the A25SH (bottom), EG3 (top), and EG3/A25SH substrates prepared by IPER with a dose written at the respective curves. The spectra of the brushes grown on the A25SH and EG3/A25SH substrates exhibit the characteristic P 2p emission of ssDNA at 134.1 eV.

Figure 4.8 N K-edge NEXAFS spectra of homogeneous poly(A) brushes grown on the A25SH (bottom), EG3 (top), and EG3/A25SH templates prepared by IPER with a dose written at the respective curves.

that the characteristic attenuation length of the PEY signal is longer than that of photoemission signal of the comparable kinetic energy,¹⁹³ so that the complete saturation of the former signal does not occur for the thinner films and the changes in the brush thickness can be partly monitored. No brush related features or signals from nitrogen containing contamination were observed for the one-component EG3 film (top spectrum Figure 4.8), even after its exposure to A25SH solution (without preliminary irradiation, i.e. at 0 mC/cm²; top but one spectrum). No exchange occurs without irradiation so that the A25SH species, serving as initiators for the poly(A) brush growth, are not available. In addition, the EG3 substrate is contamination-free, which is presumably related to its protein-repelling properties.

4.2.5 ssDNA patterns on EG3 templates

The new approach enable nanofabrication of DNA nanostructures of arbitrary shape in an EG3 matrix by EBL-IPER followed by SIEP, as shown in Figure 4.9 -4.13, where several representative examples of poly(A) nanostructures are presented. Importantly, the ability to introduce gradients in the surface concentration of the A25SH by IPER allows the formation of nanostructures with a structural complexity that is not possible by other nanofabrication methodologies. The “DNA” letters, wedges, and cone-like columns in Figures 4.9a, 4.9b and 4.9c were designed and fabricated as gradient-like brushes; the respective height profiles

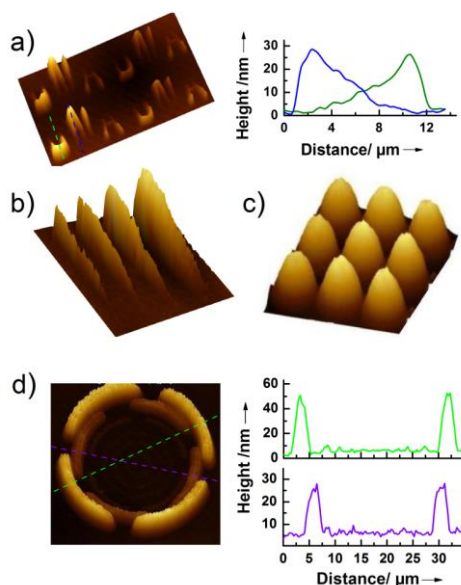


Figure 4.9 AFM images (3D view) of representative poly(A) brush patterns grown by SIEP on the EG3/A25SH templates prepared by IPER-EBL and the height profiles (for a and d) along the lines of the respective colour shown in the images. a) contrary running gradient-like “DNA” letters; b) wedges with widths of 2, 1, 0.5, and 0.25 μm ; c) cone columns (this shape was intentionally sculptured by gradient-like template); d) a microscale “amphitheatre”. The size of the images is 36 x 63, 20 x 30, 27 x 30, and 34 x 35 μm^2 for a, b, c, and d, respectively. It took 22, 5, 54, and 14 s, respectively, to write these patterns.

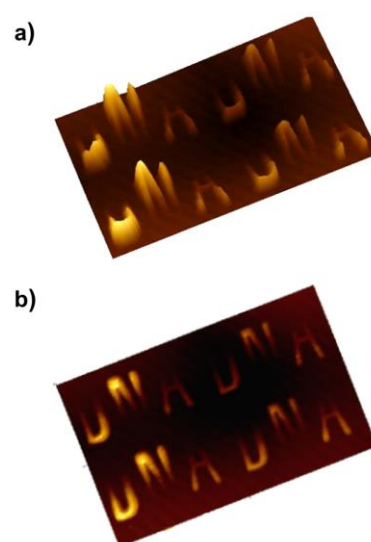


Figure 4.10 AFM images of a representative poly(A) brush patterns grown on the EG3/A25SH templates prepared by IPER-EBL. The brush represents an assembly of contrary running gradient-like “DNA” letters. Comparison of the 3D (a) and top (b) view. It is the same brush which is presented in Figure 4a. The size of the images is 36 x 63 μm^2 .

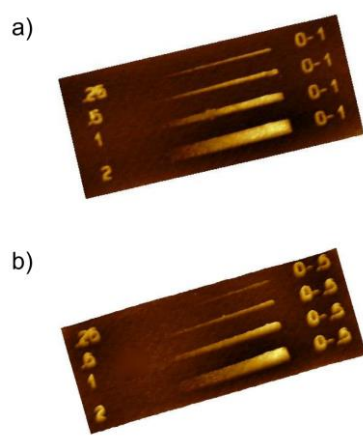


Figure 4.11. AFM images of poly(A) brush patterns in form of gradient-like wedges grown on the EG3/A25SH templates prepared by IPER-EBL (at the top). The width of the wedges (in μm) is “written” on their left side while the dose range (from-to; in mC/cm^2) is “written” on their right side. These are 3D images presented in almost normal view geometry to make the numbers visible. 3D character of the wedges can be better seen in Figure 4.9b which presents the same pattern as in (a) but the view angle is different. The size of the images is 22 x 52 μm^2

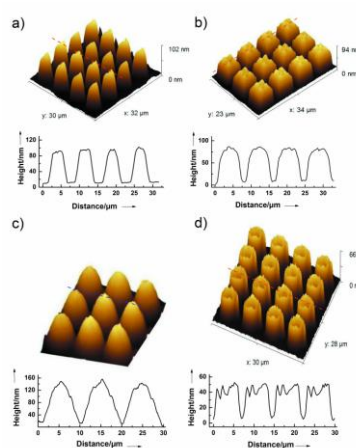


Figure 4.12 AFM images (3D view) of several representative poly(A) brush patterns grown on the EG3/A25SH templates prepared by IPER-EBL (at the top) together with the height profiles (at the bottom) along the dashed lines shown in the images. a) triangle “knives”; b) columns with engineered top face; c) cone-like columns - the same brush which is presented in Figure 4.9c; d) columns with helix-like engineered top face

(Figure 4.9a) agree well with the ellipsometric height of the homogeneous brush in Figure 4.6. The “amphitheatre” in Figure 4.9d is an example of an even more complex nanostructure. The maximum height of the brush patterns was ~ 150 nm (Figure 4.9c), which can be precisely controlled by two orthogonal experimental parameters: (1) the density of the A25SH moieties that is itself controlled by the irradiation dose in IPER, and whose 3' ends serve as initiation sites for (2) SIEP, the experimental conditions of which, viz. nucleotide concentration, enzyme to nucleotide ratio and reaction time, control the chain length of each DNA strand.

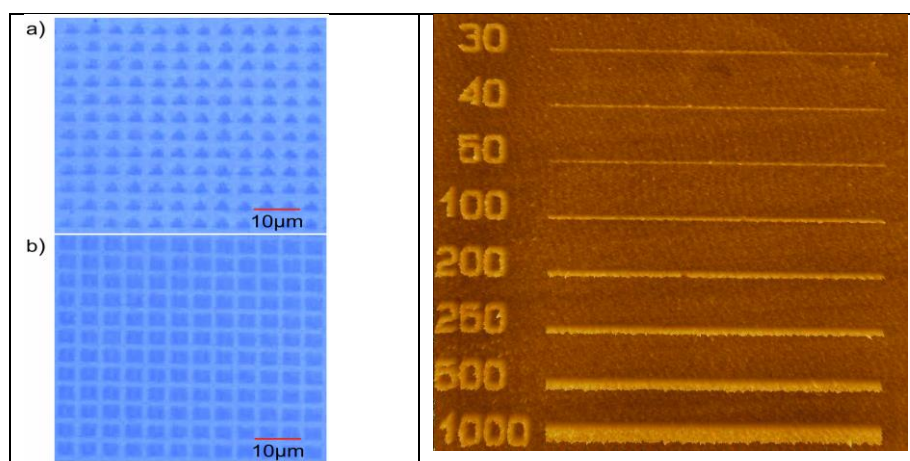


Figure 4.13 Large-scale, optical images of two representative poly(A) brush patterns grown on the EG3/A25SH templates prepared by IPER-EBL. (a) triangle “knives” and (b) columns with engineered top face. The AFM images of these patterns are presented in Figures 4.12a and 4.12b, respectively.

Figure 4.14 AFM image of the EG3/A25SH pattern prepared by IPER-EBL (1 mC/cm^2). The width of the lines (in nm) is “written” on their left side. The size of the images is $40 \times 37 \mu\text{m}^2$.

This process is somewhat analogous to photographic development in that the “negative” written by EBL in the EG3 matrix is “developed” by exchange with A25SH, and the fabricated A25SH pattern is then “amplified” by SIEP, becoming poly(A) 3D nanostructures embedded in EG3 “background”. Note that brush structures exhibit a slight expansion as compared to the template pattern, which becomes essential for the nm range, putting certain limitations on the lateral size and height of these structures.^{73,194} As for the template patterns, features down to 30-50 nm can be easily fabricated (Figure 4.14).

4.3 Conclusions

A universal two-step procedure to fabricate mixed ssDNA/OEG-AT monolayers and patterns on gold substrates is presented here. The procedure is based on IPER and relies on commercially available compounds – making it easily accessible to researchers – and is highly flexible in terms of the composition of the mixed monolayers as well as the size and shape of the ssDNA patterns that can be formed on the OEG-AT background. The approach is not limited to the compounds used herein but can be presumably implemented with almost any combination of a protein-repelling OEG-AT SAM and thiolated ssDNA. The strength of the approach is demonstrated by its combination with TdT-catalyzed SIEP that allows amplifying

ssDNA/OEG-AT patterns in the z-direction. This combination provides a new methodology to sculpt complex 3D DNA nanostructures on solid supports.

5. Irradiation promoted exchange reactions with disulfide substituents

In the previous chapter, a new approach was described to prepare homogeneously mixed ssDNA/OEG-ATs monolayer of desired composition by IPER. Within this approach, the mixing of OEG-ATs and thiolated ssDNA occurs through exchange reaction between the OEG-AT monolayer assembled on a gold substrate and ssDNA species in solution.⁵³ This approach relies on the specific affinity of thiolated ssDNA to gold, provided by the thiol anchor group. However, thiolated ssDNA are not the only precursors for the formation of ssDNA monolayers on coinage metal substrates. Alternatively, and even more frequently, asymmetric and symmetric disulfides are used for this purpose.⁵⁴⁻⁵⁷ In this context it was important to test the possibility to perform IPER with disulfide ssDNA precursors, which should broaden significantly the application range of IPER.

Before these experiments, as a reference study, the possibility to perform IPER with a disulfide substituent was tested. As a test systems for the primary SAMs and molecular substituents, the films of non-substituted ATs on gold and symmetric dialkyldisulfides substituted with –COOH and bromoisobutyrate (BIB) groups, respectively were used. The results are compared to the well-studied reference system of the same primary matrix and –COOH substituted AT as substituent.³⁸ The effect of electron irradiation and duration of exchange reaction were monitored in detail, which gave information of both kinetics of the substitution reaction and composition of the resulting mixed films. The usefulness of the approach is demonstrated by the fabrication of complex chemical templates for the growth of polymer micro- and nanobrushes. These templates were prepared by IPER-EBL using a disulfide molecule bearing an initiator for surface initiated polymerization (SIP) as substituent.

5.1 Preparation and characterization procedures

5.1.1 Preparation of monolayers on Au

A detail description of SAMs preparation can be found in chapter 10. The used molecules are schematically shown in figure 5.1. The primary Dodecanethiol (DDT) SAMs (matrix) and single-component monolayers prepared from the 11-mercaptoundecanoic acid (MUDA), 11,11'-dithiobis-undecanoic acid (DTUDA), and 11,11'-Dithiobis[1-(2-bromo-2-methylpropionyloxy)undecane] (DTBUD) precursors (references) were formed by immersion of gold coated substrates into 1 mmol ethanolic solutions of the respective molecules at room temperature. After immersion, the samples were carefully rinsed with pure ethanol, and blown dry with argon. No evidence for impurities or oxidative degradation products was found. Note that the DTUDA and DTBUD precursors were assumed to split into two COOH-AT or two BIB-AT species, respectively, upon the adsorption, following the substrate-mediated cleavage of the disulfide bond. The

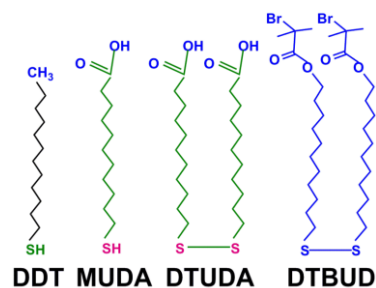


Figure 5.1 The target molecules of the present study. DDT, a nonsubstituted alkanethiol, served as the primary matrix; MUDA, DTUDA, and DTBUD were used as substituents, to fabricate the mixed SAMs and chemical templates.

same was true for the case of IPER.

5.1.2 Irradiation promoted exchange reaction and EBL

DDT SAMs were homogeneously irradiated with 10 eV electrons which are especially effective for a gentle modification of SAMs and AT SAMs, in particular.¹⁹⁵⁻¹⁹⁶ The doses were estimated by multiplication of the exposure time with the current density ($\sim 15 \mu\text{A}/\text{cm}^2$). For the fabrication of complex chemical templates, the DDT SAMs were patterned by a LEO 1530 scanning electron microscope (Zeiss, Germany) with a Raith Elphy Plus pattern generator system. A detail description of IPER and EBL can be found in chapter 10. The exchange reactions were performed by immersion of the pristine, homogeneously irradiated, or pre-patterned DDT SAMs into 1 mmol solution of MUDA, DTUDA, or DTBUD in ethanol either for a fixed (2 h) or variable time (0 - 2 h) at room temperature. After immersion, the samples were carefully rinsed with pure ethanol and blown dry with argon.

5.1.3 Fabrication of polymer brushes by SI-ATRP

A detail description of growth of polymer brushes on monolayers is given in chapter 10. Single component SAMs formed from the DTBUD precursor as well as chemical patterns formed with DTBUD as substituent were used as templates for Surface initiated polymerization (SIP). BIB tail groups of BIB-ATs served as initiators for this process. Three different polymer brushes were prepared, viz. bushes of poly(N-isopropylacrylamide) (pNIPAAM), poly(2-hydroxyethyl methacrylate) (pHEMA), and poly(ethylene glycol dimethacrylate) (pEGDMA) by Surface initiated Atom transfer radical polymerization (SI-ATRP).

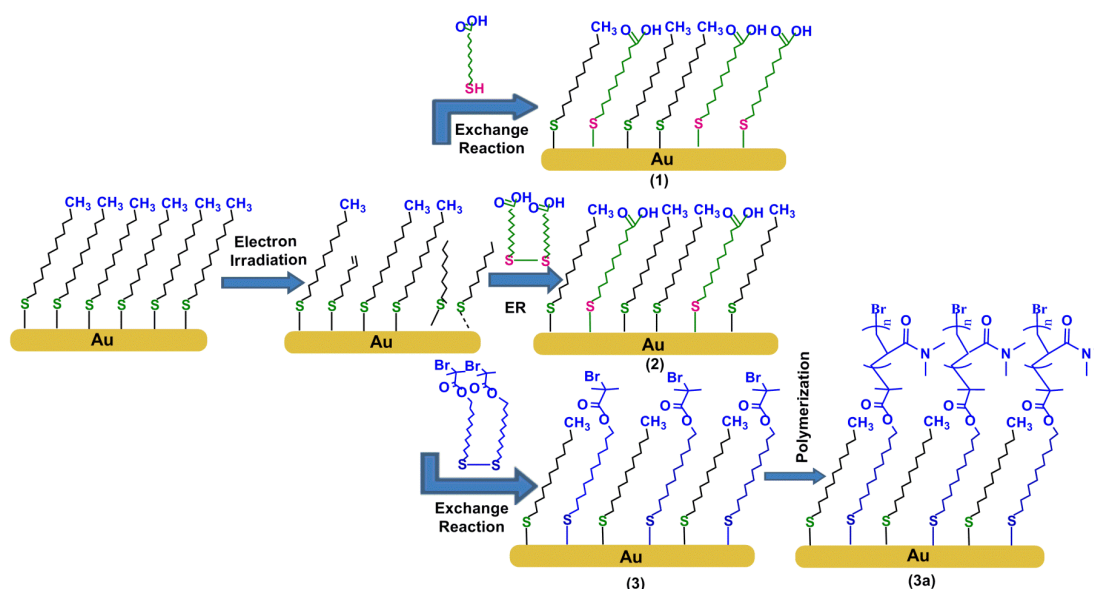


Figure 5.2 Schematic of the experimental procedure. In the first step, the primary DDT SAMs were either homogeneously irradiated by electrons or patterned by EBL. In the second step, irradiated and pre-patterned SAMs were subjected to the exchange reaction with MUDA (1) DTUDA (2), or DTBUD (3). Further, DDT/BIB-AT SAMs and chemical patterns were used as templates for SIP (3a).

5.2 Results and discussion

The general experimental procedure is schematically illustrated in Figure 5.2. In the first step, the primary DDT SAMs were either homogeneously irradiated by electrons or patterned by EBL. In the second step, irradiated and pre-patterned SAMs were subjected to the exchange reaction with DTUDA, MUDA, or DTBUD. The SAMs formed with DTUDA as substituent were used to monitor the outcome and kinetics of IPER in the case of disulfide, while the DDT/MUDA monolayers served as reference. SAMs and chemical patterns formed with DTBUD as substituent were used as templates for SIP to demonstrate the possibilities of IPER in the case of disulfide.

The homogeneous single-component and mixed films were characterized by contact angle goniometry. The kinetics of SIP was monitored by spectral ellipsometry using the polymer brushes grown on the homogeneous DDT/COOH-AT templates. The fabricated Nanostructured Brushes were characterized by atomic force microscopy (AFM).

5.2.1 Outcome and kinetics of IPER

DDT/DTUBA represents an ideal system to monitor outcome and kinetics of IPER since the monitoring can be performed by such a relatively simple and straightforward technique as contact angle (CA) goniometry. The strongly hydrophobic character of the $-\text{CH}_3$ tail groups in the DDT SAMs as well as strongly hydrophilic character of the $-\text{COOH}$ tail groups in the DTUBA monolayers result in the distinctly different values of the contact angles of water in these films. Usually, $-\text{CH}_3$ and $-\text{COOH}$ terminated aliphatic SAMs show advancing water contact angles (θ_{adv}) of $\sim 112^\circ$ and $\sim 10\text{--}15^\circ$, respectively.^{38,45,197-199} Mixed SAMs, comprised of the above constituents, exhibit some intermediate values of θ_{adv} depending on their composition. The fractions of the $-\text{CH}_3$ and $-\text{COOH}$ terminated constituents can then be derived from the contact angle data using the Cassie equation, $\cos\theta = f_1\cos\theta_1 + f_2\cos\theta_2$, where θ is the contact angle of the mixed film, f_1 and f_2 are the fractions of the components 1 and 2 in this film, and θ_1 and θ_2 are the contact angles of water for the homogeneous surfaces of these components.¹⁹⁷ The large difference between the θ_{adv} values for $-\text{CH}_3$ and $-\text{COOH}$ terminated SAMs makes the use of the Cassie equation in the given case especially favorable. Advancing water contact angles for the mixed SAMs prepared on the basis of the primary DDT/Au monolayers which were either irradiated or consecutively irradiated and exposed to the DTUDA or MUDA solution for 2 h for the exchange purpose are presented in Figure 5.3a as functions of irradiation dose. Since the promoting effect of electron irradiation could be expected up to a dose of $\sim 1 \text{ mC/cm}^2$ in the case of 10 eV electrons,^{38,45} the dose range up to a slightly higher value (1.5 mC/cm^2) was selected. IPER with MUDA served as direct reference to the case of DTUDA since the only difference between these two systems is their thiol or disulfide character. The contact angles for the single-component monolayers formed from DDT, DTUDA and MUDA serving as references to the respective mixed SAMs were estimated at 110° , 35° and 20° respectively. These values are close to the expected ones. The difference between the θ_{adv} values for the SAMs formed from DTUDA and MUDA is not that large and can be tentatively explained by the sensitivity of the preparation procedure in the case of $-\text{COOH}$ termination of the precursor to its subtle parameters.²⁰⁰

In the case of irradiation only, θ_{adv} decreased continuously with increasing dose following a partial damage of the terminal $-\text{CH}_3$ groups at the SAM-ambient interface and appearance of further defects in the monolayer.^{128,201} Both this behavior and absolute values of the observed changes agree well with previous observations for non-substituted AT SAMs on Au.^{38,45,202-203} However, a much larger change of θ_{adv} was achieved by the combination of irradiation and subsequent exchange reaction both in the case of MUDA (as reported)^{38,45} and most importantly in the case of DTUBA, which suggests that IPER with a disulfide substituent is possible. Indeed, the behavior observed in Figure 5.3a can only be explained by extensive replacement of the DDT species in the primary SAMs by the MUDA or DTUBA molecules, continuously promoted by the irradiation, which results in the formation of a mixed SAM with a heterogeneous $-\text{CH}_3/-\text{COOH}$ surface. The small extent of the exchange reaction for the pristine DDT SAMs (i.e. without irradiation) indicates a high quality and a dense molecular packing of these films.²⁰

The higher θ_{adv} values for DTUBA as compared to MUDA mean that the extent of the exchange is smaller in the former case, resulting in a smaller fraction of the $-\text{COOH}$ terminated ATs in the mixed SAMs. This behavior is understandable since the imbedding of the larger DTUBA species, having probably a complex conformation, into the defective DDT matrix is certainly more difficult than the analogous process for the MUDA moieties. Using the Cassie equation, relative contents of the $-\text{COOH}$ terminated ATs in the mixed films prepared with DTUBA or MUDA as substituents were calculated. According to these curves, which are presented in Figure 5.3b, this content in the case of DTUBA is smaller than that in the case of MUDA at all doses. Both curves exhibit a levelling off behavior at a dose 1-1.5 mC/cm^2 , with ultimate values of $\sim 59\%$ and $\sim 75\%$ in the case of DTUBA and MUDA, respectively. Even though the former value is lower than the latter one, it is still high enough to provide a broad dynamical range both for the fabrication of mixed SAMs and chemical lithography on the basis of IPER with a disulfide as substituent. The above experiments regarding the outcome of IPER were complemented by the measurements of the kinetics of this process. To this end, primary DDT SAMs were irradiated with a fixed dose of 1 mC/cm^2 and subjected to IPER with either DTUBA or MUDA (reference) as substituents for a variable time. The values of θ_{adv} for the resulting mixed SAMs are presented in Figure 5.4a as functions of the exchange time, while the respective relative contents of the $-\text{COOH}$ terminated ATs in the in the mixed films prepared with DTUBA or MUDA as substituents, calculated using the Cassie equation, are shown in

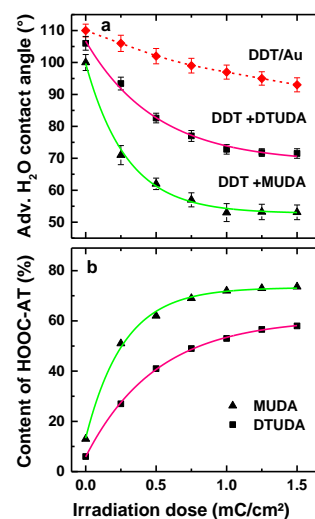


Figure 5.3 (a) Advancing contact angles of water for the mixed DDT/COOH-AT SAMs prepared on the basis of the primary DDT/Au monolayers which were either irradiated (diamonds) or consecutively irradiated and exposed to the DTUBA (squares) or MUDA (triangles) solution for 2 h for the exchange purpose. (b) Relative contents of the $-\text{COOH}$ terminated ATs in the mixed films prepared with DTUBA (squares) or MUDA (triangles) as substituents. The contents were calculated from the contact angle data in panel a using the Cassie equation. Both advancing contact angles in panel a and the relative contents in panel b are presented as functions of irradiation dose. The solid lines in panels a and b are exponential fits to the experimental data. The curve for DDT/Au in panel a is just a guide for the eyes.

Figure 5.4b. The curves in Figure 5.4b can be fitted well by first order exponential functions, $f = f_{\infty} [1 - \exp(-kt)]$, where, f and f_{∞} are the current and saturation values of the COOH-AT content, respectively. This behaviour suggests a pseudo first order kinetics for the exchange reaction for both DTUDA and MUDA. The reaction rates for both substituents are similar; viz. $6.1 \times 10^{-4} \text{ s}^{-1}$ for DTUDA and $6.6 \times 10^{-4} \text{ s}^{-1}$ for MUDA. At the same time, the saturation value for the COOH-AT content for the case of DTUDA is noticeably lower than that for MUDA, as can be expected in view of the size and conformation differences. Note that two COOH-AT moieties in the mixed films prepared with DTUDA as substituent correspond to only one exchanged DTUDA molecule which splits into two –COOH substituted ATs upon the adsorption. Note also that the saturation values for the COOH-AT content are almost achieved at a reaction time of 2 h for both DTUDA and MUDA cases, which was the reason for selecting this time for the experiments related to the outcome of IPER (Figures 5.3a and 5.3b).

The exchange reaction occurs stochastically but is driven thermodynamically. As to the kinetics of this reaction, it should be presumably the second order process, since the reaction involves two participants, viz. the substituents in the solution and the irradiation-induced defects in the matrix SAM. The fact is that, the first-order kinetics was observed with respect to the irradiation dose suggests, as can be expected, that one of the reactants, viz. substituents in the solution, is present in large excess as compared to the other. The difference between the thiols and disulfides is then presumably the exact character of the irradiation-induced defects and related probability of the molecular reorganization necessary for the imbedding of the disulfide moiety into the primary matrix. Respectively, the amount of the irradiation-induced defects which promote the exchange reaction in the case of disulfide substituents is smaller than that in the case of thiols. This is exactly what was found in the experiments. Whereas the rate-constants are similar in both cases, the extents of the reaction under the saturation conditions are different (Figure 5.4b) assuming the different amounts of the crucial reactant, i.e. irradiation-induced defects promoting the exchange reaction.

5.2.2 IPER with a disulfide bearing an initiator for SIP

The results presented in Section 5.2.1, suggest that IPER with a disulfide as substituent is possible. Along with this principal result, the feasibility and usefulness of the approach, applying it to the fabrication of protein brush patterns was demonstrated. To this end, a disulfide molecule bearing an initiator for SIP as substituent was selected, viz. DTBUD (Figure 5.1). Note that the molecules bearing such an initiator - BIB group - are frequently used for

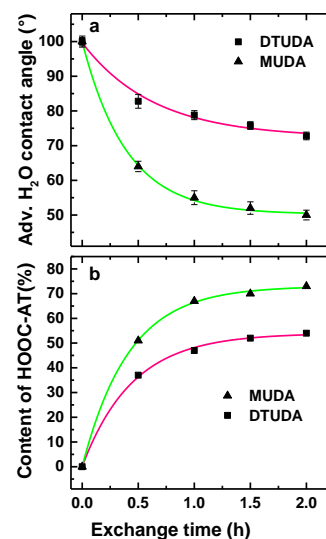


Figure 5.4 (a) Advancing contact angles of water for the mixed DDT/COOH-AT SAMs prepared on the basis of the primary DDT/Au monolayers which were consecutively irradiated (1 mC/cm^2) and exposed to the DTUDA (squares) or MUDA (triangles) solution for the exchange purpose as functions of the exposure time. (b) Relative contents of the -COOH terminated ATs in the mixed films prepared with DTUDA or MUDA as substituents as functions of the exposure time. The contents were calculated from the contact angle data in panel a using the Cassie equation. The solid lines in panels a and b are exponential fits to the experimental data.

SIP,^{134,138,141,204-210} both as thiols^{138,204,206,208-209} and disulfides.^{141,205,207} In most cases, these molecules were custom-synthesized but, since recently, they are also available commercially in the form of disulfides. Such a disulfide was used in the experiments.

Advancing contact angles of water for the mixed DDT/BIB-AT SAMs prepared on the basis of the primary DDT/Au monolayers which were either irradiated (diamonds) or consecutively irradiated and exposed to the DTBUD (circles) solution for 2 h for the exchange purpose are presented in Figure 5.5a as functions of irradiation dose. Relative content of the BIB terminated moieties in the mixed films prepared with DTBUD as substituent is presented in Figure 5.5b as a function of irradiation dose. These values were calculated from the contact angle data in panel a using the Cassie equation. Note that the advanced contact angle of water for the single component SAM prepared from the DTBUD precursor was estimated at 65°. The difference to the analogous value for DDT/Au (110°) is not that large as in the case of MUDA, resulting in a lower accuracy of the relative content values in Figure 5.5b. In addition, due to the bulk character of the BIB tail group, the respective DDT/BIB-AT mixed SAMs will be quite rough on the molecular scale, which can affect the θ_{adv} values to some extent. Therefore, the relative content of the BIB-ATs presented in Figure 5.5b can be considered as a coarse estimate only. According to the figure, this content can be varied continuously from 10 to 72% by a dose variation from 0 to 1 mC/cm². Significantly, the saturation behaviour is not observed yet at 1 mC/cm², which means that even higher contents of the BIB-ATs are possible at higher doses.

The above experiments on the outcome of IPER were complemented by the measurements of the kinetics of this process, similar to the case of DTUDA (Figure 5.4). To this end, the primary DDT SAMs were irradiated with a fixed dose of 1 mC/cm² and subjected to IPER with DTBUD as substituent for a variable time. The values of θ_{adv} for the resulting mixed SAMs are presented in Figure 5.6a as a function of the exchange time, while the respective relative content of BIB-ATs in the mixed SAMs are presented in Figure 5.6b. The content values were calculated using the Cassie equation. The curve in Figure 5.6b can be fitted well by the same first order exponential function as in the case of DTUDA or MUDA (see previous section), suggesting a first order kinetics for the exchange reaction of DTBUD. The reaction rate was estimated at $9.4 \times 10^{-4} \text{ s}^{-1}$ which is even faster than in the case of DTUDA. Accordingly, the saturation value for the content of BIB-ATs in the mixed SAMs is almost achieved at a reaction time of 1 h, so that 2h selected by us for the experiments related to the outcome of IPER (Figure 5.5) were a reasonable choice. The content at saturation (~70%) is somewhat higher than that in the case DTUDA (59%, see previous section), which can

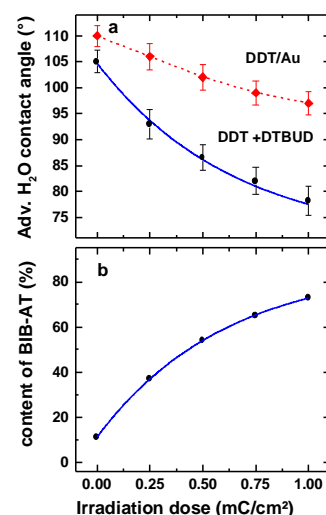


Figure 5.5 (a) Advancing contact angles of water for the mixed DDT/BIB-AT SAMs prepared on the basis of the primary DDT/Au monolayers which were either irradiated (diamonds) or consecutively irradiated and exposed to the DTBUD (circles) solution for 2 h for the exchange purpose. (b) Relative content of the BIB terminated ATs in the mixed films prepared with DTBUD as substituent. The contents were calculated from the contact angle data in panel a using the Cassie equation. Both advancing contact angles in panel a and the relative contents in panel b are presented as functions of irradiation dose. The solid lines in panels a and b are exponential fits to the experimental data. The curve for DDT/Au in panel a is just a guide for the eyes.

be tentatively explained by the dependence of the outcome and kinetics of IPER on the exact molecular composition of the substituent. In addition, the value for DTBUD can be somewhat overestimated because of the limited accuracy of the evaluation procedure in the given case.

Previous two sections demonstrate clearly the possibility of IPER with disulfides as substituents. It is generally assumed that disulfides do not dissociate spontaneously in solution but only upon the direct interaction with the substrate, which results in the cleavage of the disulfide bond and adsorption of both chain parts as thiolates.^{20,211} The respective process can occur easily in the case of the SAM formation, when the substrate can be freely accessed by the disulfide moieties. However, such a direct access is not possible in the case of IPER, in which the substrate can only be accessed by the molecular exchange. The major hindrance is then the larger size of the disulfide moiety as compared to the constituents of the primary, matrix SAM. This means that the exchange reaction should involve the expelling of at least two of these constituents. One possibility then is the molecular domains of several damaged SAM constituents which can be simultaneously exchanged for a larger species. However, assuming the low irradiation doses used in the IPER experiments, one would rather expect the damage of the individual molecules which will then be stochastically distributed in the pristine matrix,³⁸ even though the formation of small amount of two-adjacent-molecules defects cannot be completely excluded. In addition, IPER has also been performed with the thiolated single-stranded DNA species as substituents.⁵³ The diameter of these species is by a factor of 7-8 larger than the area taken by a constituent of the matrix SAM, and it is not realistic to assume that the clusters of 7-8 damaged molecules can be formed by irradiation. Thus, it will be more obvious to assume that the damaged molecules in the matrix SAM serve as initiator sites for the exchange reaction which probably involves partial squeezing or expelling of the neighbouring species.

5.2.3 SIP on IPER-generated chemicals templates

The data presented in the previous section suggest that a high fraction of the BIB terminated ATs can be incorporated into the DDT matrix by IPER with DTBUD as substituent. This process can be performed not only homogeneously but also in a lithographic way - by the combination of IPER with EBL. This should enable the preparation of complex chemical patterns which can serve as templates for the growth of polymer brushes by SIP starting from the initiator groups of the imbedded BIB-AT species. The main advantage of IPER-EBL as

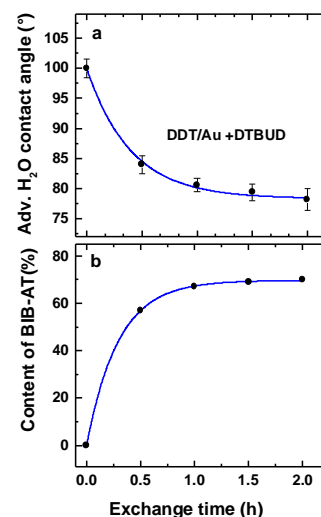


Figure 5.6 (a) Advancing contact angle of water for the mixed DDT/BIB-AT SAMs prepared on the basis of the primary DDT/Au monolayers which were consecutively irradiated (1 mC/cm^2) and exposed to the DTBUD (circles) solution for the exchange purpose as a function of the exposure time. (b) Relative content of the BIB terminated ATs in the mixed films prepared with DTBUD as substituent as a function of the exposure time. The contents were calculated from the contact angle data in panel a using the Cassie equation. The solid lines in panels a and b are exponential fits to the experimental data.

compared to other methods used for the preparation of polymer brush patterns^{204,206-208} is the possibility to tune precisely the density of the initiator groups over the template.^{49,53-55} This can be easily achieved by the selection of a proper irradiation dose which defines the local fraction of the BIB-AT species imbedded into the DDT matrix.

As test polymers for SIP, pNIPAAm, pHEMA, and pEGDMA were used. pNIPAAm has significant potential in technology and biomedical applications.²⁰⁷ Because of the variety of useful properties, it is probably one of the most frequently used polymers for SIP and in this regard, a suitable reference system.^{204,206-208} pHEMA has also good potential for biomedical applications; an additional advantage of this polymer is the possibility of its functionalization with a variety of chemical species.¹⁴¹ Similarly, pEGDMA is also of interest in biological and biomedical context; its special feature, useful for some applications, is a high degree of cross-linking.

Before performing lithographic experiments, the formation of homogeneous polymer brushes on the single components BIB-AT monolayers formed upon the adsorption of DTBUD on gold were tested. The respective data are presented in Figure 5.7 where the ellipsometric thicknesses of the pNIPAAm, pHEMA, and pEGDMA brushes are depicted as functions of the reaction time. Both the kinetics of the brush formation and the ultimate thickness values agree well with the literature data. In particular, the curves for pNIPAAm and pHEMA can be fit well by exponential functions suggesting, in agreement with literature data,^{141,207} a pseudo first order kinetics for the surface-initiated atom-transfer radical polymerization in both cases; the derived values of the rate constant are 0.58 and 0.48 h⁻¹, respectively. The maximal thickness of the pNIPAAm brush (~430 nm) is higher than the reported values of 200-300 nm,^{206-207,212} while that of the pHEMA brush (~210 nm) is similar to the values reported for the given reaction time.¹⁴¹ The experimental points for the pEGDMA brush can be fit well by a linear function, also in accordance with literature data.²⁰⁵ The growth of this brush occurred much slowly as compared to the pNIPAAm and pHEMA cases, which agrees with the literature data as well.²⁰⁵ The only difference was slightly lower (by ~25%) values of the brush thickness, which was presumably related to subtle differences of the preparation procedures.

The above kinetic data were obtained after the optimization of the preparation procedures under the specific conditions of our laboratory. An important information from these experiments was the necessary duration of SIP for each of the selected polymers. This parameter was set to 7, 3, and 40 h for the preparation of pNIPAAm, pHEMA, and pEGDMA brush patterns, respectively. AFM images of representative pNIPAAm, pHEMA, and pEGDMA brush patterns grown by SIP on the DDT/BIB-AT templates prepared by IPER-EBL with DTBUD

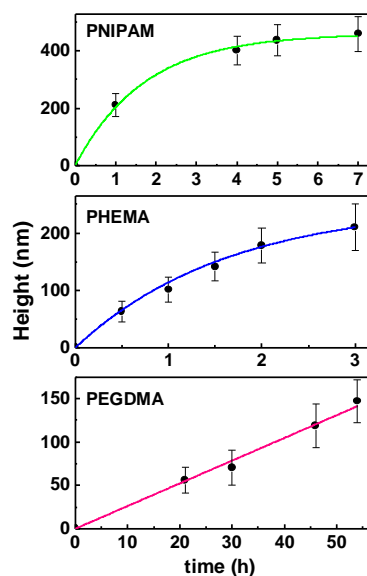


Figure 5.7 Ellipsometric thicknesses of the homogeneous pNIPAAm, pHEMA, and pEGDMA brushes as functions of the reaction time. The brushes were grown on the homogeneous BIB-AT templates by SIP. The solid lines in the top and middle panels are exponential fits to the experimental data. The solid line in the bottom panel is a linear fit to the experimental data.

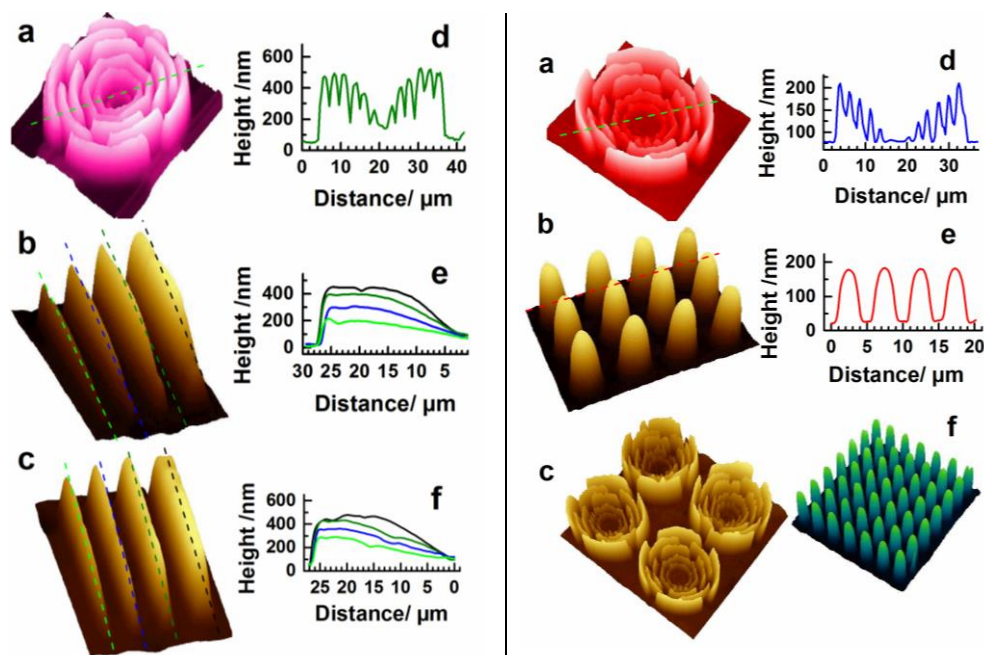


Figure 5.8 AFM images (3D view) of representative pNIPAAm brush patterns grown by SIP (7 h) on the DDT/BIB-AT templates prepared by IPER-EBL with DTBUD as substituent as well as height profiles along the lines of the respective colour shown in the images. (a) a nanorose; (b,c) wedges with widths of 2, 1, 0.5, and 0.25 μm ; the dose along the wedges was varied from 0 to 1 mC/cm^2 (b) and from 0 to 3 mC/cm^2 (c). The lateral size of the images in panels a, b, and c can be derived from the respective height profiles in panels d, e, and f, respectively. The 3D structures in all patterns were intentionally sculptured by the gradient-like templates.

Figure 5.9 AFM images (3D view) of representative pHEMA brush patterns grown by SIP (3 h) on the DDT/BIB-AT templates prepared by IPER-EBL with DTBUD as substituent as well as height profiles along the lines shown in the images. (a,c) nanoroses; (b,f) cone columns. The lateral size of the images in panels a and b can be derived from the respective height profiles in panels d and e, respectively. The size of the images in panels c and f is 69×65 and 35×33 μm^2 , respectively. The 3D structures in all patterns were intentionally sculptured by the gradient-like templates.

as substituent are presented in Figures 5.8, 5.9, and 5.10, respectively, along with the height profiles along the lines of the respective colour shown in the images. All the patterns were initially prewritten by EBL in the primary DDT templates and then “developed” by the exchange reaction with DTBUD. Upon the development step, each local dose was transformed in the respective density of the BIB-AT moieties. This density, in its turn, was transformed in the local height of the polymer brush, resulting in formation of complex gradient-like pattern as shown in Figures 5.8-5.10. The gradient character is especially obvious in the wedge patterns in Figures 5.8b and 5.8c where a continuous increase of the brush height with increasing dose is observed. As known from the previous SIP experiments,^{39,44,53,194} a higher grafting density leads to a higher polymer brush because of the straightening of the polymer chains within the feature. The maximum heights of the brush patterns agree well with the values from the kinetic experiments (Figure 5.7) in the case of pNIPAAm and pHEMA (Figures 5.8 and 5.9). The situation is, however, different in the case of pEGDMA. The maximum height of the brush pattern in Figure 5.10 (~ 20 nm) is much smaller than the height of the homogeneous brush for the same duration of SIP (~ 100 nm). So it was also assumed that, in view of the very rough background of the pEGDMA brush pattern (Figure 10a), that the growth of this brush occurred not only on the areas containing the BIB moieties but also on the areas comprised of DDT only ($-\text{CH}_3$ termination). The reason for such a limited selectivity is unclear;

the fabrication of well-defined pEGDMA brush patterns might require a further optimization or even significant modification of the SIP procedure in this particular case.

As for the pNIPAAm and pHEMA brush patterns, they exhibit height saturation at high irradiation doses, which is especially obvious in the wedge patterns in Figures 5.8b and 5.8c. This effect can be monitored in detail looking at the respective height profiles in Figures 5.8e and 5.8f and explained by the onset of irradiation-induced cross-linking.^{38,45} Such a cross-linking, appearing at irradiation doses above 1-1.5 mC/cm² for 10 eV electrons, hinders IPER, which is the reason for the saturation of this process at higher doses as shown in Figures 5.3b

and 5.5b. In the wedges presented in Figure 5.8b, which were written with a dose variation from 0 to 1 mC/cm², the saturation occurs at a $\sim 2/3$ of the wedge length (Figure 5.8e) corresponding to a dose of $\sim 0.5-0.7$ mC/cm². In the case of the wedges in Figure 5.8c, which were written with a dose variation from 0 to 3 mC/cm², the saturation takes place at an even lower dose (Figure 5.8f). The difference to the value of 1-1.5 mC/cm² for 10 eV electrons is related to the higher efficiency of the 1 keV electrons used for EBL (a factor of 2-2.5).¹⁹⁴

Another prominent effect observed in the wedge patterns is a decrease in the maximum height of the wedge stripes with decreasing width. Such a behavior has been observed previously for polymer brushes on different templates and was explained by the widening of the fabricated features due to the spreading of the side chains.^{43,194,213} This imposes some limitations on the lateral size of these features. Nevertheless, extended sub-micrometer and nanometer-scale structures of sufficient height can be prepared even within these limitations.

5.3 Conclusions

Using a model system of a non-substituted alkanethiolate SAM on gold as primary matrix and -COOH substituted dialkyldisulfide as substituent, it was demonstrated that IPER can be performed with disulfide substituents in the same manner as in the case of thiols. The kinetics of the exchange reaction was found to be similar in both cases but the extent of this reaction, i.e. the ultimate portion of the substituent moieties in the resulting mixed SAMs, occurred to be smaller for disulfides. The feasibility and practical usefulness of the approach were demonstrated by the experiments with another disulfide substituent - a molecule bearing the BIB tail group which can serve as an initiator for SIP. Using this substituent and combining IPER with EBL, a variety of complex polymer brush patterns were prepared by SIP.

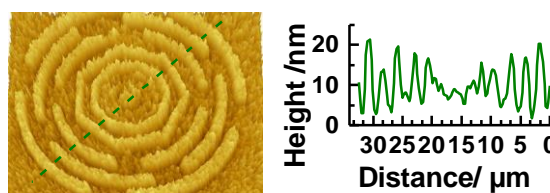


Figure 5.10 a) AFM image (3D view) of a representative pEGDMA brush pattern grown by SIP (40 h) on the DDT/BIB-AT template prepared by IPER-EBL with DTBUD as substituent as well as b) a height profile along the line in the image. The lateral size of the image can be derived from the height profile. The 3D structure in the pattern was intentionally sculptured by the gradient-like template.

6. Fabrication of ssDNA/oligo(ethylene glycol) monolayers by promoted exchange reaction with disulfide substituents

In the previous chapter, It was described that disulfides are suitable for IPER, even though less efficient than thiols, by the experiments with COOH-substituted dialkyl disulfide serving as substituents for non-substituted AT SAM.⁸⁷

In this context, the experimental results on the fabrication of ssDNA/OEG-AT monolayers from the ssDNA-based disulfide precursors, serving as substituents for the OEG-AT matrix exposed to electrons within the framework of the IPER approach is presented here. As a test ssDNA moiety a well-defined adenine-based homo-oligonucleotide (25-mer), arranging it as a thiolate (reference),⁵³ asymmetric disulfide, and symmetric disulfide were chosen. Along with the application of the above precursors in the framework of the IPER approach, a comparative characterization of the ssDNA monolayers fabricated on their basis within the standard immersion procedure was performed.²⁰ On one hand, these monolayers served as references for the ssDNA/OEG-AT films prepared by IPER. On the other hand, they are of interest on their own, providing information on the efficiency of a particular precursor.

6.1 Preparation and characterization procedures

6.1.1 Preparation of disulfide DNA films on Au

The ssDNA monolayers were prepared in accordance with literature protocols.^{12,13} as The used molecules are schematically shown in Figure 6.1. Briefly, Au substrates were immersed in 3 μ M solution of A25SH, A25SSOH, or A25SSA25 in 1 M CaCl₂-TE buffer (1 M CaCl₂, 10 mM Tris-HCl, 1 mM EDTA, pH 7.0) for 40 h at a temperature of 37°C. Afterward, the samples were rinsed with Millipore-grade water, sonicated with water for 60 s followed by rinsing with water for 0.5 min to remove loosely bound A25SH species. Finally, the samples were blown dry with Ar.⁷⁸

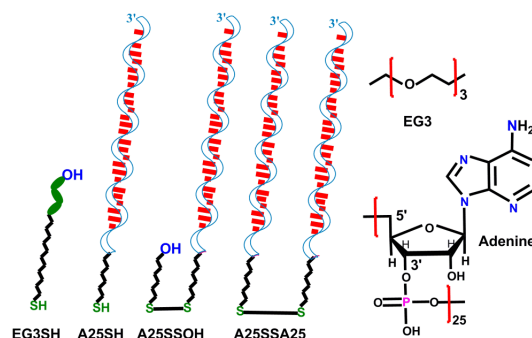


Figure 6.1. The precursor molecules of the present study, along with their abbreviations and schematic representation of the repeating units

6.1.2 IPER with symmetric and asymmetric disulfides DNA precursors

As first step of the IPER procedure, the primary EG3S films were homogeneously irradiated with 10 eV electrons provided by a flood gun. The doses were estimated by multiplication of the exposure time with the current density ($\sim 15 \mu\text{A}/\text{cm}^2$). The electron gun was mounted at a distance of ~ 15 cm from the sample to ensure uniform illumination. Subsequent exchange reactions were carried out by immersion of the irradiated EG3S films in

a 3 μM solution of A25SH, A25SSOH, or A25SSA25 in 1 M CaCl_2 -TE buffer for 3 h at a temperature of 37°C. After immersion, the samples were carefully rinsed with Millipore-grade water, sonicated for 60 s followed by rinsing with water for 60 s to remove loosely bound species. Finally, they were blown dry in an argon stream. Note that the duration of the exchange reaction was optimized for A25SH⁵³ and kept the same for A25SSOH and A25SSA25 to make possible direct comparison.

6.2 Results and Discussion

The general experimental procedure is schematically illustrated in Figure 6.2. A25S and EG3S/A25S monolayers were characterized by laboratory and synchrotron-based X-ray photoelectron spectroscopy (XPS) and angle-resolved near-edge X-ray absorption fine structure (NEXAFS) spectroscopy. Laboratory XPS was used to determine the packing density of the A25S monolayers and to monitor outcomes of the IPER procedure in the case of the EG3S/A25S films.

6.2.1 A25S films

The packing densities of the A25SH monolayers prepared at the identical conditions from the thiolated and disulfide precursors differ significantly. The respective values are presented in Figure 6.3, corresponding to molecular areas of ~ 190 , ~ 150 , and ~ 120 \AA^2 for the A25SSA25, A25SH, and A25SSOH precursors, respectively. The densities⁵⁸ were obtained following the approach described in ref 58 and, in each case, represent an average over several samples prepared within different measurement series. The values are reasonable and well comparable to the previous results, being among the highest packing densities reported^{60,71} so far for ssDNA monolayers on gold.^{53,58}

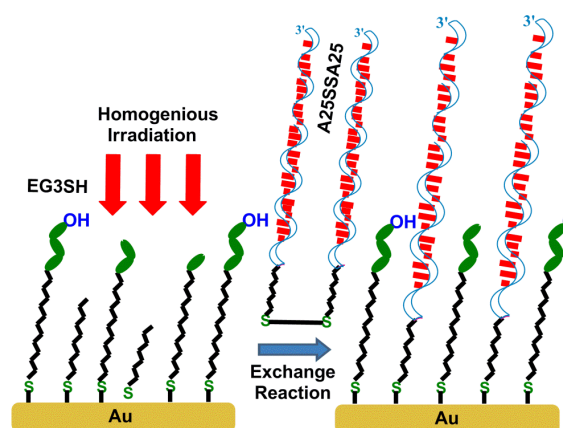


Figure 6.2 Schematic of the experimental procedure. In the first step, the primary EG3S SAM was homogeneously irradiated by electrons. In the second step, irradiated SAM was subjected to the exchange reaction with A25SSA25. The approach is also analogous for A25SSOH and A25SH (reference).

The lowest packing density was observed for the symmetric disulfide precursor, which is well understandable in view of the sterical hindrance associated with the presence of two bulky chain parts stochastically orientated with respect to one another. It is then difficult to achieve a direct contact of the disulfide moiety with the substrate upon adsorption, which is a prerequisite for the cleavage of the disulfide bond with the subsequent release of two A25S species bound to the substrate over the thiolated anchors. Otherwise, the binding to the substrate will be weak and A25SSA25 will desorb. The above restrictions exist from the very beginning of the assembly process, becoming even more severe in its course, since the assembled A25S species will provide additional hindrance for the bulky A25SSA25 species to make a proper contact with the substrate.

Surprisingly, the highest packing density is not observed for the thiol (A25SH) but for asymmetric disulfide (A25SSOH) precursor. Obviously, the comparably small MH moieties do not represent any additional sterical hindrance for the proper assembly of the A25S species on the substrate starting from the A25SSOH precursor. It is, however, difficult to say why the asymmetric disulfide is even more efficient than thiol in the given case. The MH moieties adsorbed along with the A25S species after the cleavage of the disulfide bonds do not take much space in view of their comparably small cross section ($\sim 21.4 \text{ \AA}^2$). Probably, these species assist the adsorption of the subsequent A25SSOH moieties, resulting in a denser molecular packing as compared to the A25SH case. Alternatively, the presence of the coadsorbed MH moieties can prevent the direct contact of the adenine bases of the A25S species with the substrate, which can result in an increase of the molecular area. It is well known that adenine has a particular affinity to gold,^{55,214} which is of course weaker than the thiolate bond, but probably strong enough to promote an additional anchor point over the direct base-substrate bond.

In spite of the differences in the packing density, the A25S films prepared from the different precursors are identical in terms of the chemical composition, apart from the presence of the comparably small MH moieties in the A25SSOH derived films. Indeed the characteristic XP and NEXAFS spectra of the A25SH, A25SSOH, and A25SSA25 derived A25S monolayers in Figures 6.4 and 6.5 are almost identical, apart from some intensity differences related mostly to the slight deviations in the positioning of the individual samples during the measurements at the synchrotron radiation facility. The packing density differences between the A25SSOH and A25SH derived monolayers are hardly seen in the spectra, because of the saturation

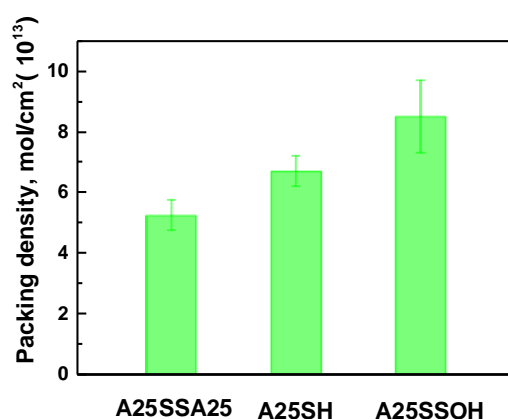


Figure 6.3 Packing density of the A25S monolayers prepared from the A25SSA25, A25SH, and A25SSOH precursors.

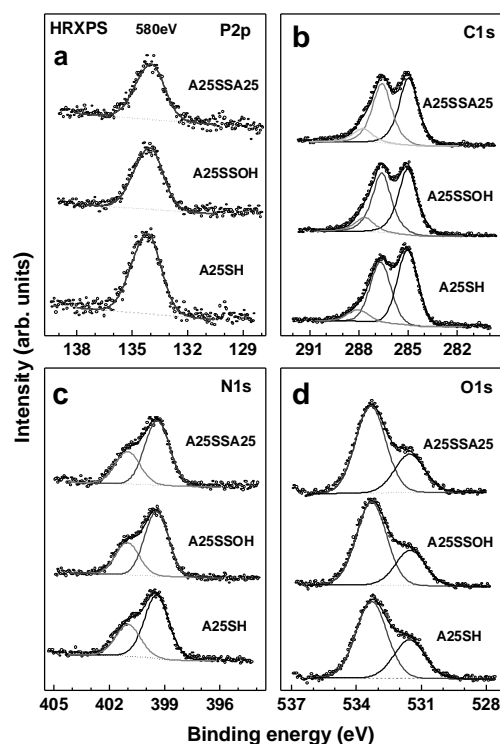


Figure 6.4 P 2p (a), C 1s (b), N 1s (c), and O 1s (d) XP spectra of the A25S monolayers prepared from the A25SSA25, A25SH, and A25SSOH precursors; the spectra are marked respectively. The C 1s, N 1s and O 1s spectra are decomposed into individual emissions (solid gray lines).

of the photoemission (XPS) and PEY (NEXAFS) signals from these relatively thick films.^{193,215} The lower packing density of the A25SSA25 derived films is exhibited in some of the spectra as lower intensity of the characteristic features.

A detailed description and assignments of the individual emissions in the XP spectra and absorption resonances in the NEXAFS spectra of the A25S monolayers can be found elsewhere.^{53,55-56,58,79,216-218} It is noted that the spectra in Figures 6.4 and 6.5 exhibits all expected characteristic emissions and resonances of adenine-based homoligonucleotides, with no additional features observed. In particular, the P 2p and O 1s XP spectra (Figures 6.4a and 6.4d) as well as O K edge NEXAFS spectra (Figure 6.5b) are exclusively representative of the A25 backbone since the adenine nucleobase does not contain oxygen and phosphorus (Figure 6.1). The N 1s XP spectra (Figure 6.4c) and N K-edge NEXAFS spectra (Figure 6.5c) are exclusively representative of adenine, exhibiting the characteristic emissions at binding energies of ~ 399.5 and ~ 401.2 eV (with a larger spectral weight for the former peak) and π^* -like adsorption resonances at photon energies of ~ 399.4 eV (1) and ~ 401.3 eV (2).^{56,192} The C 1s XP spectra (Figure 6.4a) and C K-edge NEXAFS spectra (Figure 6.5a) are representative of both the adenine nucleobase and A25 backbone. The intensity relations between the individual emissions or resonances within a particular XP or NEXAFS spectrum are typical of adenine based homoligonucleotides. This underlines a high quality and contamination-free character of the fabricated A25S monolayers.

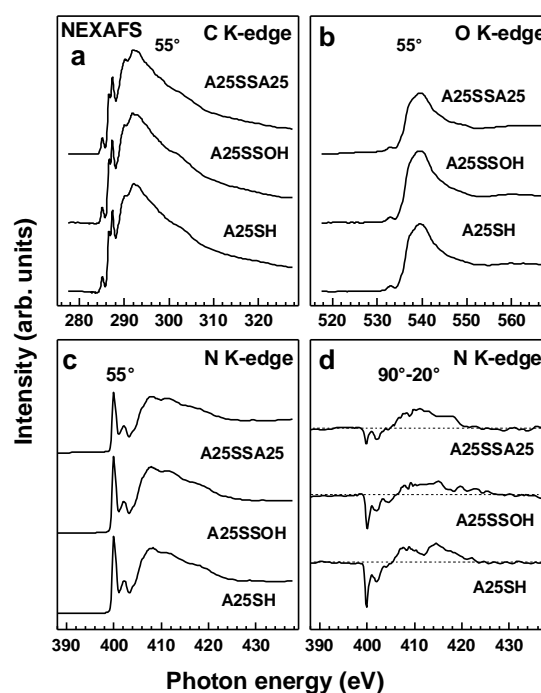


Figure 6.5 C (a), N (b), and O (c) K-edge NEXAFS spectra of the A25S monolayers prepared from the A25SSA25, A25SH, and A25SSOH precursors; the spectra are marked respectively. The spectra were acquired at an X-ray incidence angle of 55°. (b) Difference between the N K-edge spectra collected at normal (90°) and grazing (20°) angles of X-ray incidence for the above samples. The characteristic absorption resonances and the respective difference peaks are marked by numbers. The vertical scale of panel (d) is scaled up by a factor of 3.5 as compared to that of panel (c).

Based on the linear dichroism effects in X-ray absorption (chapter 10), the orientational order in the A25S monolayers were studied. A convenient way to get a qualitative impression of these effects is drawing of so called difference spectra, viz. the difference between the spectra acquired at normal (90°) and grazing (20°) incidence of X-rays. Such spectra are presented in Figure 6.5d for the N K-edge. These spectra exhibit pronounced peaks at the positions of the absorption resonances 1 and 2, which suggests a certain orientational order in the A25S monolayers. Since the resonances 1 and 2 have the π^* character and their transition dipole moments (TDMs) are orientated perpendicular to the

nucleobases and, consequently, parallel to the A25 strands, the negative sign of the difference peaks implies that the strands are predominantly oriented upright to the substrate surface. The extent of this orientation is however limited since the amplitude of the difference peaks is small as compared to the intensity of the respective resonances in the 55° spectra (consider the difference in the vertical scales in Figures 6.5c and 6.5d). The respective intensity modulation amplitude,^{54,56} i.e. the change of the normalized intensity of the resonances 1 and 2 at going from grazing to normal incidence is in a range of 0.82-0.84 for all A25S monolayers, with the larger value corresponding to the case of the A25SSA25 precursor. Also the average tilt angle of the A25 strands in the A25S monolayers, determined within the standard formalism,¹⁴⁸ modified slightly for the case of ssDNA monolayers,^{54,56,216} is about 32-33°, with the larger value corresponding to the A25SSA25 case. Thus, the orientational order is slightly better in the A25S monolayers prepared from the A25SH and A25SSOH precursors as compared to the film fabricated from the A25SSA25 compound, which correlates to some extent with their packing densities (see above). Note, however, that the degree of the orientational order is rather low in all studied films, which is typical of this kind of systems, including the values of the intensity modulation amplitude and average tilt angle.^{54,216} There is presumably a certain distribution of different orientations for the individual strands, including irregular bends in the backbone, along with rotation of individual nucleobases relative to the backbone, occurring to some extent as well.

6.2.2 Outcome of IPER

The above A25S films served as references to determine the compositions of the mixed EG3S/A25S monolayers prepared by IPER with the A25SH, A25SSOH, or A25SSA25 substituents. This composition was monitored using the N 1s and P 2p XP spectra, following the established procedure.⁵³ These spectra are shown in Figures 6.6 and 6.7 for the A25SSOH and A25SSA25 case, respectively; the analogous data for the A25SH substituent can be found elsewhere.⁵³ As seen in the figures 6.6 and 6.7, the spectra of the EG3S films subjected to IPER with either A25SSOH or A25SSA25 substituents exhibit the characteristic emissions of the adenine-based homooligonucleotides (Figure 6.4), which means that IPER occurs with ssDNA-substituted disulfides in a similar way as with the thiols. As mentioned above, the disulfide bond is cleaved upon the adsorption, resulting in either A25S and MH species (A25SSOH) or two

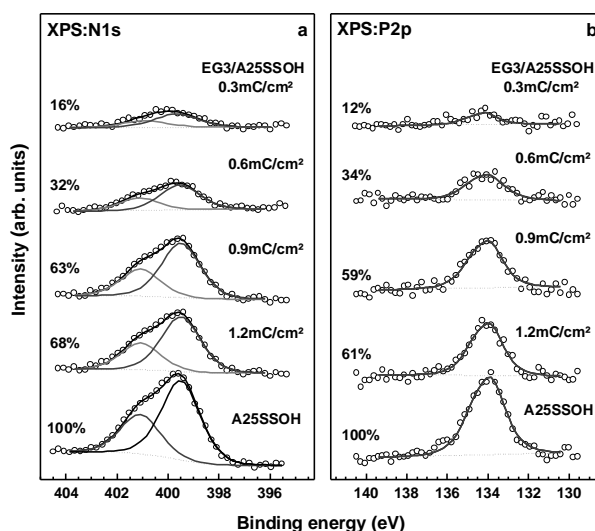


Figure 6.6 N 1s (a) and P 2p (b) XP spectra of the EG3S/A25S monolayers prepared by IPER with A25SSOH as substituent. The spectra of the A25S film prepared from the same precursor are given at the bottom of each panel as references. The irradiation doses (IPER) and portions of the A25S species in the films, normalized to the value for the A25S monolayer (100%), are given at the respective spectra.

A25S moieties mixed with the residual EG3S molecules. Significantly, the exchange reaction does not occur without irradiation, which has been previously demonstrated for ssDNA-substituted thiols⁵³ and shown now for the A25SSA25 case (top curves in Figure 6.7). This has important implications for IPER based lithography, assuring the absence of the ssDNA species beyond predefined spots treated with electron beam.^{53,216}

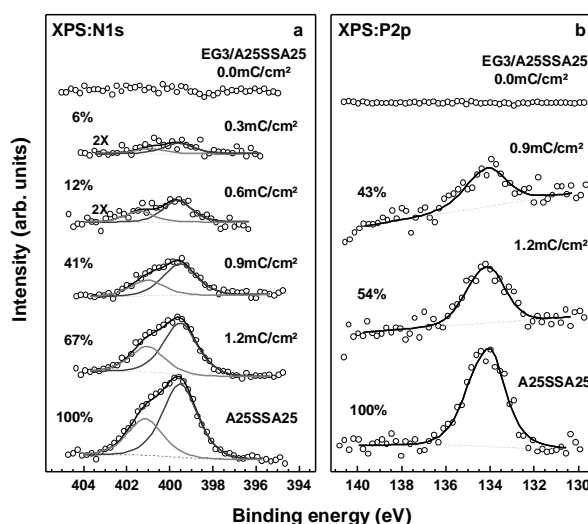


Figure 6.7 N 1s (a) and P 2p (b) XP spectra of the EG3S/A25S monolayers prepared by IPER with A25SSA25 as substituent. The spectra of the A25S film prepared from the same precursor are given at the bottom of each panel as references. The irradiation doses (IPER) and portions of the A25S species in the films, normalized to the value for the A25S monolayer (100%), are given at the respective spectra.

Comparing the intensities of the characteristic emissions in the N 1s XP spectra of the EG3S/A25S films with the analogous values for the respective, reference A25S monolayers (bottom spectra in Figures 6.6a and 6.7a),

the relative extent of the A25S species in these films could be estimated. The respective data are presented in Figure 6.8. According to these data, A25SSOH substituent behaves similar to the A25SH one, whereas A25SSA25 is noticeably less efficient. Interesting is a particular low efficiency of IPER at low doses in the latter case, which is presumably explained by especially hard sterical demands associated with the adsorption of A25SSA25. This process involves presumably exchange of more molecules that in the case of A25SH or A25SSOH, so that a certain extent of damage, associated with a comparably high dose, is required to make it efficient.

As seen in Figure 6.8, the mixed EG3S/A25S films with a portion of the A25S moieties of 65- 70% can be prepared by IPER with both thiol and disulfide substituents at sufficiently high doses (1.0-1.2 mC/cm²). However, this portion in each particular case (A25SH, A25SSOH or A25SSA25) is related to the packing density of the A25S species in the respective reference A25S film (section 6.2.1). The latter parameter depends, however, on the precursor and is distinctly different in the A25SH, A25SSOH, and A25SSA25 cases (Figure 6.3). To be able to compare the compositions of the EG3S/A25S films for the different substituents, a general normalization is necessary. As such, the

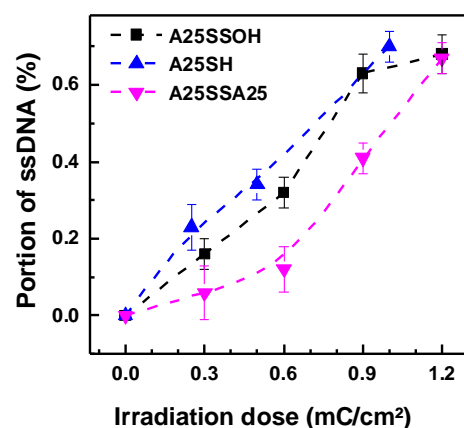


Figure 6.8 Portions of the A25S species in the EG3S/A25S films prepared by IPER with A25SSOH (square), A25SH (up triangle), and A25SSA25 (down triangle) as substituents as functions of irradiation dose. The values were derived from the N 1s XP spectra (Figures 6.6 and 6.7 and ref 53) ; the intensities of the N 1s signal were normalized to the N 1s intensities for the respective A25S films.

packing density of the A25S film prepared from the A25SSOH precursor was selected, since this was the highest packing density achieved with the different precursors in this study.

The generally normalized portions of the A25S species in the mixed EG3S/A25S films prepared by IPER with the A25SH, A25SSOH and A25SSA25 substituents are presented in Figure 6.9a as functions of the irradiation dose. The absolute packing densities of these species can then be easily calculated on the basis of the reference density for the film prepared from the A25SSOH precursor (Figure 6.3). Similar to Figure 6.8, the curves for the A25SH and A25SSOH substituents are very close to one another, whereas that for A25SSA25 is distinctly different. This behaviour supports above statement that the presence of the short chain MH segment does not affect the efficiency of the promoted exchange reaction to a noticeable extent, while the MH moieties releasing after the substrate-induced cleavage of the disulfide bond become a part of the resulting EG3S/A25S films. Since they are comparably small, they hardly affect the molecular organization in the films. In contrast, the exchange reaction with the A25SSA25 substituents is much less efficient as compared to the A25SH and A25SSOH counterparts, especially at low doses, at which the difference between the curves is especially pronounced. Due to bulky character of the A25SSA25 species, the above exchange reaction should involve more molecules in the primary EG3S than in the A25SH or A25SSOH case. It is therefore only efficient after an accumulation of a certain extent of damage by many EG3S molecules, which occurs starting from a comparably high dose of 0.6 mC/cm^2 (Figure 6.9a). Above this dose, the slope of the portion vs. dose curve for A25SSA25 is similar to the A25SH and A25SSOH ones, even though the resulting contents of the A25S species in the mixed EG3S/A25S films are considerably lower.

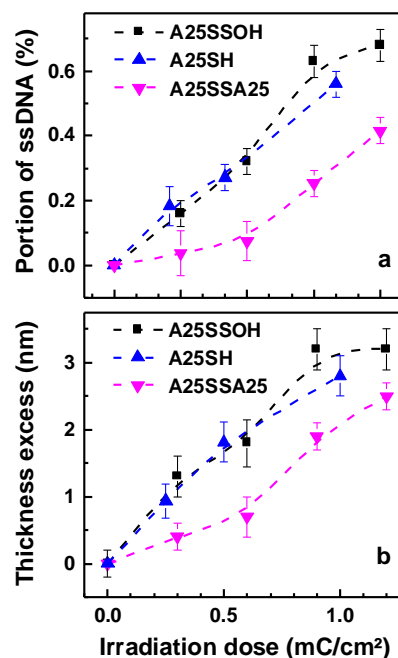


Figure 6.9 a) Portions of the A25S species in the EG3S/A25S films prepared by IPER with A25SSOH (square), A25SH (up triangle), and A25SSA25 (down triangle) as substituent as functions of irradiation dose. The values were derived from the N 1s XP spectra (Figures 6.6 and 6.7 and ref 53); the intensities of the N 1s signal were normalized to highest packing density of A25S films. (b) Difference between the thicknesses of the EG3S/A25S and EG3S monolayers. The dashed curves are guides for the eyes.

Along with the XPS measurements, the efficiency of IPER could be monitored by the ellipsometry. The relevant parameter is then the difference between the thickness of the mixed EG3S/A25S film and that of the primary EG3S template. This difference is proportional to the portion of the A25S species in the mixed films. The respective results are presented in Figure 6.9b. The curves in this figure mimic those in Figure 6.9a, exhibiting similar behaviour in the case of A25SH and A25SSOH and a distinctly different behavior in the case of A25SSA25. Also the shapes of the corresponding curves in Figures 6.9a and 6.9b are very similar. The above findings are an additional proofs for the conclusions made on the basis of Figure 6.9a.

6.3 Conclusions

The ability of disulfides ssDNA precursors to serve as substituents in IPER, resulting in mixed OEG-AT/ssDNA monolayers was tested. As representative disulfide, A25SSOH and A25SSA25 were found to be suitable for IPER. The efficiency of A25SSOH as substituent occurred to be similar to that of A25SH. The highest quality was achieved in the case of the A25SH and A25SSOH precursors, with the latter film exhibiting the highest packing density but slightly lower degree of the orientational order. In contrast, the A25SSA25 derived monolayers exhibited comparably low packing density and orientational order which was explained by the bulky character and conformational flexibility of A25SSA25. The portion of the A25S species in the resulting EG3S/A25S monolayers exhibited an almost linear dependence on the irradiation dose, with ultimate values of 55-65% at doses of 1.0-1.2 mC/cm². In contrast, A25SSA25 showed two somewhat different regimes. At higher doses, the portion of the A25S species showed a similar increase with increasing dose as in the A25SH and A25SSOH case, but the absolute values were somewhat lower, achieving ~40% at a dose of 1.2 mC/cm². Similar, to the case of the reference films, the particular behavior of A25SSA25 was associated with its bulky character and conformational flexibility. This required involvement of a large amount of the EG3S molecules in the exchange process, which is only possible at high irradiation dose, necessary to produce sufficient damage to the primary EG3S monolayer.

7. Fabrication of ssDNA/Oligo(ethylene glycol) monolayers and patterns by exchange reaction promoted by ultraviolet light irradiation

In the previous chapters, it was clearly demonstrated that thiolated and disulfide ssDNA molecules can be embedded into bio repulsive background (OEG-AT) by electron irradiation promoted exchange reaction, resulting in the formation of mixed film. If irradiation is performed homogeneously, mixed ssDNA/OEG-ATs film of desired composition can be prepared. If irradiation is carried out in lithographic fashion, ssDNA/OEG-ATs spots of desired composition and shape can be “written” in the biorepulsive ssDNA/OEG-ATs matrix, allowing the precise control of the packing density of ssDNA within each individual spot.^{53,216}

In spite of all above advantages, the use of the IPER approach is not always easy, since it requires high vacuum and, in the case of advanced patterning, relies on complex experimental setups such as scanning electron microscopes (SEM) with pattern generator systems.^{39,53,59-60} In contrast, the use of this approach in combination with ultraviolet (UV) lithography does not require such complex equipment and can be performed under ambient conditions.^{41,61}

In view of the above arguments, the experimental results on the fabrication of ssDNA/OEG-ATs monolayers and patterns by UV light promoted exchange reaction (UVPER) approach are presented here. The UV irradiation was performed at two different wavelengths, viz. 254 and 365 nm. UV light with a wavelengths of ~254 nm is most frequently used for SAM patterning, requiring, however, quite expensive UV laser sources and UV compatible optics in the case of high resolution patterning.^{64,68-69} UV light with a wavelengths of ~365 nm or even higher (up to 390 nm) is also suitable for SAM patterning^{41,61} and can be potentially combined with well-developed standard optics as well as with commercial patterning strategies such as maskless lithography.⁷⁰⁻⁷¹

7.1 Preparation and characterization procedures

7.1.1 Preparation of mixed A25SH/EG3 films by UVPER

A detail description of EG3, A25SH and mixed film preparation can be found in chapter 10. The relevant molecules are schematically shown in figure 7.1. Mixed A25SH/EG3 films were prepared by irradiation of EG3 films by UV light with a wavelength of either 254 or 365 nm. Exchange reactions were carried out by immersion of the irradiated EG3 films in a 3 μ M solution of A25SH in 1 M CaCl₂-TE buffer for 3 h at a temperature of 37°C. After immersion, the samples were carefully rinsed with Millipore-grade water, sonicated for 60 s followed by

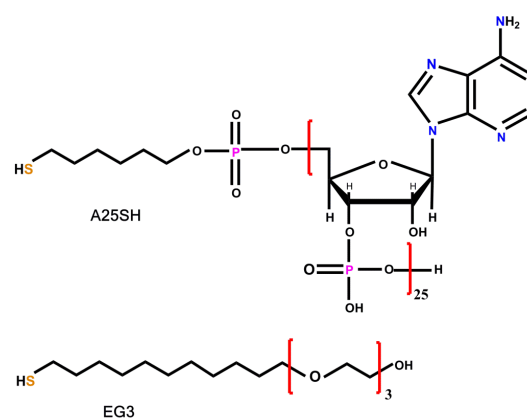


Figure 7.1 The target molecules of the present study, along with their abbreviations

rinsing with water for 60 s to remove loosely bound ssDNA species. Finally, the samples were blown dry in an argon stream. As a negative control, non-irradiated EG3 films were immersed in A25SH as well, to check for so called zero dose exchange reaction.⁴¹

7.1.2 Fabrication of ssDNA nanostructures by UVPER

Along with the preparation of the mixed A25SH/EG3 monolayers, representative A25SH/EG3 patterns were fabricated by proximity printing lithography. For this purpose, EG3 films were irradiated by UV light (254 nm) through a mask (Science Services. T601-Cu) with a dose 3 J/cm^2 and subsequently subjected to the exchange reaction with A25SH under the same conditions as in the case of the homogeneous irradiation. To visualize the fabricated A25SH/EG3 patterns, it was used as templates for surface-initiated enzymatic polymerization (SIEP) to grow single-strand adenine deoxynucleotide (poly(A)) brushes.

7.1.3 Fabrication of ssDNA brushes

A detail description of growth of polymer brushes can be found in chapter 10. In addition, possibility to adjust the height of poly(A) brushes by selection of the parameters of the SIEP was tested. For this purpose, enzyme concentration and the duration of the SIEP reaction were varied (table 7.1)

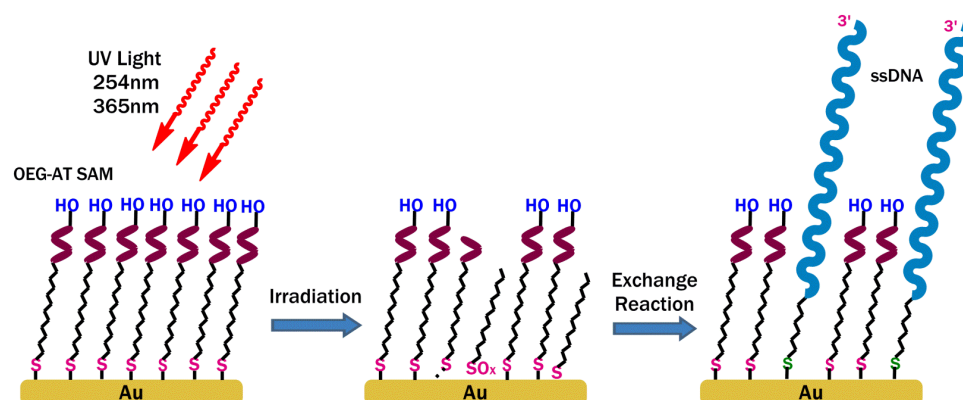


Figure 7.2. Schematic of the experimental procedure. In the first step, the primary, biorepulsive EG3 SAMs were either homogeneously irradiated or patterned by UV light. In the second step, irradiated and pre-patterned SAMs were subjected to the exchange reaction with A25SH, resulting in the formation of mixed EG3/A25SH SAMs and patterns.

7.2 Results and Discussion

The general experimental procedure to prepare mixed A25SH/EG3 SAMs and patterns is schematically illustrated in Figure 7.2. In the first step, the primary EG3 SAMs were either homogeneously irradiated by UV light with a certain wavelength (254 or 365 nm) or patterned in proximity printing geometry. In the second step, irradiated or pre-patterned SAMs were subjected to the exchange reaction with A25SH.

One-component EG3 and A25SH SAMs as well as mixed A25SH/EG3 monolayers prepared by UVPER were characterized by laboratory and synchrotron-based XPS and angle-resolved NEXAFS spectroscopy. The poly(A) brush patterns were imaged with atomic force

microscopy (AFM) and scanning electron microscopy (SEM). The thickness of the fabricated brushes was measured by ellipsometry.

7.2.1 Extent of UVPER

The extent of the UVPER reaction, i.e. the composition of the resulting, mixed A25SH/EG3 monolayers could be monitored by the specific N 1s XP spectra, using the one-component A25SH SAM as the reference; similar procedure has been successfully applied before.⁵³ The respective spectra are shown in Figures 7.3a and 7.3b for the case of 254 and 365 nm UV light, respectively. The spectrum of the one-component A25SH SAM exhibits an asymmetric broad peak which is characteristic of the adenine nucleobase and correlates well with the published data for the adenine-based ssDNA films.^{53,55-56,72,74,79} In accordance with literature data,^{53,55-56,72,74,79} this peak can be decomposed into two emissions at ~ 399.5 and ~ 401.2 eV, with a larger spectral weight for the former peak. The same adenine specific peak is also observed in the spectra of the EG3 monolayers subjected to UVPER suggesting an efficient, UV-light promoted exchange reaction. Significantly, no signature of this peak is observed in the case of the negative control, which is the non-irradiated EG3 film subjected to the exchange reaction with A25SH (top spectrum in Figure 7.3b). Thus, the exchange reaction does not occur without an exposure to UV light, which is of primary importance for the UVPER based lithography, ensuring an ultimate contrast of the ssDNA content between the UV light exposed and non-exposed areas.

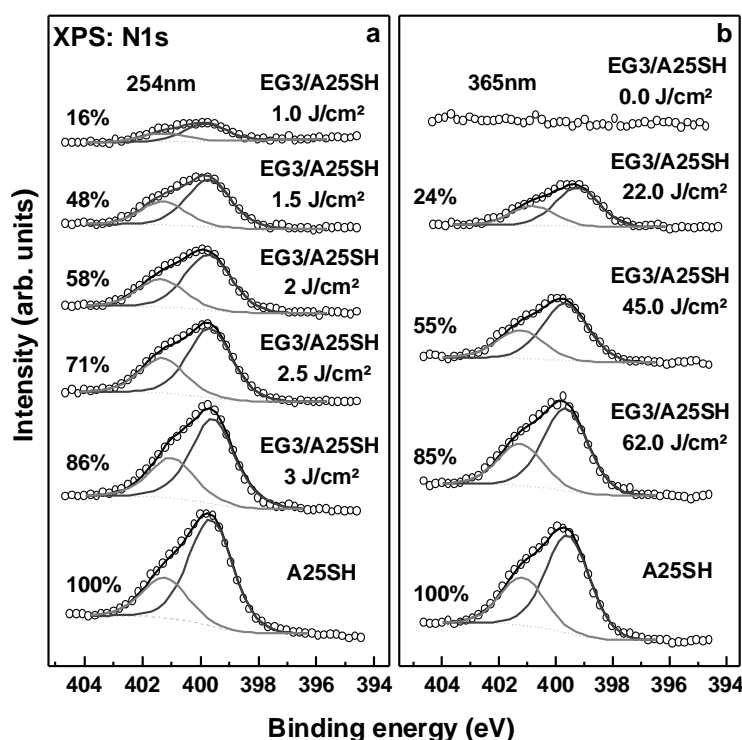


Figure 7.3 N 1s XP spectra of the reference A25SH monolayer and mixed EG3/A25SH films prepared by UVPER with a wavelength of either 254 nm (a) or 365 nm (b). The spectra are tentatively decomposed in two emissions. Irradiation doses and portions of A25SH in the films are given at the respective curves. The spectrum of the non-irradiated (0 J/cm²) EG3 monolayer exposed to A25SH is shown as well in (b).

As seen in Figure 7.3, the intensity of the adenine specific peak in the spectra of the mixed A25SH/EG3 films increases with increasing UV dose. This is exactly what one can expect in view of the progressing damage of the EG3 film upon its exposure to UV light. Another important observation is much higher UV doses required for the efficient exchange reaction for the 365 nm light as compared to 254 nm. This behaviour agrees well with the previous observations related to the imbedding of protein receptors into the OEG-AT matrix by UVPER with different wavelengths.^{41,61} Both the cross-sections of the major UV-induced processes in the OEG-AT monolayers and the outcome of UVPER showed strong dependence on the wavelength, with the lower cross-sections and, consequently, lower efficiency of UVPER at a longer wavelength.^{41,61}

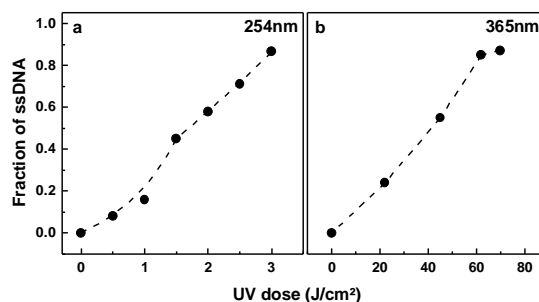


Figure 7.4 A25SH content in the mixed EG3/A25SH films prepared by UVPER with a wavelength of either 254 nm (a) or 365 nm (b) as a function of UV dose. The dashed lines are guides for the eyes.

Referring the intensity of the characteristic adenine signal to that for the one-component A25SH film, A25SH content in the mixed A25SH/EG3 monolayers could be derived. The respective parameter is presented in Figures 7.4a and 7.4b as a function of UV dose for wavelengths of 254 and 365 nm, respectively. As seen in these figures, the fraction of A25SH in the mixed A25SH/EG3 films prepared by UVPER increases almost linearly with increasing UV dose both in the 254 and 365 nm case, achieving almost 90% at high doses. This behaviour is similar to that in the case of the analogous IPER procedure performed with the same test compounds, but the ultimate fraction of A25SH is lower in the later case, achieving ~72%.⁵³ The higher efficiency of UVPER as compared to IPER is presumably related to the photooxidation of the thiolate headgroups, which is especially favourable for the exchange reaction, and to the partial cross-linking of the damaged OEF-AT species in the case of electron irradiation.^{39,219} Similar relation between the outcomes of UVPER and IPER was also observed when non-substituted AT SAMs served as the primary matrix for these procedures.^{38,67} However, the most important conclusion from the curves in Figure 7.4 is the possibility to adjust precisely the content of ssDNA in the mixed OEG-AT/ssDNA films by UVPER. This can be done more efficiently at a wavelength of 254 nm, but can also be realized at a longer wavelength, offering new possibilities for UVPER based lithography. Note that, presumably, the mixed OEG-AT/ ssDNA films represent a stochastic mixture of the both components since a long-range lateral order is rather unlikely in view of the large differences between these components and the complex character of the OEG-AT species. Even for single component ssDNA monolayers, there are no reports on long range lateral order, to the best of knowledge.

7.2.2 Characterization of the A25SH/EG3 films: XPS

Along with the evaluation of the UVPER extent, spectroscopic characterization of the resulting, mixed A25SH/EG3 SAMs was performed. The respective XP spectra are presented in Figure 7.5, along with the spectra of the single component EG3 and A25SH monolayers serving as references.

The C 1s spectrum of the EG3 film in Figure 7.5b exhibits two characteristic emissions at 284.4 and 286.15 eV assigned to the alkyl and OEG segments, respectively.⁵⁹ The O 1s spectrum of this monolayer in Figure 7.5d exhibits only one characteristic emission at 532.5 eV assigned to the OEG segment of the OEG-AT species.⁵² No features are observed in the P 2p (Figure 7.5a) and N 1s (Figure 7.5c) spectra, in accordance with the molecular composition of EG3 (Figure 7.1).

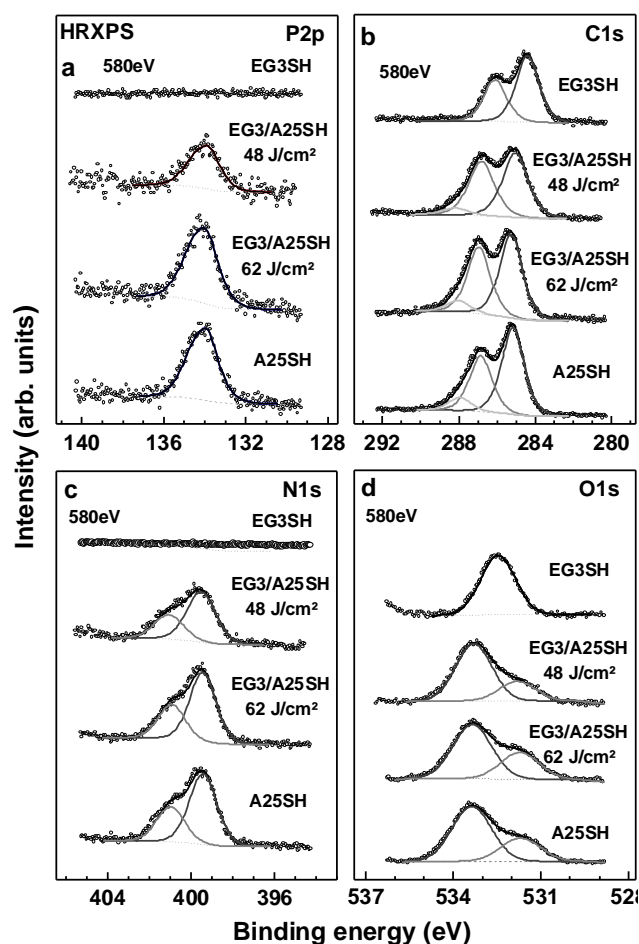


Figure 7.5 P 2p (a), C 1s (b), N 1s (c), and O 1s (d) XP spectra of the one component A25SH (bottom) and EG3 (top) SAMs as well as mixed EG3/A25SH monolayers prepared by UVP with a wavelength of 365 nm (open circles). Irradiation doses are given at the respective spectra. The C 1s, N 1s and O 1s spectra are decomposed into individual emissions (solid gray lines) by a fitting procedure. The fitted spectral envelopes are drawn by solid black lines.

The XP spectra of the A25SH monolayer are characteristic of adenine-based homooligonucleotides and agree well with the literature data for such systems.^{56,216} The P 2p spectrum in Figure 7.5a exhibits a single, slightly asymmetric peak at ~ 134.1 eV that can be assigned to the phosphorus atom in the phosphate group of the ssDNA backbone.^{56,58,217} Due to the small spin-orbit splitting (~ 0.84 eV),²²⁰ the individual P 2p_{3/2} and P 2p_{1/2} components of the P 2p doublet cannot be resolved. The C 1s spectrum in Figure 7.5b contains contributions from the carbon atoms in the adenine nucleobase and ssDNA backbone.^{79,216,218} It has a

characteristic spectral envelope and can be tentatively decomposed into three emissions at 285.1, ~286.7, and ~287.9 eV.^{79,216,218} The N 1s spectrum in Figure 7.5c was described above; the observed asymmetric peak, consisting of two emissions, is exclusively assigned to the nitrogen atoms in the adenine nucleobase.^{53,55-56,79} Finally, the O 1s spectrum in Figure 7.5d exhibits two overlapping emissions at 531.6 and 533.4 eV, typical of ssDNA^{58,216-218} and characteristic of the sugar and phosphate group in the ssDNA backbone.^{216,218} Note that a XP signal from the thiolate headgroup could not be recorded because of its strong attenuation by the densely packed ssDNA matrix wherein the quite long A25SH molecules form an oriented monolayer.^{56,221-222} This signal could however be clearly observed for the ssDNA SAMs comprised of the shorter molecules.⁵⁶

The XP spectra of the A25SH/EG3 monolayers in Figure 7.5 mimic the respective spectra of the one-component A25SH SAMs. This is especially obvious in the P 2p (Figure 7.5a) and N 1s (Figure 7.5c) cases since EG3 does not contain the respective elements. In contrast, the C 1s (Figure 7.5b) and O 1s (Figure 7.5d) spectra should represent a superposition of the EG3 and A25SH ones. However, A25SH contains noticeably more carbon and oxygen atoms than EG3 (Figure 7.1), so that the contribution of A25SH prevails. The effect of the EG3 contribution can only be tentatively traced in the C 1s spectra of the mixed films (Figure 7.5b), revealing itself as an intensity redistribution within the spectral envelope. This redistribution is, as expected, progressive, following the decrease in the A25SH content with decreasing UV dose. Note that the decrease in the A25SH content can also be traced in the P 2p (Figure 7.5a) and N 1s (Figure 7.5c) spectra. It is, however, less obvious in the O 1s spectra (Figure 7.5d), because of the saturation of the photoelectron signal at the given, quite low kinetic energy of the photoelectrons; this saturation is mediated by the self-attenuation of the photoelectron signal.²¹⁵ Similar self-attenuation occurred of course in the case of the P 2p, C 1s, and N 1s spectra as well, but was less pronounced because the kinetic energies of the respective photoelectrons were somewhat higher.

7.2.3 Characterization of the A25SH/EG3 films: NEXAFS spectroscopy

Complementary information about the mixed A25SH/EG3 films was obtained by NEXAFS spectroscopy. This technique samples the electronic structure of the unoccupied molecular orbitals and, in this regard, is especially sensitive to the chemical composition of the samples.¹⁴⁸ In addition, NEXAFS spectra acquired in the partial electron yield (PEY) acquisition mode are much less affected by the self-attenuation of the electron signal than the analogous XP spectra, since the PEY signal is comprised not only of the elastic Auger electrons but from the inelastic secondary electrons as well.¹⁴⁸

C K-edge NEXAFS spectra of the one-component EG3 and A25SH monolayers as well as mixed A25SH/EG3 films prepared by UVPER (365 nm) are presented in Figure 7.6a. These spectra were acquired at so-called “magic angle” of X-ray incidence (55°) and are therefore exclusively representative of the electronic structure of the samples, without admixture of any effects related to molecular orientation.¹⁴⁸ The spectra of the one-component films exhibit the spectral envelopes and absorption resonances characteristic of the EG3 or A25SH species. In particular, the spectrum of the EG3 monolayer shows the characteristic resonances at ~287.5 eV (1) and ~289.5 eV (2) assigned to the Ridberg-like states associated with the C–H orbitals of the alkyl and OEG segments, respectively.²²³ The spectrum of the A25SH SAM is dominated by

two sharp, π^* -like absorption resonances at ~ 286.6 eV (3) and ~ 287.3 eV (4) characteristic of the adenine nucleobase.^{56,224} The spectra of the mixed A25SH/EG3 monolayers represent a superposition of the EG3 and A25SH spectra with the relative weights depending on the UV dose. This is additionally demonstrated in Figure 7.6b where the spectra of the mixed films are compared to the best fits by a linear combination of the spectra of the individual components (i.e. EG3 and A25SH). The fits fully reproduce the resonance pattern and spectral shape of the experimental spectra, which suggests that all (or almost all) EG3 molecules damaged by UV were exchanged by the A25SH species, because the spectra of the damaged OEG-based moieties differ significantly from those of the pristine ones,²²⁵ making a good fit impossible. Another implication of the successful fitting is a lack of disturbance of the A25SH species upon their imbedding into the EG3 matrix. A disturbance would certainly result in a change of the electronic structure, with the respective change of the NEXAFS spectrum, making a good fit by the principle components impossible.

The relative weights of the A25SH and EG3 contributions in the fitting spectra of the mixed films vary in accordance with the expected film composition. Indeed, the relative weights of the A25SH and EG3 spectra in the spectra of the mixed films are, respectively, 55% and 45% at 45 J/cm² and 85% and 15% at 62 J/cm². These compositions correlate well with the data presented in Figure 7.4b, which underlines the reliability of both evaluation procedures, based on either the normalization of the N 1s XP spectra (Figure 7.4b) or on the decomposition of the C K-edge NEXAFS spectra (Figures 7.6b and 7.6c).

In addition to the C K-edge data, NEXAFS spectra at the N K-edge were acquired. N K-edge spectra (55°) of the one-component A25SH and EG3 monolayers as well as mixed A25SH/EG3 films prepared by UVPER (365 nm) are presented in Figure 7.7a. The spectrum of the EG3 film does not exhibit any features, in accordance with the chemical composition of this compound. The spectrum of the A25SH monolayer is dominated by the prominent, π^* -like absorption resonances at ~ 399.4 eV (1) and ~ 401.3 eV (2) associated with the $N1s \rightarrow LUMO$ and $N1s \rightarrow LUMO+2$ electron transitions involving the nitrogen atoms in the adenine nucleobases.^{56,224} These resonances exhibit characteristic intensity relation, with the former feature being significantly stronger. The spectra of the mixed A25SH/EG3 films mimic that of the A25SH monolayer exhibiting the same pattern of the absorption resonances. This is additional evidence that the electronic structure of the A25SH moieties was not disturbed

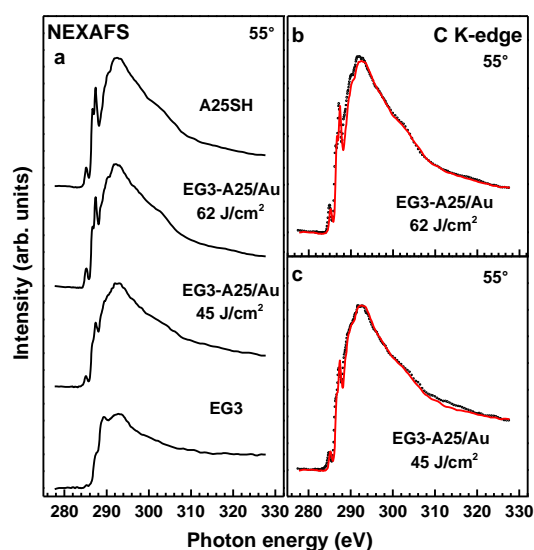


Figure 7.6 (a) C K-edge NEXAFS spectra (55°) of the one component A25SH (top) and EG3 (bottom) monolayers as well as mixed EG3/A25SH films prepared by UVPER with a wavelength of 365 nm. Irradiation doses are given at the respective spectra. (b,c) fits of the spectra of the mixed films (black) by a linear combination of the spectra of the individual components (red). The relative weights of the A25SH and EG3 spectra are, respectively, 55% and 45% at 45 J/cm² and 85% and 15% at 62 J/cm². The characteristic absorption resonances are marked by numbers.

upon their imbedding into the EG3 matrix. Also, the spectral weight of A25SH decreases with decreased UV dose in accordance with the expectations and all the above data.

In addition to the information on chemical composition, NEXAFS spectroscopy provides insights into molecular order and orientation in molecular assemblies by monitoring linear dichroism effects in X-ray absorption. A convenient way to monitor these effects is to calculate the difference between the spectra acquired at normal (90°) and grazing (20°) incidence of X-rays. Such N K-edge difference spectra of the one-component A25SH monolayer and

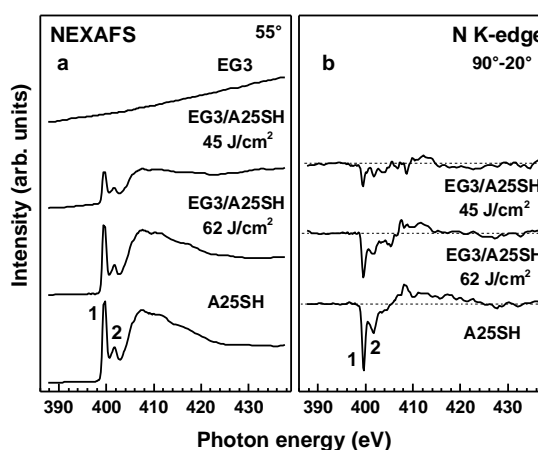


Figure 7.7 (a) N K-edge NEXAFS spectra of the one-component A25SH (top) and EG3 (bottom) monolayers as well as mixed EG3/A25SH films prepared by UVPER with a wavelength of 365 nm. The spectra were acquired at an X-ray incidence angle of 55° (magic angle). (b) Difference between the N K-edge spectra collected at normal (90°) and grazing (20°) angles of X-ray incidence for the above samples. Irradiation doses are given at the respective spectra. The characteristic absorption resonances and the respective difference peaks are marked by numbers

mixed A25SH/EG3 films prepared by UVPER (365 nm) are presented in Figure 7.7b. The difference spectrum of the A25SH monolayer exhibit pronounced peaks at the positions of the absorption resonances 1 and 2, which highlights a dependence of the resonance intensity on the angle of X-ray incidence characteristic of predominant molecular orientation in the film. Considering that the resonances 1 and 2 have the π^* character, the respective transition dipole moments (TDMs) are orientated perpendicular to the nucleobases (i.e., parallel to the ssDNA backbone). In view of this orientation, the sign of the difference peaks implies that the adenine bases in the A25SH monolayers are predominantly oriented parallel to the substrate surface, suggesting that the ssDNA strands are predominantly aligned upright, which agrees well with the literature data.^{53,216} The pronounced, negative difference peaks at the position of the absorption resonances 1 and 2 are also observed for the mixed A25SH/EG3 monolayers, suggesting that the ssDNA strands in these films are also predominantly aligned upright. The smaller amplitudes of these peaks as compared to the case of the A25SH SAM does not mean a worse orientational order, since the amplitude should be related to the height of the respective resonances in the 55° spectra, which decreases in intensity with decreasing UV dose. So-called intensity modulation amplitude, that is, the change of the normalized intensity of the resonances 1 and 2 at going from grazing to normal incidence is ~ 0.82 for both one component A25SH monolayer and mixed EG3/A25SH films addressed in Figure 7.7. In agreement with these values, evaluation of the NEXAFS data using the standard formalism,¹⁴⁸ modified slightly for the case of ssDNA monolayers,^{54,56,216} results in similar average tilt angles of the ssDNA strands in the one-component A25SH monolayer and mixed EG3/A25SH films. Indeed, these angles are $\sim 32^\circ$ for the single-component A25SH films and $\sim 31^\circ$ and $\sim 32^\circ$ for the mixed EG3/A25SH monolayers prepared at UV doses of 45 and 62 J/cm², respectively (with an accuracy of $\pm 3^\circ$). Note that, most likely, these values do not reflect the real tilt of the A25 strands but rather a degree of the orientational order in the monolayer. The individual A25

segments exhibit presumably a somewhat random distribution of different orientations,⁵⁴ along with some flexibility in orientation of individual nucleobases for each segment due to rotation relative to the backbone and from irregular bends in the backbone.

7.2.4 UVPER based patterning

UVPER can not only be used to prepare well-defined, mixed A25SH/EG3 monolayers of desired composition but, in combination with lithographic tools, be applied for the fabrication of the A25SH arrays and patterns, with the density of the A25SH species within the predefined spots being precisely controlled. As a representative example, a simple array of the square-like A25SH spots imbedded into the EG3 background by combining UVPER (254 nm; 3 J/cm²) with proximity printing lithography (Section 7.4.2). To visualize this array we used it as template to grow a poly(A) brush pattern by SIEP.⁷²⁻⁷³ The reaction was mediated by TdT, with the 3'-ends of the surface-bound A25SH serving as initiation sites for the polymerization.⁷²⁻⁷³ AFM and SEM images of the resulting poly(A) brush pattern are shown in Figures 7.8a and 7.8b, respectively, along with the corresponding height profiles. The height of the brush pattern is ~40 nm as seen in Figure 7.8a. Note that the image and height profile are somewhat smeared in the AFM case because of the rather high scan speed to measure such a large area. In this regard, the SEM image, given as 3D view and the respective height profile are better representative of the brush quality. In any case, the images presented in Figure 7.8 show that UVPER can be successfully combined with lithography resulting in the fabrication of ssDNA arrays and patterns imbedded in the biorepulsive OEG-AT matrix. Note that the pattern presented in Figure 7.8 is of course primitive and only serves to demonstrate the principle applicability of the approach. However, significantly more complex and highly resolved patterns can be prepared if UVPER is combined with more sophisticated

approaches for UV patterning such as scanning near-field photolithography,⁶² including the parallel scanning mode,⁶⁹ or interferometric lithography.⁶⁴ So far the above lithographic tools utilized UV light with a wavelength of ~254 nm. Presumably, even more flexibility can result from the use of UV light with longer wavelengths, which allows one to use less expensive optics and commercial patterning setups. In particular, variation of the ssDNA density within the predefined spots, possible in the case of UVPER, will result in the preparation of complex, gradient like ssDNA patterns which, if necessary, can be extended in the z-direction by SIEP.^{53,216}

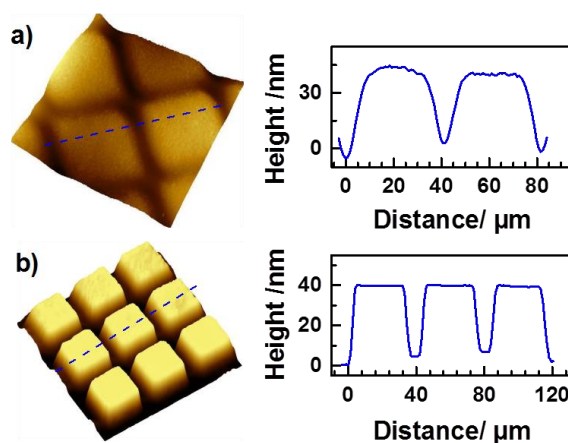


Figure 7.8 AFM (a) and SEM (b) images of a representative poly(A) brush pattern grown by SIEP on the A25SH/EG3 template prepared by UVPER, along with the respective height profiles. The SEM image is converted into 3D representation.

7.2.5 Characterization of ssDNA brushes

Note also that the ssDNA brushes and brush patterns grown by SIEP on the ssDNA/OEG-AT templates prepared by UVPER are of interest on their own. In particular, their height can be precisely adjusted in a broad range by the variation of the parameters of the SIEP procedure as shown in Table 7.1 where representative data for several poly(A) brushes grown on the single-component A25SH templates are presented (see literature).²¹⁶

Table 7.1 Height of the poly(A) brushes grown on the one-component A25SH templates by SIEP at different enzyme concentrations and reaction time.

Enzyme concentration (U)	Reaction time (hours)	Brush height (nm)
0.1	2	22 ±2
0.15	2	34 ±2
0.2	2	45 ±2
0.1	2	28 ±2
0.1	3	46 ±2
0.1	4	66 ±2

These brushes were found to be almost identical to those of A25SH initiator, with no unambiguous traces of contamination as e.g. evidenced by the N 1s XP spectra and “magic angle” N K-edge NEXAFS spectra of several representative brushes of different thicknesses presented in Figure 7.9. Both XP and NEXAFS spectra are almost identical to those of the A25SH films in Figures 7.5c and 7.7a and show only slight, statistically driven variation upon the change in the brush height. Finally, it is worth to mention that apart from the well-defined chemical integrity and contamination-free character, the ssDNA brushes are characterized by a high degree of orientational order, with an upright orientation of individual chains.²¹⁶

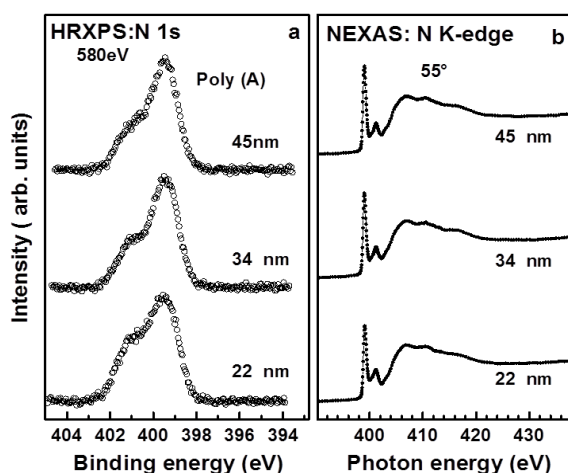


Figure 7.9 N 1s XP spectra (a) and “magic angle” N K-edge NEXAFS spectra (b) of poly(A) brushes of different thicknesses grown on the A25SH templates.

7.3 Conclusions

From the above findings, it can be concluded that, mixed ssDNA/OEG-AT monolayers can be prepared by UVPER starting from well-defined biorepulsive matrix. The composition of the mixed monolayers can be precisely adjusted in almost entire composition range (up to 90% of ssDNA) by the selection of suitable UV dose. As shown by the example of UVPER at wavelengths of 254 and 365 nm, this procedure can be performed with UV light of different wavelengths, even though significant higher UV doses are required at longer wavelengths as

compared to shorter ones. The ssDNA strands in the mixed A25SH/EG3 monolayers were found to be predominantly aligned upright, similar to the case of the one-component A25SH films. As was demonstrated by a representative example, UVPER procedure can be combined with lithography, resulting in the fabrication of the OEG-AT/ssDNA arrays and patterns imbedded in biorepulsive OEG-AT background. The fabricated OEG-AT/ssDNA patterns can be, if necessary, extended into the z-dimension by SIEP, which may result in sculpturing complex ssDNA brushes.

8. Spectroscopic study of ssDNA brushes prepared on ssDNA templates

In the previous chapters, the ssDNA patterns were fabricated and in some case extended into the z-dimension by surface-initiated enzymatic polymerization (SIEP), result in nanostructured ssDNA brushes.⁵³ These brush are also of interest on their own. In contrast to SIP of synthetic polymers, there has been little effort dedicated to the in situ synthesis of biopolymer brushes on surfaces. Biological polymers have a range of useful properties and many potential applications in an interfacial context, so that methods to grow these types of polymers directly at an interface are of great interest.

SIEP of DNA exploits the ability of a template independent polymerase, terminal deoxynucleotidyltransferase (TdT), to grow a polynucleotide chain from the exposed 3'-OH group of a short oligonucleotide primer. In contrast to the fabrication methodology and application of TdT for SIEP of ssDNA, which are fairly well developed, there is significantly less information about the internal structure of these DNA brushes. To this end, detailed spectroscopic characterization of ssDNA brushes that were polymerized by SIEP are presented in this chapter. To simplify the analysis of the experimental data, the brushes of a homopolymer of deoxynucleotide (deoxyadenosine triphosphate (dATP)) were synthesized. Note that the use of homo-oligomers is a popular approach to study complex ssDNA systems,^{53-55,57-58,75-76,78} as demonstrated in the previous chapters.

To investigate the chemical integrity, purity and possible internal alignment of model single-strand (ss) adenine deoxynucleotide (poly(A)) DNA brushes, a combination of synchrotron-based XPS and NEXAFS spectroscopy was used. Finally, to avoid any uncertainty related to the parameters of different experimental setups and to simplify the analysis of the experimental data, the powder films of adenine and SAMs of 5'-thiol-modified adenine homo-oligonucleotides as reference samples with respect to the ssDNA brushes were measured.

8.1 Preparation and characterization procedures

8.1.1 Preparation of adenine powder film

The adenine powder film, used as reference for the NEXAFS measurements, was pressed into a clean indium foil and thinned by a brush to suppress charging effects. This procedure, which is also used by other groups,²²⁶⁻²²⁷ has been optimized in lab on amino acids, peptides, and proteins, and it results in homogeneous and contamination-free films with no traces of indium in the spectra.^{192,224,228-230} It is superior to the drop casting procedure which is frequently used to prepare powder samples for spectroscopy measurements.^{227,231} The only disadvantage is a limited suppression of charging effects, which is good enough for the NEXAFS measurements but, regretfully, not sufficient for synchrotron-based XPS, even at a bending magnet beamline, such as used in the present study. Note that, the grains in the powdered films were oriented stochastically resulting in the lack of the orientational effects in the NEXAFS spectra.

8.1.2 Fabrication of ssDNA brushes on ssDNA templates

A detail description A25SH SAMs preparation can be found in chapter 10. Mixed A25SH/EG3SH films were prepared by irradiation-promoted exchange reaction.^{45,53} Briefly, the primary EG3SH films were homogeneously irradiated by electrons (10 eV) and placed in a 3 μ M solution of A25SH in 1 M CaCl₂-TE buffer for 3 h at 37°C for the exchange reaction.

As a negative control, single component EG3SH monolayers were prepared using a standard procedure,⁴⁰ i.e. by immersion of freshly prepared gold substrate into 1 mM solution of EG3SH in pure ethanol for 24 h at room temperature, with subsequent rinsing and drying.

Poly(A) brushes were grown on homogeneous A25SH and mixed A25SH/EG3SH templates in accordance with literature protocols.⁵³ Briefly, substrates bearing A25SH and A25SH/EG3SH films were applied to SIEP reaction which comprises of 0.1 U/ μ l TdT, 100 μ M dATP and 0.1% Tween 20 in 1x TdT buffer (100 mM potassium cacodylate, 1 mM CoCl₂, and 0.2 mM DTT, pH 7.2) for 1 h at 37°C. The samples were then rinsed in 1x PBS buffer with 0.1% Tween 20, followed by rinsing with water and dried with a stream of nitrogen. In some experiments, in order to obtain thicker DNA brushes (>25 nm), 1 mM dATP (higher monomer concentration) and higher enzyme concentration (up to 1.0 U/ μ l) were used in the SIEP reaction.

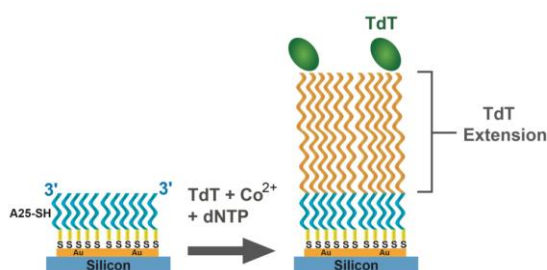


Figure 8.1 Schematic of DNA brush formation through SIEP reaction.

8.1.3 Preparation of ssDNA patterns

In addition to the spectroscopic studies, poly (A) brush patterns were grown on mixed A25SH/EG3SH templates prepared by electron beam lithography (EBL) in combination with IPER. The SIEP conditions were the same as for the homogeneous brushes.

8.2 Results and discussion

The schematic of SIEP is shown in Figure 8.1, while Figure 8.2 presents the chemical structure of the “initiator” A25SH molecule that was assembled in a SAM-like fashion on gold substrate. The dATP repeat unit in the 25-mer long initiator consists of the adenine base, sugar, and phosphate group; individual atoms of the adenine base are marked by numbers for convenience, and the entire repeat unit is marked by red square brackets. This unit is identical to those in the poly(A) brushes that are grown by SIEP.

One component and mixed monolayers, homogeneous poly(A) brushes, and poly(A) nanostructures were characterized by laboratory and synchrotron-based photoemission spectroscopy (XPS), NEXAFS spectroscopy, ellipsometry, AFM, and optical microscopy. Synchrotron-based XPS and angle-resolved NEXAFS spectroscopy measurements were carried

out at the HE-SGM beamline (bending magnet) of the synchrotron storage ring BESSY II in Berlin, Germany.

The spectra of the A25-SH films and poly(A) brushes were compared to the respective reference spectra of highly pure native polycrystalline powder films of adenine. These spectra are almost identical to those published previously.^{56,192} In case of thick films, the issue of the sampling depth of XPS and NEXAFS spectroscopy became quite essential.

The sampling depth is usually defined as the depth from which 95% of the electrons are emitted.¹⁹³ It corresponds to 3λ where λ is the attenuation length of the photoelectrons at the given kinetic energy.²¹⁵ Thus, at a photon energy of 580 eV, which used for the photoemission experiments, the sampling depths of the P 2p, C 1s, N 1s, and O 1s electrons were 4.5, 3.4, 2.7, and 2.1 nm, respectively (based on the literature λ values for densely packed molecular films).²³² So, the photoemission spectra in the given study are mostly representative of the topmost part of the A25SH films and poly(A) brushes. At the same time, the lower parts of the films contributed as well in the spectra. In particular, the signal from the substrate (Au_{4f}), even though strongly attenuated was found, for the brushes with a thickness of up to ~ 14 nm.

The sampling depth of the NEXAFS spectroscopy in the PEY acquisition mode is larger than that of the Auger electrons which mediate the PEY signal. The reason is that the signal consists not only of the elastically scattered Auger electrons but from the inelastically scattered ones as well, within the energy loss range determined by the threshold voltage. For the C K-edge this gives a factor of 2 at a proper selection of the threshold voltage.¹⁹³ Adapting this factor for the N K-edge and taking literature value for the attenuation length of the KLL Auger electrons of nitrogen,²³² a sampling depth of ~ 8.5 nm for the N K-edge NEXAFS spectra was found. This is larger than the sampling depth of the photoemission but still in the same range. Thus, for thick poly(A) brushes, also the NEXAFS spectra are mostly representative for their topmost part of the brush. However, since the brushes grew continuously with the successive parts mimicking the previous parts (presumably), it could be assumed that the spectra representative of the topmost part of the brushes are also representative of them as a whole.

8.2.1 Characterization of ssDNA brush by XPS

A25SH and poly(A) moieties consist of carbon, nitrogen, phosphorus, and oxygen atoms, all of which are, in principle amenable to quantification by XPS. A25SH also contains sulfur as a head group, necessary for the anchoring of the molecules to the substrate by the thiolate-gold bond.^{56,221-222,233} However, the S atoms were not accessible to XPS because of the strong attenuation of their signal by the densely packed ssDNA matrix wherein the A25SH molecules form an oriented monolayer.^{56,221-222,233} Such an adsorption mode is assumed in the given case based on all the experimental data. In particular, the thickness of the A25SH film was estimated at 5-6 nm which corresponds well to monolayer coverage. The density of the

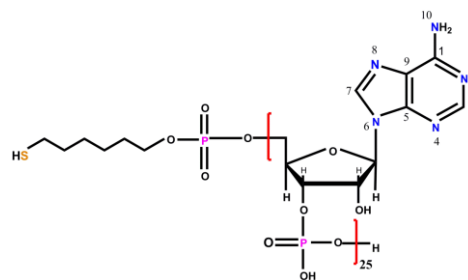


Figure 8.2 Chemical structure of the A25-SH molecule, which includes the repeat unit deoxyadenine nucleoside triphosphate (dATP) showing the base, sugar and phosphate backbone

A25SH monolayer was estimated at 6.5×10^{-13} molecules/cm² following the literature approach.⁵⁸

C 1s, N 1s, P 2p, and O 1s XPS spectra of the A25SH monolayer and poly(A) brush of ~25 nm thickness are shown in Figure 8.3; some of them have been tentatively decomposed into individual emissions based on the spectral shape and literature data for ssDNA films.^{55-56,79,218} The spectra exhibit characteristic features of adenine-based homo-oligonucleotides.^{55-56,79,218}

The absolute intensity of the spectral features in Figure 8.3 is similar for the A25SH monolayer and poly(A) brush even though the thicknesses of these films are considerably different. This is related to the strong self-attenuation of the photoelectron signals, resulting in their saturation, which is also observed for the A25SH monolayer. Thus, it is not the absolute intensity, but the individual emissions – their positions and fractional contributions to the overall spectrum – that are the relevant parameters that can be used for comparison of the A25SH monolayer and poly(A) brush. To this end, the spectra of the A25SH film and poly(A) brush are very similar, in terms of the relative spectral weights of the individual emissions, suggesting very similar chemical compositions in both cases and a lack of significant contamination in poly(A). The C 1s XP spectra in Figure 8.3a contain contributions from carbon atoms in the adenine nucleobase and ssDNA backbone. The spectrum of the A25SH initiator on gold agrees well with most of the literature data^{79,218} (slightly different spectral shapes can be found for the C 1s range in other literature).⁵⁶ This spectrum as well as the spectrum

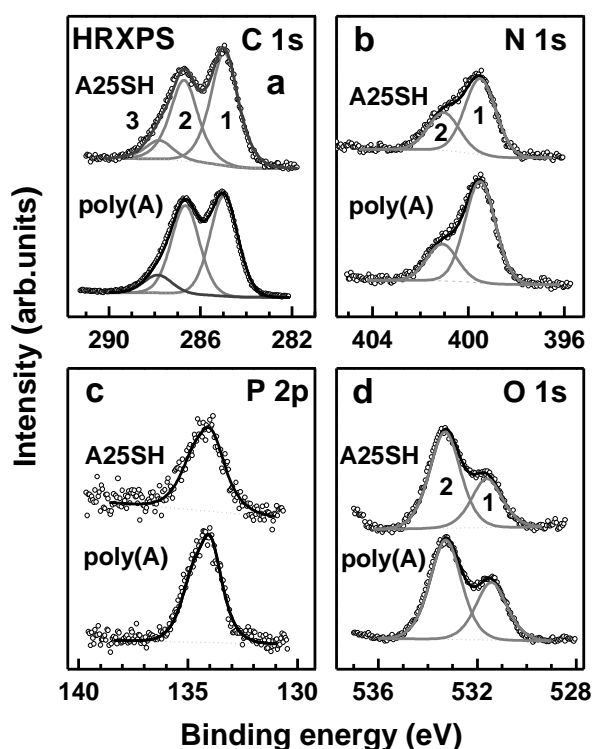


Figure 8.3 C 1s (a), N 1s (b), P 2p (c), and O 1s (e) XPS spectra of the A25-SH SAM and poly(A) brush with a thickness of 25 nm (open circles). The C 1s, N 1s and O 1s spectra are decomposed into individual emissions (solid gray lines) by a fitting procedure. The fitted spectral envelopes are drawn by solid black lines. The derived individual emissions are marked by numbers (see text for details).

of the poly(A) brush can be decomposed into three components. Their positions are very close for the A25SH film and poly(A) brush and are ~284.95, ~286.7, and ~287.9 eV. The exact assignments of these components, which will refer to as emissions 1, 2, and 3, respectively, are regrettably still elusive at the moment, in spite of some attempts to identify them.^{79,218} Tentatively, emission 1 can be assigned to the aromatic carbon in the adenine nucleobase and sugar moiety; emission 2 has a strong contribution from carbon bound to nitrogen as well as from C–O bonds of the sugar groups; and emission 3 can be assigned to the sugar-phosphate bond. Note that the C 1s spectrum of the adenine nucleobase exhibits only emissions 1 and 2, with emission 2 having a slightly higher intensity as compared to 1.²²⁶⁻²²⁷ This suggests that the ssDNA backbone contributes more strongly into emissions 1 and 3 as compared to 2. In current

study, emission 2 in the poly(A) spectrum has a slightly higher relative weight as compared to the spectrum of the A25SH monolayer, which varied to some extent from sample to sample. This can be probably related to a partial capture of the unbound dATP species in the poly(A) matrix.

The N 1s XP spectra in Figure 8.3b are representative of the nucleobases, exhibiting the spectral shape characteristic of the unique nitrogen composition of these moieties. The N 1s spectrum of the A25SH monolayers correlates well with the published data for the analogous films.^{53,55-56,79} The spectrum exhibits a characteristic asymmetric broad peak, which, in accordance with literature data,^{53,55-56,79} can be decomposed into two emissions at ~ 399.5 and ~ 401.2 eV (referred to as emissions 1 and 2, respectively), with a larger spectral weight for the former peak. The assignments of both emissions are not straightforward (see the elsewhere⁷⁹). Tentatively, emission 1 can be assigned to the conjugated nitrogen ($-N=$) while emission 2 can be assigned to non-conjugated and NH_2 nitrogen. According to this assignment, the intensity ratio of emissions 1 and 2 should be 3:2. However, not this relation but a $\sim 2:1$ ratio is typically observed for adenine-based ssDNA,^{53,55-56,79} which is also the case in the present work, both for the A25SH monolayer and the poly(A) brush. This deviation is presumably related to possible protonation or deprotonation of the individual nitrogen atoms and related functional groups. Such effects are typical for biological macromolecules and their building blocks.²³⁴

The spectrum of the poly(A) brush is very similar to the spectrum of the A25SH monolayer from which the polymer brush is grown by SIEP, both in terms of the positions and relative intensities of the individual components within the spectral umbrella. The only difference is a slightly lower relative intensity of emission 2, which can be related to the different extent of protonation/deprotonation effects in the brush as compared to the monolayer.

The P 2p XP spectra in Figure 8.3c are representative of the phosphate groups in the ssDNA backbone (Figure 8.2). The spectra of both A25SH films and poly(A) brush exhibit a single, slightly asymmetric peak at ~ 134.1 eV that can be assigned to the phosphorus atom in the phosphate group of the ssDNA backbone.^{56,58} Due to the small spin-orbit splitting (ca. 0.84 eV),²²⁰ the individual P $2p_{3/2}$ and P $2p_{1/2}$ components of the P 2p doublet cannot be resolved.

The O 1s XP spectra in Figure 8.3d are also representative of the ssDNA backbone as adenine does not contain oxygen (Figure 8.2). The spectra of both A25SH films and poly(A) brush exhibit similar spectral shapes and can be decomposed into two peaks at ~ 531.4 and ~ 533.3 eV (referred to as emissions 1 and 2, respectively), which, in the case of the A25SH SAM, agrees well with the literature data.^{58,217-218} Emission 1 can be assigned to the bridging oxygen atom in phosphate groups and the oxygen atom in sugar,²¹⁸ while emission 2 can be associated with the non-bridging oxygen atoms in phosphate groups.²¹⁸

Note that the above photoemission spectra can also contain some contributions from water and proteins which can be trapped in the A25SH SAMs and poly(A) brushes. The contribution from the trapped water can presumably appear in the O 1s spectrum at ~ 534.2 eV,²³⁵ which is at the high binding energy side of the observed emissions in Figure 8.3d. This

would result in asymmetry of emission 2, which is not the case. Therefore, the amount of the trapped water is presumably small both for the A25SH SAMs and poly(A) brushes.

The presence of the trapped proteins will affect all studied spectra. Significantly, the envelopes and the characteristics of the P 2p and O 1s spectra for the poly(A) brushes are very close to those for the A25SH SAMs where no proteins are trapped (Figures 8.3c and 8.3d). This suggests, even though tentatively, that the amount of the trapped proteins in the brushes is quite small. Further, the standard contribution of proteins in the N 1s spectra is an emission at ~ 400.6 eV,⁵⁹ which is located between emissions 1 and 2 in the spectra of the A25SH SAM and poly(A) brush in Figure 8.3b. The latter spectra can, however, be well fitted by just two peaks and do not exhibit the protein-specific signal. This confirms that the amount of the trapped proteins in the brushes is negligible.

8.2.2 Characterization of ssDNA brush by NEXAFS spectroscopy

NEXAFS spectroscopy provides complementary information on the chemical identity and composition of the samples. C, N, and O K-edge NEXAFS spectra of the powder adenine films, A25SH monolayer, and the poly(A) brush with a thickness of 25 nm are shown in Figure 8.4. These spectra were acquired at the so-called magic angle of X-ray incidence (55°) to avoid any effects related to possible molecular orientation or alignment in the investigated samples. The spectra of the adenine powder and A25SH monolayer agree well with literature data.^{54,56,192,236}

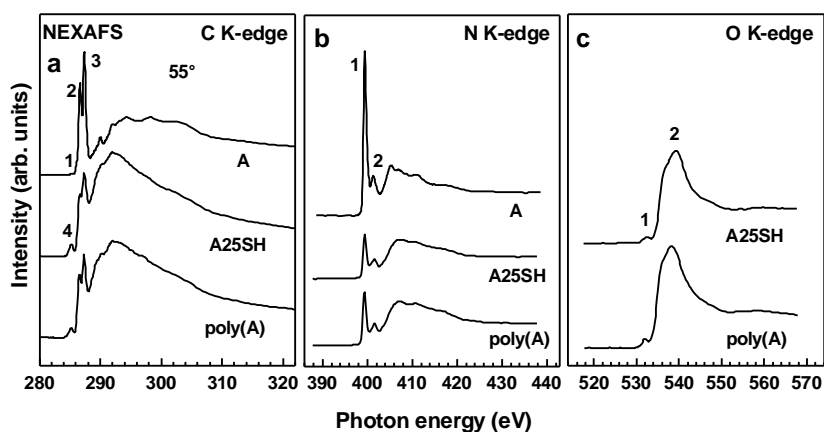


Figure 8.4 C (a), N (b), and O (c) K-edge NEXAFS spectra of adenine (powder film), A25-SH SAM, and poly(A) brush (25 nm) acquired at an X-ray incidence angle of 55° (magic angle). The most prominent resonances are marked by numbers (see text for details).

The C K-edge spectra of the A25SH monolayer and poly(A) brush in Figure 8.4a have almost identical spectral shapes and exhibit the most prominent absorption resonances of the adenine base, viz. those corresponding to the C9 \rightarrow LUMO+1 (2) and C1,3,5,7 \rightarrow LUMO (3) transitions at 286.6 and 287.3 eV, respectively.¹⁹² The C9 \rightarrow LUMO resonance (1) at 286.1 eV represents only a small shoulder of the main features¹⁹² and is not well resolved in the spectra. The most pronounced differences between the spectrum of the adenine base and those of the ssDNA monolayer and brush are: (i) a substantial step-like intensity increase at approx. 287-288 eV generated by the ssDNA backbone; (ii) a different pattern of the π^*

resonances at higher photon energies in the ssDNA spectra, stemming from the presence of the sugar and phosphate groups in the ssDNA backbone²³⁶ and (iii) the appearance of a weak resonance at 285.0 eV (4) in the monolayer and brush spectra, which, in the given case, is not perceptible in the spectrum of the adenine base in Figure 8.4a but was reported for this base in other literatures.²³⁶ This weak resonance can be tentatively associated with solid state effects or exact tautomeric state of adenine in the samples. Alternatively, it can be related to contamination.

The N K-edge spectra of the A25SH film and poly(A) brush in Figure 8.4b have very similar spectral shapes and exhibit the most prominent absorption resonances of the adenine nucleobase, viz. those corresponding to the N2,4,6,8,10→LUMO (1) and N2,4,6,8,10 → LUMO+2 (2) transitions at 399.4 and 401.3 eV, respectively. Similar to the C K-edge spectra, the spectral weight of the characteristic resonances of adenine decreases in the case of the A25SH film and poly(A) brush as compared to the spectrum of the adenine powdered film, which, in the case of the monolayer, is a typical behavior reported before by other authors.^{56,236}

The O K-edge spectra of the A25SH film and poly(A) brush in Figure 8.4c have almost identical spectral shapes and exhibit two distinct resonances at 532.3 eV (1) and 538.7 eV (2), which are related to the ssDNA backbone (phosphate and sugar) since the adenine nucleobase does not contain oxygen atoms. The spectral shape and the position of the dominant absorption maximum is similar to Na₂H_pO₄,²³⁶ which implies that the spectra of the monolayer and brush are dominated by contributions from phosphate groups. Note that the resonance 2, according to its complex spectral shape, probably consists of several individual components.

In addition to information on the chemical composition, NEXAFS spectroscopy provides insights into molecular order and orientation in these systems by monitoring linear dichroism effects in X-ray absorption. The spectra of both the A25SH monolayer and poly(A) brush exhibit noticeable linear dichroism as can be seen from the difference between the N K-edge spectra collected at normal (90°) and grazing (20°) angles of X-ray incidence (Figure 8.5). This implies the presence of orientational order in both of these samples. The difference spectra show negative peaks at the positions of the absorption resonances 1 and 2 (Figure 8.4b) and positive peaks at the positions of the resonances occurring at higher photon energies. Considering that the resonances 1 and 2 have the π* character and those at higher photon energies have α* character, the respective transition dipole moments (TDMs) are orientated perpendicular to the nucleobases (i.e. parallel to the ssDNA backbone) and along their plane (i.e. parallel to the substrate surface), respectively. In view of this orientation, the signs of the difference peaks suggest that the adenine bases both

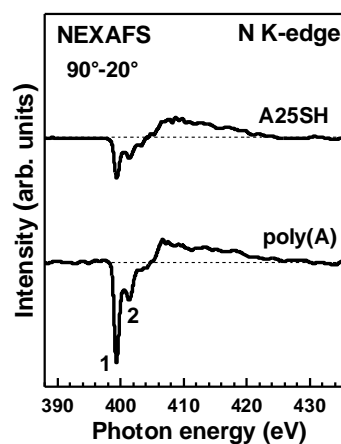


Figure 8.5 Difference between the N K-edge spectra collected at normal (90°) and grazing (20°) angles of X-ray incidence for the A25-SH SAM (top curve) and poly(A) brush (25 nm; bottom curve). The difference peaks corresponding to the most prominent resonances are marked (see text and Figure 8.4b). The horizontal dashed lines correspond to zero.

in the A25SH film and poly(A) brush are preferably orientated parallel to the substrate surface, i.e. the ssDNA strands are predominantly aligned upright.

Apart from the above qualitative considerations, a quantitative evaluation of the NEXAFS data was performed in accordance with the established procedures.^{54,56,148} Accordingly, plotted in Figure 8.6 the dependence of the normalized intensity of the most prominent α^* -like resonances at the N K-edge (1 and 2) on X-ray incidence angle for the A25SH film and poly(A) brush. The extent of the linear dichroism can then be tentatively estimated by

intensity modulation amplitude (A_π), i.e. the change of the normalized resonance intensity at going from grazing to normal incidence, which is 0.83 and 0.66 for the A25SH monolayer and poly(A) brush, respectively. Beyond this fingerprint estimate, the experimental dependences in Figure 6 were fitted by the theoretical curves for a vector-type orbital following the general formalism for the evaluation of NEXAFS data for molecular ensembles.¹⁴⁸ Because of the symmetry considerations,¹⁴⁸ the only fitting parameter was the average tilt angle (α) of the relevant molecular orbitals with respect to the surface normal. The resulting α values for the A25SH film and poly(A) brush are 32.5° and 29.5° , respectively. Note that these values are averaged over the entire ensemble of the ssDNA strands with the random azimuthal orientation of the individual bases and a definite distribution of their tilt angles. Note also that even though the absolute values of the average tilt angles have the usual accuracy of the NEXAFS experiment and data evaluation procedure, the difference between these angles has much higher accuracy and was reproduced many times in the experiments.

The most interesting and unexpected finding is the pronounced upright alignment of the individual strands in the poly(A) brush, which is the only explanation for the observed preferable orientation of the bases, that are generally perpendicular to the ssDNA backbone, even though they possess some flexibility in orientation, due to rotation relative to the backbone and its bends. According to Figures 8.5 and 8.6 as well as to the derived tilt angles, this alignment is even greater than that in the A25SH monolayers. This is quite surprising in view of the previous observations that the orientational order in the ssDNA films worsens significantly with increasing length of the ssDNA strand.⁵⁴ This was in particular observed for the monolayers of 5'-thiol-modified thymine homonucleotides on Au(111).^{54,78} This also follows from the comparison between the monolayers of short-chain⁵⁶ and long-chain⁵³ 5'-thiol-modified adenine homonucleotides. The poly(A) brushes behave opposite to this trend and exhibit relatively high orientational order, with preferable upright alignment of the individual strands. The most likely mechanism of this alignment is base stacking,^{54,58} i.e. interaction and subsequent correlation between individual bases in the process of SIEP and afterwards. This unexpected degree of orientational order in the poly(A) brush is a consequence of the high

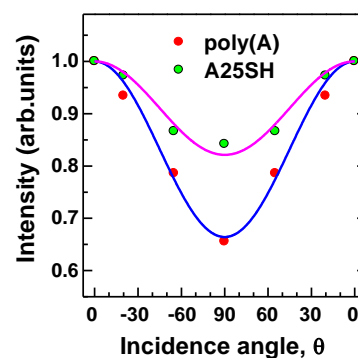


Figure 8.6 Dependence of the normalized intensity of the most pronounced absorption resonances (1 and 2; see Figure 8.4b) at the N K-edge for the A25-SH SAM (open circles) and poly(A) brush (filled circles) on the X-ray incidence angle (with respect to the surface), along with the best theoretical fits (solid lines) according to the formalism of ref 149. The data presentation follows that of refs 54 and 56.

density and the length/number of bases of these brushes. In particular, the number of bases in poly(A) brushes obtained by SIEP are impossible to achieve by grafting of long ssDNA to surface, so that despite their large molecular weight, their orientation ordering is dominated by the high interfacial density of the ssDNA and their lack of dispersity.

8.2.3 Brush thickness and density effects

Next the composition and orientation of the poly(A) brushes of different thickness was examined by measuring their characteristic N 1s XPS and N K-edge NEXAFS spectra, as the brush thickness is an important variable in controlling their structure and properties. These data are presented in Figure 8.7. The brush height was varied by either combining the A25SH initiators and EG3SH species in a mixed SAM to control the chain density^{179-180,187-190} or by

increasing the concentration of the monomer input during SIEP reaction to increase the chain length. The mixing of A25SH and EG3SH was performed by IPER,^{39,45} following an established protocol.⁵³ IPER was chosen instead of the more common method of making a mixed SAM by coadsorption of a mixture of the two thiols because IPER provides greater compositional control of the mixed A25SH/EG3SH monolayer than coadsorption, along with better reproducibility. These mixed monolayers enabled precise control of the density of SIEP initiation sites. A negative control monolayer of a pure EG3SH confirmed that no growth of the poly(A) brush occurs in the absence of the A25SH initiator (top curves) in Figure 8.7.

The N 1s XPS spectra and N K-edge NEXAFS spectra (55°) in Figure 8.7 exhibit only a slight, sample-dependent variation with varying thickness of the poly(A) brush, both in terms of the general spectral shape and positions and relative intensities of the individual emissions and absorption resonances. Due to the self-attenuation of the photoemission (XPS) and partial electron yield (NEXAFS spectroscopy) signals which occurred at almost saturation conditions, no noticeable intensity variation is observed with decreasing thickness of the poly(A) brush. A slight, continuous change is only perceptible in the NEXAFS spectra, as the effective attenuation length for the partial electron yield signal is larger than that for the elastic electrons (Section 8.1.2),¹⁹³ so that the effect of the self-attenuation is less strong.

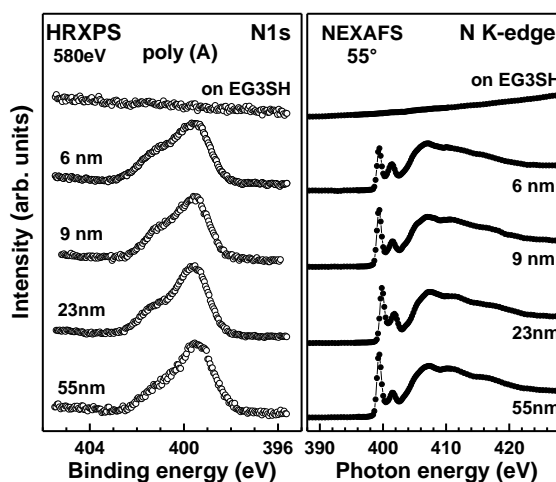


Figure 8.7 N 1s XPS spectra (left panel) and “magic angle” N K-edge NEXAFS spectra (right panel) of poly(A) brushes of different thicknesses as well as the analogous spectra of the EG3-SH SAMs on gold (top curves) subjected to SIEP at the same conditions as the A25-SH and A25-SH/EG3-SH initiator SAMs. The 23 nm brush was grown at the standard conditions (see Section 8.1.2) on a homogeneous A25-SH template. The 6 and 9 nm brushes were grown on mixed A25-SH/EG3-SH templates (lower density of the initiator) prepared by the exchange reaction as described in Section 8.1.2. The 55 nm brush was grown at a higher concentration of TdT (1.0 U/ μ l, which corresponds to the surplus situation) on a homogeneous A25-SH template. The NEXAFS spectra were acquired at an X-ray incidence angle of 55° (magic angle) to avoid effects related to molecular alignment.

Along with the “magic angle” NEXAFS spectra (Figure 8.7), the orientational order in the poly(A) brushes of different thickness was monitored. To this end, 90°-20° NEXAFS spectra of four different brushes are presented in Figure 8.8 in the same fashion as the analogous spectra in Figure 8.5. As seen in Figure 8.8, the character and extent of the linear dichroism do not noticeably change with variation of the thickness of the poly(A) brush, as long as the density of the A25SH initiator is high enough and both the length of the poly(A) chains and brush thickness are controlled by the concentration of the monomer or the enzyme. At the same time, a partial deterioration of the orientational order progressively occurs with decreasing density of the A25SH initiator as this, in particular, takes place upon its mixing with EG3SH. Whereas the length of the molecular chains – depending on the reaction conditions only – will be mostly unaffected by the initiator density, these chains get more space for coiling, resulting in decreasing thickness of the brush.

Taken together, the above results imply that the poly(A) brushes show an extraordinary degree of orientational ordering as an intrinsic property, which is largely unaffected by their thickness as long as their density is high enough, which can be controlled by the density of the initiator sites in SIEP. This degree of orientational ordering is both remarkable and surprising.

8.2.4 Characterization of Brush patterns

Combining IPER with EBL, complex 3-D DNA structures on solid supports can be sculptured, relying on the area-selective and density-controlled imbedding of the A25SH moieties (initiator site for SIEP) into the inert EG3SH matrix and subsequent growth of the brush pattern by SIEP, with the initiator site density defining the brush height.⁵³ Two examples of such structures are given in Figure 8.9 where AFM images of a column array and an assembly of contrary running gradient-like “DNA” letters formed from poly(A) by SIEP are presented. The height of the columns in Figure 8.9a is about 50 nm while the

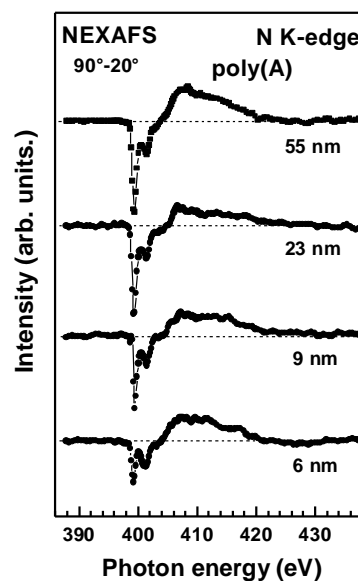


Figure 8.8 Difference between the “magic angle” N K-edge spectra collected at normal (90°) and grazing (20°) angles of X-ray incidence for several poly(A) brushes. The N 1s XPS and 55° N K-edge NEXAFS spectra of these brushes are shown in Figure 8.7. The horizontal dashed lines correspond to zero.

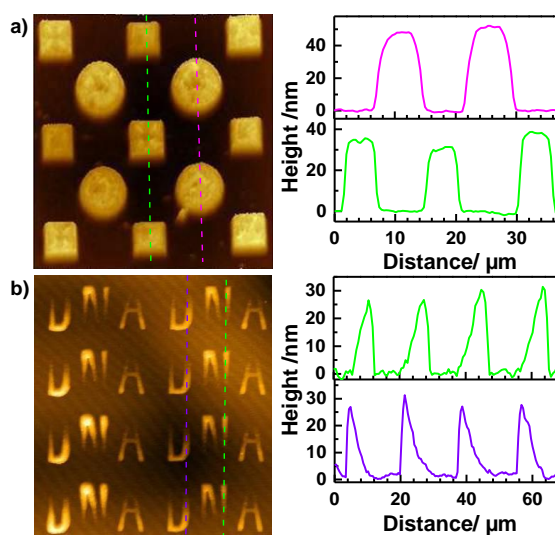


Figure 8.9 AFM images (from-top 3D view) of representative poly(A) brush patterns grown by SIEP on the A25SH/EG3SH templates prepared by IPER-EBL, along with the respective height profiles (color-coded). (a) an array of circular and square columns; (b) an assembly of contrary running gradient-like “DNA” letters. The size of the images is 37 x 40 and 70 x 70 μm^2 , respectively.

maximum height of the gradient pattern in Figure 8.9b is about 30 nm. The height of the latter brush pattern varies continuously along the letters, with the opposite directions of change for each two adjacent letters. Whereas the density of the A25SH initiator was set constant by IPER-EBL within the areas where the columns were grown by SIEP (Figure 8.9a), this density was varied in the gradient fashion within the areas where the “DNA” letters were grown by SIEP (Figure 8.9a). The A25SH density was then transformed into the certain height of the poly(A) brush, relying either on stretching or coiling of the growing molecular chains. As a result, gradient-like 3-D poly(A) pattern was sculptured.

8.3 Conclusions

The chemical integrity, purity, orientation, and ordering in the poly(A) brushes were probed by a combination of synchrotron-based XPS and angle-resolved NEXAFS spectroscopy at all relevant absorption edges. The recorded spectra of poly(A) brushes were found to be almost identical to those of the well-defined A25SH monolayers, with only slight differences related presumably to the specific extent of the protonation/deprotonation processes involving the nucleobases. Along with the chemical integrity and contamination-free character of these films, the surface anchored poly(A) brushes were found to have a high degree of internal orientational order with preferable upright orientation of individual strands. This behavior was characteristic of all studied brushes, independent of their height in a thickness range of 10 – 55 nm and mostly unaffected by the parameters of SIEP in a reasonable range of their variation. A most likely mechanism of the preferable alignment is base stacking, i.e. interaction and subsequent correlation between individual bases in the process of SIEP and afterwards.

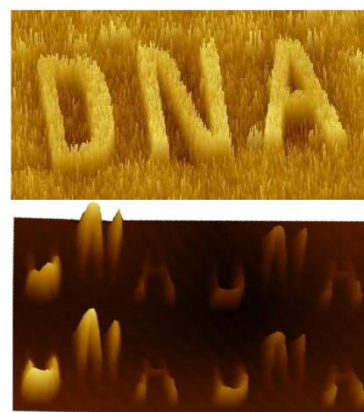
9. Summary and outlook

Controlled immobilization of biological molecules on surfaces and interfaces is one of the key challenges and technologically relevant issues in modern biology and medicine. The organization and hybridization of surface-bound DNA in particular is an important component in many established, new, and emerging medical, biological and related technologies.

This work describes a universal two-step procedure to fabricate mixed ssDNA/OEG-AT monolayers and complex ssDNA patterns in a biorepulsive background on gold substrates using exchange reaction promoted by electron or UV light irradiation treatment.



Accordingly, a primary monolayer of a test OEG-AT compound, $\text{HO}(\text{CH}_2\text{CH}_2\text{O})_3(\text{CH}_2)_{11}\text{SH}$ (termed EG3) was irradiated with electrons either homogeneously or in the EBL fashion, resulting in preferential damage of the OEG segments and partial cleavage of the thiolate-gold bonds (discussed in Chapter 4). Subsequently, the film was incubated in a solution of a test thiolated homo-oligonucleotide, 5'-SH-(CH₂)₆-d(A)25-3' (termed A25SH) for the exchange reaction promoted by the above defects. The resulted mixed ssDNA/EG3 films were characterized in detail by XPS and NEXAFS spectroscopy. It was found that the proportion of the A25SH component in the mixed A25SH/EG3 monolayer can be precisely controlled by selection of the irradiation dose. Significantly, no exchange occurred without irradiation as realized by the lack of the characteristic adenine signal (N1s photoemission spectra) for the control, non-irradiated sample. Further evidence for the formation of high-quality A25SH/EG3 monolayers were provided by the NEXAFS spectroscopy. The C K-edge NEXAFS spectra of the mixed films could be reproduced as linear combinations of the spectra of the both constituents, viz. EG3 and A25SH, which shows that their electronic structures are not affected by the mixing. The mixed A25SH/EG3 films generated by IPER were also tested for hybridization by exposing them to their complementary d(T)25 strand. The degree of hybridization was estimated at ~45.5% for the A25SH/EG3 monolayers prepared by IPER with a dose of 0.5 mC/cm². The efficiency of hybridization for this monolayer is much higher than that of the one-component A25SH film (~22%). The above results demonstrate that mixed A25SH/EG3 monolayers of desirable composition can be successfully fabricated by IPER, provided that irradiation is performed homogeneously and the dose is controlled. Further the IPER approach was combined with electron beam lithography (EBL) to introduce ssDNA/OEG-AT patterns of desired composition and shape into the biorepulsive OEG-AT template. The strength of the approach was additionally demonstrated by its combination with TdT-catalyzed SIEP that could be amplified ssDNA/EG3 patterns in the z-direction. This combination provides a new methodology to sculpt complex 3D DNA nanostructures on solid supports.

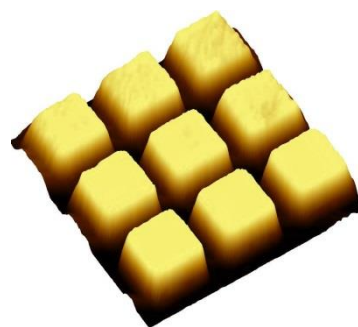


In addition to the thiolated ssDNA, asymmetric and symmetric disulfides are used frequently for the formation of ssDNA monolayers on coinage metal substrates. In this context, a question arises, whether disulfide ssDNA can serve as substituents to perform IPER with biorepulsive OEG-AT matrix. As an independent reference study, this possibility was initially tested by using a model system of a DDT SAM on gold as a primary matrix and $-COOH$ substituted dialkyldisulfides as substituents (discussed in Chapter 5). It was found that IPER can be performed with disulfide substituents in the same manner as in the case of thiols. The kinetics of the exchange reaction was found to be similar in both cases but the extent of this reaction, i.e. the ultimate portion of the substituent moieties in the resulting mixed SAMs, was to be smaller for disulfides. This can be explained by the lower probability of the exchange reaction in the case of disulfide substituents, requiring probably a special character of the exchange-promoting defects and involving a rearrangement of the adjacent intact species. It was found that mixed SAMs comprised of DDT and $-COOH$ substituted dialkyldisulfide, hold up to 60% of substituents at $1\text{mC}/\text{cm}^2$ dose. The new findings allowed the use of another commercially available disulfides molecule bearing the BIB tail group which can serve as an initiator for surface initiated polymerization (SIP). The respective chemical template was fabricated and several representative polymers, relevant for biomedical research and applications, were tested for SI-ATRP viz. pNIPAAm, pHEMA, and pEGDMA. In the case of pNIPAAm and pHEMA, a high level of control was achieved, allowing to sculpture gradient-like 3D structures of desired shape with a height up to 500 nm. In the case of pEGDMA, the selectivity of SIP was found to be poor; so that polymer brush grew over the entire template area so that brush patterns with a limited height only (up to 20 nm) were produced.



The results of the above experiments clearly showed that disulfides are suitable for IPER. So, there were no principle constraints why the disulfides ssDNA substituents would not be suitable for this procedure as well. In this context, monomolecular films based on the A25SH (reference), A25SSOH, and A25SSA25 precursors were prepared and studied in detail (as described in chapter 6). The results showed that all disulfides ssDNA substituents are suitable for mixed film preparation. The efficiency of A25SSOH as substituent was to be similar to that of A25SH. The portion of the A25S species in the resulting EG3S/A25S monolayers exhibited an almost linear dependence on the irradiation dose, with ultimate values of 55-65% at doses of $1.0\text{-}1.2\text{ mC}/\text{cm}^2$. In contrast, A25SSA25 showed two somewhat different regimes. At low irradiation doses (below $\sim 0.6\text{ mC}/\text{cm}^2$) this substituent exhibited very low efficiency in IPER, with a portion of the A25S species in the EG3S/A25S films of only $\sim 6\%$ at a dose of $\sim 0.6\text{ mC}/\text{cm}^2$. At higher doses, the portion of the A25S species showed a similar increase with increasing dose as in the A25SH and A25SSOH case, but the absolute values were somewhat lower, achieving $\sim 40\%$ at a dose of $1.2\text{ mC}/\text{cm}^2$. Similar, to the case of the reference films, the particular behavior of A25SSA25 was associated with its bulky character and conformational flexibility.

As IPER is not always easy to perform under vacuum, the possibility for the preparation of mixed ssDNA /OEG-AT monolayers as well as related patterns with UV light promoted exchange reaction were tested (discussed in chapter 7). Using a model system of the EG3 SAMs on gold as the primary film and A25SH as a representative ssDNA substituent, it was demonstrated that mixed ssDNA/OEG-AT monolayers can be prepared by UVPER starting from a well-defined biorepulsive matrix. The composition of the mixed monolayers could be precisely adjusted in almost entire composition range (up to 90% of ssDNA) by the selection of suitable UV dose. As shown by the example of UVPER at wavelengths of 254 and 365 nm, this procedure can be performed with UV light of different wavelengths, even though significant higher UV doses are required at longer wavelengths as compared to shorter ones. The extensive spectroscopic characterization of the mixed A25SH/EG3 monolayers prepared by UVPER showed that the A25SH molecules imbedded into the EG3 matrix maintained their identity and intact character. Their electronic structure was not perturbed by the interaction with the EG3 moieties, which suggests that their properties such as sensing elements with respect to the complementary ssDNA strand were not affected as well. The ssDNA strands in the mixed A25SH/EG3 monolayers were found to be predominantly aligned upright, similar to the case of the one-component A25SH films. It was also demonstrated that UVPER procedure can be combined with lithography, resulting in the fabrication of the ssDNA /OEG-AT arrays and patterns imbedded in biorepulsive OEG-AT background. The density of ssDNA moieties within the ssDNA /OEG-AT spots could be precisely adjusted. The fabricated ssDNA /OEG-AT patterns could be, if necessary, extended into the z-dimension by SIEP, which may result in sculpturing complex ssDNA brushes.



Finally, a detailed spectroscopic characterization of homogeneous ssDNA brushes of poly(A) grown by the TdT-mediated SIEP on A25SH SAMs on gold was performed (as described in chapter 8). The chemical integrity, purity, orientation and ordering in the ssDNA brushes were probed by a combination of synchrotron-based XPS and angle-resolved NEXAFS spectroscopy at all relevant absorption edges. The recorded spectra of poly(A) brushes were found to be almost identical to those of the well-defined A25SH monolayers, with only slight differences related presumably to the specific extent of the protonation/deprotonation processes involving the nucleobases. No unambiguous traces of contamination were found, even though a slight contamination cannot be completely excluded. Aside from the chemical integrity and contamination-free character of these films, the surface anchored poly(A) brushes were found to have a high degree of internal orientational order with preferable upright orientation of individual strands. This behavior was characteristic of all studied brushes, independent of their height in a thickness range of 10 – 55 nm and mostly unaffected by the parameters of SIEP in a reasonable range of their variation. A most likely mechanism of the preferable alignment is base stacking, i.e. interaction and subsequent correlation between individual bases in the process of SIEP and afterwards.

Finally, few comments can be made, also in a sense of further investigations and extension of the developed approach. The described IPER-EBL procedure relies on commercially available compounds – making it easily accessible to researchers and is highly

flexible in terms of the composition of the mixed monolayers as well as the size and shape of the ssDNA patterns that can be formed on the OEG-AT background. The approach is not limited to the compounds used herein but can be presumably implemented with almost any combination of a protein-repelling OEG-AT SAM and thiolated ssDNA. Moreover, the possibility to perform UVPER at relatively long wavelength makes possible the use of reasonably priced lasers, non-expensive UV LED sources, dynamic mirror arrays as well as standard optical and diffractive components within the lithographic setups. Also, UV light of longer wavelengths is less harmful compared to that of shorter wavelengths simplifying the design of the respective experimental setups. Note that the UVPER procedure also relies on commercially available compounds and does not require vacuum, which simplifies its application in research and industrial labs. The tunable thickness, density and orientation of ssDNA brushes synthesized by SIEP makes it, a new and experimentally attractive model system for the biointerface science community to investigate the physico-chemical properties of DNA specifically at the solid-water interface. Furthermore, the ability of TdT enzyme to catalyze the *in situ* polymerization of long and monodisperse polydeoxynucleotides, which can be patterned and sculpted into spatially complex 3-D nanoscale structures, suggest that functionally sophisticated, anisotropic nanoscale interfacial architectures should be accessible by this methodology for different applications. Further the developed 25nm pattern of DNA by the IPER-EBL approach sheds new light towards the preparation of DNA based biosensors, biochips, and recognition of complementary DNA, protein from labs to industries.



10. Experimental part

In this section all experimental details regarding different mixed SAMs preparation as well as various polymer brushes preparation techniques are discussed. Furthermore, an overview of the used lithographic procedure and analytical techniques will be given.

10.1 Preparation of self-assembled monolayers on Au

Self-assembled monolayers (SAMs) give access to surfaces with well-defined and tunable properties. The most frequently used strategies to obtain highly ordered SAMs are self-assemblies of alkanethiols (ATs) on gold.

10.1.1 Substrates and chemicals

Gold substrates were purchased from Georg Albert (PVD-Beschichtungen, Germany). In brief, the gold substrates, which were used for the SAM preparation, were fabricated by thermal evaporation of 100 nm of gold (99.99% purity) onto polished single-crystal silicon (100) wafers (Silicon Sense) that had been precoated with a 5 nm titanium adhesion layer. Such evaporated films are polycrystalline in nature with a grain size of 20-50 nm as observed by atomic force microscopy. They are considered to be standard substrates for thiol-derived SAMs. The grains predominantly exhibit a (111) orientation, which is, in particular, supported by the observation of the corresponding forward scattering maxima in the angular distributions of the Au 4f photoelectrons and by the characteristic binding energy (BE) shift of the Au 4f surface component.^{222,237}

All chemicals for SAMs formation such as EG3 ($\text{HO}(\text{CH}_2\text{CH}_2\text{O})_3(\text{CH}_2)_{11}\text{SH}$), Dodecanethiol (DDT), 11-mercaptoundecanoic acid (MUDA), 11,11'-dithiobis-undecanoic acid (DTUDA), 11,11'-Dithiobis[1-(2-bromo-2-methylpropionyloxy)undecane] (DTBUD) and ssDNA compounds, viz. A25SH, A25, and T25 were purchased from Sigma-Aldrich and used as received. TdT and adenine mononucleotide (dATP) were purchased from Promega (Madison, Wisconsin, USA) and used as received. All solvents as well as monomers and chemicals for the polymer growth were also purchased from Sigma-Aldrich Chemie GmbH, Germany. De-ionized and reverse osmosis purified water with a resistivity $>18.2 \text{ M}\Omega \text{ cm}$ was used in all experiments.

All glassware and tweezers used for samples preparation were intensely washed with ethanol before use and dried in oven. Au substrates were cleaned by a UV light emitting reactor (150W mercury vapor lamp, Heraeus noblelight, Germany, model TQ150) for a minimum of 2.5 h shortly prior to monolayers preparation in order to remove organic adsorbates from the surface. After that, the samples were rinsed with ethanol and dried by nitrogen flow and then added to the respective thiol solution. (Figure 10.1) After the given immersion time in dark at room temperature, the samples were removed from the thiols solution, rinsed with ethanol, treated in an ultrasonic bath for 1 min. Finally, the samples blown dry in flow of nitrogen. The samples were stored under pure nitrogen or in some case Argon atmosphere until used for the experiments.

10.1.2 Preparation of EG3 and A25SH monolayers

The EG3 monolayers were formed by immersion of freshly prepared gold substrates into 1 mmol solution of EG3 in pure ethanol for 24 h at room temperature, following literature protocol.⁴⁰ After immersion, the samples were carefully rinsed with the solvent, and blown dry with argon. The one component A25SH monolayers were prepared in accordance with literature protocols.^{57,76} Briefly, Au substrates were immersed in 3 μM A25SH solution in 1 M CaCl_2 -TE buffer (1 M CaCl_2 , 10 mM Tris-HCl, 1 mM EDTA, pH 7.0) for 40 h at a temperature of 37°C. Afterward, the samples were rinsed with Millipore-grade water, sonicated with water for 60 s followed by rinsing with water for 0.5 min to remove loosely bound A25SH species. Finally, the samples were blown dry with Ar.⁷⁸ The density of the one component A25SH monolayer was estimated at 6.5×10^{-13} molecules/ cm^2 following the approach described in literature.⁵⁸ This gives a molecular area of $\sim 154 \text{ \AA}^2$ which is considerably larger than the analogous value for AT-OEG SAMs ($\sim 21.4 \text{ \AA}^2$).⁵²

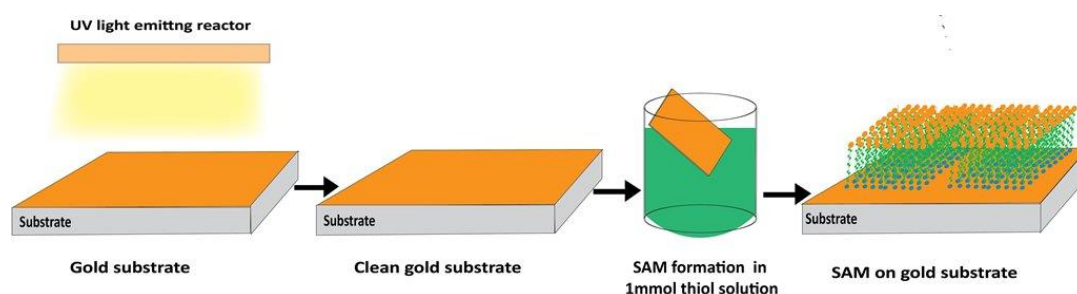


Figure 10.1 Scheme of SAM preparation protocol. First the substrate is cleaned by UV light, rinsed with ethanol and subsequent immersed in thiol solution for 24 h.

10.1.3 Preparation of DDT, MUDA, DTUDA, and DTBUD monolayers

The primary DDT SAMs (matrix) and single-component monolayers prepared from the MUDA, DTUDA, and DTBUD precursors (references) were formed by immersion of Gold coated substrates into 1 mmol ethanolic solutions of the respective molecules at room temperature. After immersion, the samples were carefully rinsed with pure ethanol, and blown dry with argon. No evidence for impurities or oxidative degradation products was found. Note that the DTUDA and DTBUD precursors were assumed to split into two COOH-AT or two BIB-AT species, respectively, upon the adsorption, following the substrate-mediated cleavage of the disulfide bond. The same was true for the case of IPER.

10.2 Preparation of two components monolayer on Au

10.2.1 Preparation of A25SH/EG3 films by IPER

To prepare mixed films, the primary EG3 SAMs were homogeneously irradiated with 10 eV electrons provided by flood gun, which are especially effective for a gentle modification of SAMs and AT SAMs, in particular.¹⁹⁵⁻¹⁹⁶ The doses were estimated by multiplication of the exposure time with the current density ($\sim 15 \mu\text{A}/\text{cm}^2$). The electron gun was mounted at a

distance of ~15 cm from the sample to ensure uniform illumination. The base pressure in the chamber during the irradiation was 1×10^{-8} mbar.

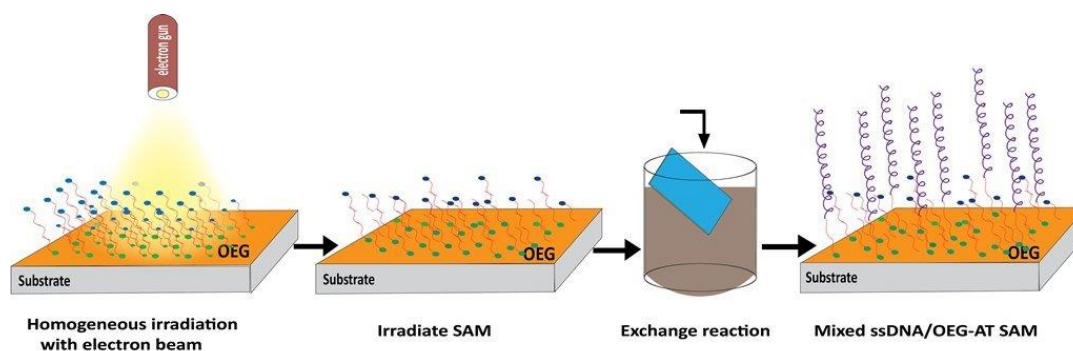


Figure 10.2 Scheme of mixed ssDNA/OEG-AT SAM preparation by irradiation promoted exchange reaction.

Exchange reactions were carried out by immersion of irradiated EG3 films in a $3 \mu\text{M}$ solution of A25SH in 1 M CaCl_2 -TE buffer for 3 h at a temperature of 37°C . After immersion, the samples were carefully rinsed with Millipore-grade water, sonicated for 60 s followed by rinsing with water for 60 s to remove loosely bound ssDNA species. Finally, they were blown dry in an Argon stream.

10.2.2 Preparation of A25SH/EG3 films by UVPER

Mixed EG3/A25SH films were prepared by irradiation of EG3 films by UV light with a wavelength of either 254 or 365 nm. The irradiation was performed homogeneously, under ambient conditions (but the ambient light was completely shadowed) using either a short wave (UV-C; 254 nm) Hg vapour lamp (Benda Konrad Laborgeräte) or a set of 365 nm LED sources (XSL-365-5E, Roithner Lasertechnik). The light intensity was measured using a UVX radiometer sensor (Ultraviolet products Ltd.) specifically adjusted for the selected wavelengths. The intensity of the UV light at a distance of 1 cm (254 nm) or 2 cm (365 nm) away from the lamp was $\sim 0.55 \text{ mW/cm}^2$ for 254 nm and $\sim 3.6 \text{ mW/cm}^2$ for 365 nm irradiation. The irradiation doses were estimated by multiplication of the light intensity with the exposure time.

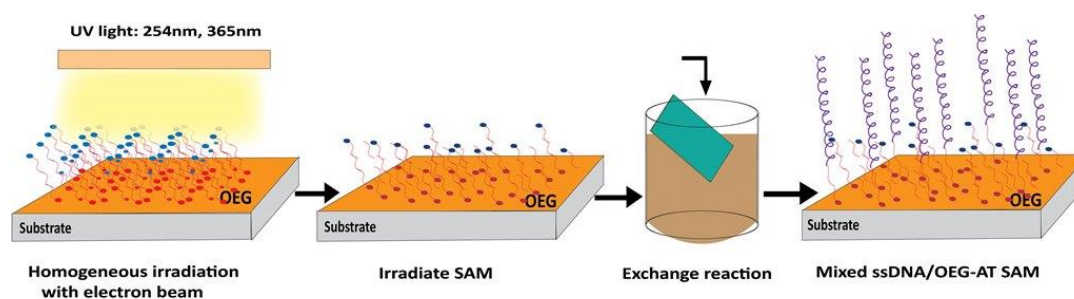


Figure 10.3 Scheme of mixed ssDNA/OEG-AT SAM preparation by UV light promoted exchange reaction.

Exchange reactions were carried out by immersion of the irradiated EG3 films in a $3 \mu\text{M}$ solution of A25SH in 1 M CaCl_2 -TE buffer for 3 h at a temperature of 37°C . After immersion, the

samples were carefully rinsed with Millipore-grade water, sonicated for 60 s followed by rinsing with water for 60 s to remove loosely bound ssDNA species. Finally, the samples were blown dry in an argon stream.

10.3 Fabrication of patterns on chemical templates

10.3.1 Fabrication of nanostructures by EBL

For the fabrication of structured chemical templates, the primary SAMs were patterned by focused electron beam using a LEO 1530 scanning electron microscope (Zeiss, Germany) with a Raith Elphy Plus pattern generator system. The electron-beam energy was chosen at 1 keV and the residual gas pressure was about 5×10^{-6} mbar. Then the patterned SAMs are subjected to exchange reaction with thiolated ssDNA molecules in solution. Finally the imbedded ssDNA molecules in OEG-AT served as an initiation site for surface-initiated enzymatic polymerization (SIEP). ssDNA brushes, poly (A) are grown on the pattern template.

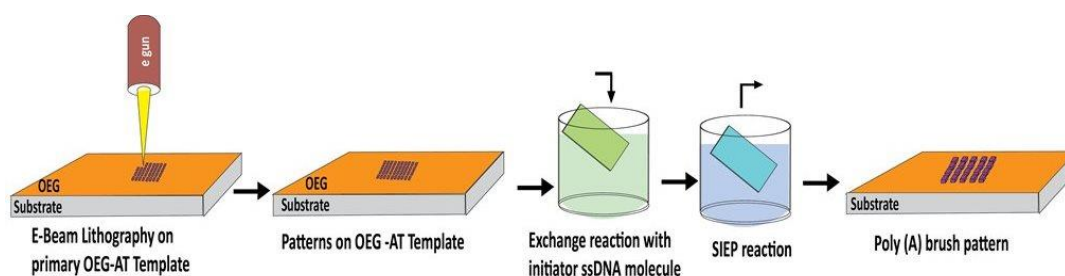


Figure 10.4 Scheme of ssDNA brush patterns preparation protocol by IPER-EBL.

10.3.2 Fabrication of nanostructures by UVPER

Along with the preparation of the mixed A25SH/EG3 monolayers, representative A25SH/EG3 patterns were fabricated by proximity printing lithography. For this purpose, EG3S films were irradiated by UV light (254 nm) through a mask (Science Services. T601-Cu) with a dose 3 J/cm² and subsequently subjected to the exchange reaction with A25SH under the same conditions as in the case of the homogeneous irradiation. To visualize the fabricated A25SH/EG3 patterns, these templates were used for SIEP to grow single-strand adenine deoxynucleotide (poly(A)) brushes.

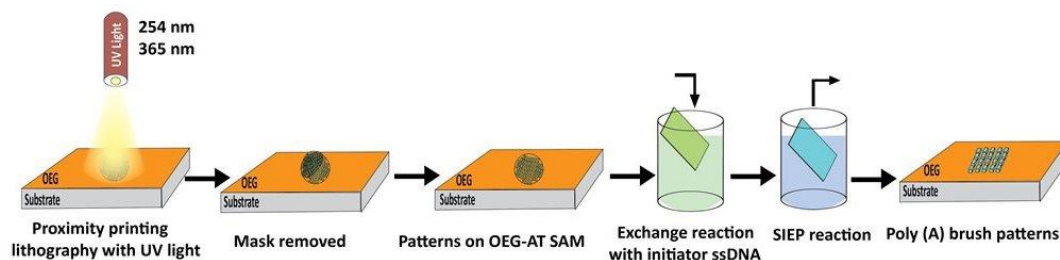


Figure 10.5 Scheme of ssDNA brush patterns preparation protocol by UVPER with proximity printing lithography.

10.4 Fabrication of Polymer Brushes

Single component SAMs formed from the DTBUD precursor as well as chemical patterns formed with DTBUD as substituent were used as templates for SIP. BIB tail groups of BIB-ATs served as initiators for this process. Three different polymer brushes were prepared, viz. brushes of poly(N-isopropylacrylamide) (pNIPAAm), poly(2-hydroxyethyl methacrylate) (pHEMA), and poly(ethylene glycol dimethacrylate) (pEGDMA).

Poly(A), i.e. DNA brushes were also grown on mixed A25SH/EG3 templates and A25SH/EG3 patterns by surface-initiated enzymatic polymerization (SIEP) reaction.

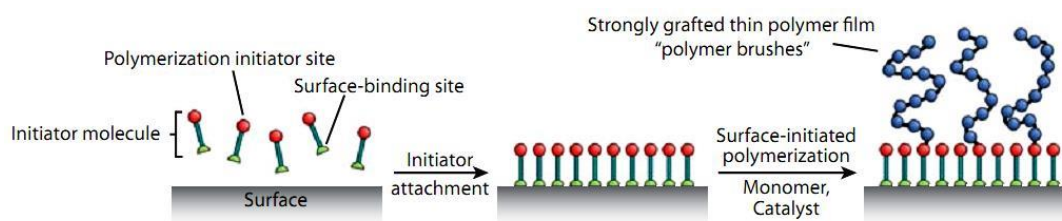


Figure 10.6 Scheme of direct polymer brush preparation process from BIB-AT SAMs, serving as an initiation site for SIP-ATRP.

10.4.1 pNIPAAm brushes

pNIPAAm brushes were prepared by surface-initiated atom transfer radical polymerization following a literature protocol,²⁰⁴ which was adapted to our laboratory. 2.1 g (18.56 mM) of the monomer (N-isopropylacrylamide; NIPAAm) was added to a degassed mixture (2 freeze pump cycles) of water and methanol (8:1 v/v, 9 ml) in a Schlenk flask. In the second flask, 2.5 mg (0.02 mM) copper(I) bromide and 18 μ l (0.05 mM) N, N, N', N'---pentamethyldiethylenetriamine were added to 1 ml of degassed (two freeze pump cycles) methanol under argon counterflow. The monomer solution was transferred from the first into second flask via a syringe and filtered with a Millipore Millex filter (0.45 μ m). The reaction mixture was treated by a Vortex for 1 - 2 min. Finally, the SAM or SAM-based chemical patterns were introduced into the reaction solution, again under argon counterflow. The reaction flask was then covered with a rubber septum and kept at room temperature for polymerization. After desired polymerization time, the samples were taken from the flask, sonicated in Milli-Q water for 2 min, rinsed with methanol, and dried under argon flow.

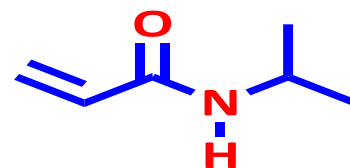


Figure 10.7 Structural formula of NIPAAm.

10.4.2 pHEMA brushes

pHEMA brushes were prepared according to a literature protocol,²⁰⁵ which was adapted to our laboratory. 4 ml Milli-Q water was degassed by two freeze pump thaw cycles before adding 4 ml freshly distilled monomer,

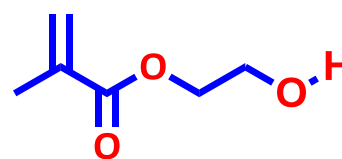


Figure 10.8 Structural formula of HEMA.

followed by the third freeze pump thaw cycle. 79 mg (0.55 mmol) of CuBr, 36 mg (0.16 mmol) of CuBr₂ and 244 mg (1.56 mmol) of 2,2'-bipyridine (bpy) were added to the aqueous solution of the monomer. The mixture was treated by a Vortex until a homogeneous dark brown solution formed. The SAMs or SAM-based chemical patterns were introduced into the reaction solution under argon counterflow. The reaction flask was then covered with a rubber septum, sealed with parafilm, and kept at room temperature for polymerization. After polymerization (for times ranging from 1 - 5 h) the samples were removed from the vial, rinsed with Milli-Q water, sonicated in dichloromethane (DMF), and dried under a flow of argon.

10.4.3 pEGDMA brushes

pEGDMA brushes were prepared according to a literature protocol,²⁰⁵ which was adapted to our laboratory. 8 ml DMF was degassed through two freeze pump thaw cycles before adding 60 mg (0.6 mmol) CuCl and 244 mg (1.56 mmol) bpy under argon atmosphere. The mixture was treated by a Vortex for 15 min to allow the salt to dissolve and to form a homogeneous dark brown solution. In a second vial, 2.5 ml Milli-Q water was degassed by using two freeze pump thaw cycles. 40 mg (0.18 mmol) CuBr₂ was added and the aqueous solution transferred into the first flask by syringe. The polymerization mixture was degassed for a third time through a freeze pump thaw cycle before the SAMs or SAM-based chemical patterns samples were introduced under argon counterflow. The reaction flask was sealed with parafilm and kept at room temperature during polymerization. Afterwards, the samples were removed from the vial, rinsed with Milli-Q water, sonicated in DMF for 20 min, rinsed with DMF, and dried under argon flow.

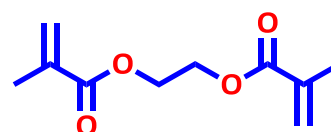


Figure 10.9 Structural formula of EGDMA.

10.4.4 ssDNA brushes

Poly(A) brushes were grown on mixed A25SH/EG3 templates and A25SH/EG3 patterns in accordance with literature protocols.⁷²⁻⁷³ Briefly, substrates bearing A25SH and A25SH/EG3 films as well as A25SH/EG3 patterns were exposed to SIEP reaction which comprises of 0.1 U/ μ l TdT, 100 μ M dATP and 0.1% Tween 20 in 1x TdT buffer (100mM potassium cacodylate, 1 mM CoCl₂, and 0.2 mM DTT, pH 7.2) for 1 h at 37°C. Where in the terminal 3'-OH of the assembled A25SH moieties served as the initiation sites for SIEP of poly(A).^{53,72-74,216} The samples were then rinsed in 1x PBS buffer with 0.1% Tween 20, followed by rinsing with Milli-Q water (resistivity > 18.2 M Ω cm) and dried with stream of nitrogen. In some experiments, in order to obtain thicker DNA brushes (>25 nm), 1 mM dATP (higher monomer concentration) and higher enzyme concentration (up to 1.0 U/ μ l) were used in the SIEP reaction.

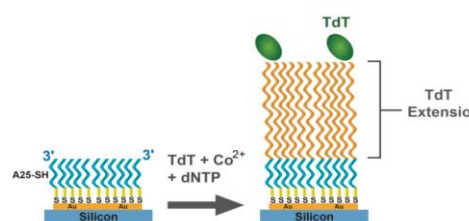


Figure 10.10 Schematic of ssDNA brush formation through SIEP reaction.

10.5 Analytical techniques

10.5.1 Spectral Ellipsometry

The thickness of homogeneous poly(A) brushes was monitored in air using an M-88[®] spectroscopic ellipsometer (J. A. Woollam Co., Inc., Lincoln, NE, USA). Samples were analyzed at fixed angles of 65°, 70° and 75°. A refractive index of 1.45 was assumed for all the brushes in the calculation of their thickness. The monolayer and brush thicknesses were fit into Cauchy model and calculated using the manufacturer's software, WVASE32[™].

10.5.2 Contact angle goniometry

The homogeneous single-component and mixed films were characterized by contact angle goniometry. Advancing contact angles of Millipore water were measured on freshly prepared samples with a Krüss goniometer Model G1. The measurements were performed under ambient conditions with the needle tip in contact with the drop. The drop volume was about 2 μl . At least three measurements at different locations on each sample were made. The averaged values are reported. Deviations from the average were less than 2°.

10.5.3 AFM measurements

AFM measurements were performed with a DI3100 microscope (Digital Instruments) equipped with a Nanoscope IIIa controller (Veeco instruments). The images were acquired in tapping mode in the repulsive force regime. In some case AFM imaging was performed with a Solver Next multifunctional Scanning Probe Microscope equipped with a SPM controller (BL900). The images were captured using standard tips in tapping mode under standard condition in repulsive force regime. The scanned data were analyzed by the local depth analysis option of the commercial AFM software by choosing the area containing the pattern.

10.5.4 Scanning electron microscopy

SEM images were obtained using a Leo 1530 Gemini SEM system (Zeiss, Germany) at an acceleration voltage of 1 kV. 2D SEM images were converted to 3D using commercial image processing software; the height of the 3D features was taken from the AFM data.

10.5.5 Optical microscopy

Optical microscopy measurements were performed with Olympus-TGH microscope, Japan in standard condition.

10.5.6 X-ray photoelectron spectroscopy

Laboratory- based XP spectroscopy

Laboratory based XP spectroscopy measurements were performed using a nonmonochromatic Mg K α X-ray source (1253.6eV) and a LHS 11 analyzer (Leybold-Heraeus GmbH, Germany). The spectra acquisition was carried out in normal emission geometry with

an energy resolution of ~ 0.9 eV. The X-ray source was operated at a power of 260 W and positioned ~ 2 cm away from the samples. All measurements were performed at a base pressure of less than 1.5×10^{-8} mbar. In addition to the detail spectra shown in the thesis, other characteristic XPS signals occur, which appear as satellite peaks in the overview spectra. At the beginning of the each measurement, a survey spectrum was recorded to verify the signal positions, which are potentially shifted through charging of the sample and furthermore to detect possible impurities on the surface. Subsequently, a detailed spectrum was recorded for the quantification of each atomic species of interest. Start and end energy state the intervals in which measurements were performed for each elements and the step size determines the energy difference between two measuring points. The parameter given in table 10.1 were used for the measurements.

Table 10.1 Parameters for recorded XP spectra

Orbitals	Start (eV)	End (eV)	Step (eV)	Dwell (S)	Pass Energy (eV)	Scan No.
WideScan	1095	-5	1.0	0.1	100	2
Au4f	87	81	0.1	0.1		2
C1s	293	280	0.1	0.1		5
O1s	538	526	0.1	0.1		3
S2p	172	158	0.06	0.20		40
N1s	405	395	0.2	0.25		20
P2p	138	128	0.2	0.25		20

To achieve the best possible resolution of the spectra, dwell time is chosen according to the signal intensity, i.e. the weaker the signal the longer the dwell time. The dwell time depends on the probability of detecting an element which is given by its cross section and its position in the material. Numerical values of cross section²³⁸ and attenuation lengths²³² are shown in table 10.2.

Table 10.2 Cross section, σ and attenuation lengths, λ for each elements

Signal	Au4f _{7/2}	C1s	O1s	S2p	N1S	P2p
σ (a.u.)	9.77	1.00	2.85	1.74	1.77	1.25
λ [\AA]	27.6	25.0	20.2	26.39	22.5	26.8

Synchrotron-based XP spectroscopy

Synchrotron-based HRXPS measurements were carried out at two synchrotron storage rings, viz. BESSY II in Berlin, Germany and MAX-lab, Sweden. At the HE-SGM beamline of BESSY II, the XPS spectra were measured using a Scienta R3000 spectrometer. The X-ray energy was set to 580 eV. The spectrum acquisition was carried out in normal emission geometry with an energy resolution of ~ 0.4 eV. At the D1011 beamline of MAX Lab, the spectra were collected by a Scienta analyzer in normal emission geometry. Linear polarized synchrotron light with a polarization factor of $\sim 95\%$ was used. The energy resolution was better than 100 meV.

Some spectra were fitted by symmetric Voigt functions using either Shirley-type or linear background. The fits were performed self-consistently, in that, the same fit parameters were used for identical spectral regions across different samples. However, due to irradiation induced damage of the films, a balance between these two counteracting effects of resolution and damage has to be chosen. The energy scale of the XPS spectra was referenced to the Au $4f_{7/2}$ peak at a binding energy (BE) of 84.0 eV.²²⁰ The obtained spectra were fitted and analyzed qualitatively and quantitatively with XPSPEAK 4.1 software. All experiments were performed at room temperature and UHV conditions at a base pressure lower than 1×10^{-9} mbar. The spectrum acquisition time was selected in such a way that no noticeable damage by the primary X-rays occurred during the experiments.^{129,239-240} Most of the measurements were repeated several times on different samples, with good reproducibility of results.

10.5.7 NEXAFS spectroscopy

Synchrotron-based angle-resolved NEXAFS spectroscopy measurements were carried out at two synchrotron storage rings, viz. BESSY II in Berlin, Germany and MAX-lab, Sweden. In detail, at the HE-SGM beamline (bending magnet)²⁴¹ of Bessy II, linear polarized synchrotron light with a polarization factor of ~ 0.91 was used. The energy resolution of the whole setup was estimated to be on the order of 0.3-0.4 eV, getting lower with the increasing photon energy. At the MAX lab, the measurements were carried out at the D1011 beamline (bending magnet), equipped with a SCIENTA SES200 electron energy analyzer and a partial electron (PEY) detector. Linear polarized synchrotron light with a polarization factor of $\sim 95\%$ was used. The energy resolution was ~ 0.1 eV.

The acquisition of the NEXAFS spectra was performed at the C, N, and O K-edges in the partial electron yield (PEY) mode with a retarding voltage of -150 , -300 , and -350 V, respectively. The most characteristic N K-edge spectra were used to monitor the orientational order in the films and brushes. For this purpose, the incidence angle of the synchrotron light was varied from 90° (normal incidence; E-vector in the surface plane) to 20° (grazing incidence; E-vector near the surface normal) in steps of 10 - 20° . This approach is based on the dependence of the cross-section of the resonant photo excitation process on the orientation of the electric field vector of the synchrotron light with respect to the molecular orbital of interest (so-called linear dichroism in X-ray absorption).¹⁴⁸ This effect results in a characteristic dependence of an adsorption resonance intensity on the incidence angle of X-rays as long as there is an orientational order in the probed system. The raw NEXAFS spectra were normalized to the incident photon flux by division through the spectrum of a clean, freshly sputtered gold sample. Furthermore, the spectra were reduced to the standard form by subtraction of a linear

pre-edge background and normalization to the unity edge jump (as determined by a nearly horizontal plateau 40-50 eV above the respective absorption edges). The energy scale was referenced to the most intense π^* resonance of highly oriented pyrolytic graphite (HOPG) at 285.38 eV.²⁴²

List of abbreviations

AFM	Atomic force microscopy
ATRP	Atom transfer radical polymerization
AO	Atomic orbital
AT	Alkanethiolate
BIB	2-Bromoisobutyryl bromide
BSE	Back-scattered electrons
CA	Contact angle
DDT	1-Dodecanethiol
EBL	Electron beam lithography
EBCL	Electron beam chemical lithography
EG	Ethylene glycol
ESCA	Electron spectroscopy for chemical analysis
FTIR	Fourier transform infrared spectroscopy
HOMO	Highest Occupied Molecular Orbital
HRXPS	High Resolution XPS
IPER	Irradiation promoted exchange reaction
LUMO	Lowest Unoccupied Molecular Orbital
MQ	MilliQ R
MO	Molecular orbital
NIPAAM	N-Isopropylacrylamide
NEXAFS	Near Edge X-Ray Absorption Fine Structure
OEG	Oligo(ethylene glycol)
PBS	Phosphate buffered saline
PMDETA	N,N,N',N'',N'''-pentamethyldiethylenetriamine
PNIPAAM	Poly(N-isopropylacrylamide)
PDMS	Polydimethylsiloxane elastomer
PE	Primary electron
RT	Room temperature
RAFT	Reversible addition fragmentation chain transfer
rpm	Rotation per minute
SAM	Self assembled monolayer
SE	Secondary electrons
SEM	Scanning electron microscopy
SI-ATRP	Surface-initiated atom transfer radical polymerization
SIP	Surface-initiated polymerization
STM	Scanning tunneling microscopy
TDM	Transition dipol moment
TdT	Terminal deoxynucleotidyl transferase
UV	Ultraviolet
μCP	Microcontact printing
UHV	Ultra high vacuum
XPS	X-ray photoelectron spectroscopy

Bibliography

1. C. R. Jaeger, Lithography. In *Introduction to Microelectronic Fabrication*, Prentice Hall: Upper Saddle River, 2002.
2. Fujita, S.; Maruno, S.; Watanabe, H.; Kusumi, Y.; Ichikawa, M., Periodical nanostructure fabrication using electron interference fringes produced by scanning interference electron microscope. *Applied Physics Letters* 1995, 66 (20), 2754-2756.
3. Brandow, S. L.; Chen, M. S.; Aggarwal, R.; Dulcey, C. S.; Calvert, J. M.; Dressick, W. J., Fabrication of Patterned Amine Reactivity Templates Using 4-Chloromethylphenylsiloxane Self-Assembled Monolayer Films. *Langmuir* 1999, 15 (16), 5429-5432.
4. Carter, D. J. D.; Pepin, A.; Schweizer, M. R.; Smith, H. I.; Ocola, L. E., Direct measurement of the effect of substrate photoelectrons in x-ray nanolithography. *Journal of Vacuum Science & Technology B* 1997, 15 (6), 2509-2513.
5. Klausner, R.; Huang, M.-L.; Wang, S.-C.; Chen, C.-H.; Chuang, T. J.; Terfort, A.; Zharnikov, M., Lithography with a focused soft X-ray beam and a monomolecular resist. *Langmuir* 2004, 20 (6), 2050-2053.
6. McCord, M. A.; Rooks, M. J., In *SPIE Handbook of Microlithography, Micromachining and Microfabrication*, Cornell Nano-Scale Science and Technology Facility: Ithaca, 2000.
7. Xia, Y.; Whitesides, G. M., Soft Lithography. *Angewandte Chemie International Edition* 1998, 37 (5), 550-575.
8. Chou, S. Y.; Krauss, P. R.; Renstrom, P. J., Imprint Lithography with 25-Nanometer Resolution. *Science* 1996, 272 (5258), 85-87.
9. Piner, R. D.; Zhu, J.; Xu, F.; Hong, S.; Mirkin, C. A., "Dip-Pen" Nanolithography. *Science* 1999, 283 (5402), 661-663.
10. Maoz, R.; Cohen, S. R.; Sagiv, J., Nanoelectrochemical Patterning of Monolayer Surfaces: Toward Spatially Defined Self-Assembly of Nanostructures. *Advanced Materials* 1999, 11 (1), 55-61.
11. Sun, S.; Leggett, G. J., Matching the Resolution of Electron Beam Lithography by Scanning Near-Field Photolithography. *Nano Lett* 2004, 4 (8), 1381-1384.
12. Okazaki, S., Resolution limits of optical lithography. *Journal of Vacuum Science & Technology B: Microelectronics and Nanometer Structures* 1991, 9 (6), 2829-2833.
13. Geppert, L., Semiconductor lithography for the next millennium. *Spectrum, IEEE* 1996, 33 (4), 33-38.
14. Winston, B., *Media technology and society: a history: from the telegraph to the Internet*. Psychology Press: 1998.

15. Conley, W.; LeSuer, R. J.; Fan, F. F.; Bard, A. J.; Taylor, C.; Tsiartas, P.; Willson, G.; Romano, A.; Dammel, R. In *Understanding the photoresist surface-liquid interface for ArF immersion lithography*, 2005; pp 64-77.
16. Stix, G., Shrinking Circuits with Water. *Scientific American* 2005, 293 (1), 64-67.
17. Pease, R., Nanolithography and its prospects as a manufacturing technology. *Journal of Vacuum Science & Technology B: Microelectronics and Nanometer Structures* 1992, 10 (1), 278-285.
18. Campbell, S. A., In *The Science and Engineering of Microelectronic Fabrication*, Oxford University Press, Oxford: UK, 1996; p 203.
19. ALLRESIST GMBH In *Parameter collection and overview of photoresist and e-beam resists . [online]* available at: <http://allresist.de/wEnglish/FAQ/FAQEBeamresistsEnglisch/0080aufloesung.php?navanchor=1110014> [Accessed : 08 December, 2013]: 2013.
20. Love, J. C.; Estroff, L. A.; Kriebel, J. K.; Nuzzo, R. G.; Whitesides, G. M., Self-assembled monolayers of thiolates on metals as a form of nanotechnology. *Chem Rev* 2005, 105 (4), 1103-1169.
21. Ulman, A., Formation and Structure of Self-Assembled Monolayers. *Chem Rev* 1996, 96 (4), 1533-1554.
22. Bain, C. D.; Evall, J.; Whitesides, G. M., Formation of monolayers by the coadsorption of thiols on gold: variation in the head group, tail group, and solvent. *Journal of the American Chemical Society* 1989, 111 (18), 7155-7164.
23. Folkers, J. P.; Laibinis, P. E.; Whitesides, G. M., Self-Assembled Monolayers of Alkanethiols on Gold: The Adsorption and Wetting Properties of Monolayers Derived from Two Components with Alkane Chains of Different Lengths. *J. Adhesion Sci. technol.* 1992, 6 (12), 1397-1410.
24. Bertilsson, L.; Liedberg, B., Infrared study of thiol monolayer assemblies on gold: preparation, characterization, and functionalization of mixed monolayers. *Langmuir* 1993, 9 (1), 141-149.
25. Folkers, J. P.; Laibinis, P. E.; Whitesides, G. M.; Deutch, J., Phase behavior of two-component self-assembled monolayers of alkanethiolates on gold. *The Journal of Physical Chemistry* 1994, 98 (2), 563-571.
26. Salaita, K.; Amarnath, A.; Maspoch, D.; Higgins, T. B.; Mirkin, C. A., Spontaneous "Phase Separation" of Patterned Binary Alkanethiol Mixtures. *Journal of the American Chemical Society* 2005, 127 (32), 11283-11287.
27. Hirsch, T.; Zharnikov, M.; Shaporenko, A.; Stahl, J.; Weiss, D.; Wolfbeis, O. S.; Mirsky, V. M., Size-Controlled Electrochemical Synthesis of Metal Nanoparticles on Monomolecular Templates. *Angewandte Chemie International Edition* 2005, 44 (41), 6775-6778.

28. Ballav, N.; Terfort, A.; Zharnikov, M., Mixing of Nonsubstituted and Partly Fluorinated Alkanethiols in a Binary Self-Assembled Monolayer. *The Journal of Physical Chemistry C* 2009, *113* (9), 3697-3706.
29. Venkataraman, N. V.; Zürcher, S.; Rossi, A.; Lee, S.; Naujoks, N.; Spencer, N. D., Spatial Tuning of the Metal Work Function by Means of Alkanethiol and Fluorinated Alkanethiol Gradients. *The Journal of Physical Chemistry C* 2009, *113* (14), 5620-5628.
30. Bain, C. D.; Biebuyck, H. A.; Whitesides, G. M., Comparison of self-assembled monolayers on gold: coadsorption of thiols and disulfides. *Langmuir* 1989, *5* (3), 723-727.
31. Schönherr, H.; Ringsdorf, H.; Jaschke, M.; Butt, H. J.; Bamberg, E.; Allinson, H.; Evans, S. D., Self-Assembled Monolayers of Symmetrical and Mixed Alkyl Fluoroalkyl Disulfides on Gold. 2. Investigation of Thermal Stability and Phase Separation. *Langmuir* 1996, *12* (16), 3898-3904.
32. Ishida, T.; Yamamoto, S. i.; Mizutani, W.; Motomatsu, M.; Tokumoto, H.; Hokari, H.; Azehara, H.; Fujihira, M., Evidence for Cleavage of Disulfides in the Self-Assembled Monolayer on Au(111). *Langmuir* 1997, *13* (13), 3261-3265.
33. Heister, K.; Allara, D. L.; Bahnck, K.; Frey, S.; Zharnikov, M.; Grunze, M., Deviations from 1:1 Compositions in Self-Assembled Monolayers Formed from Adsorption of Asymmetric Dialkyl Disulfides on Gold. *Langmuir* 1999, *15* (17), 5440-5443.
34. Lewis, P. A.; Inman, C. E.; Maya, F.; Tour, J. M.; Hutchison, J. E.; Weiss, P. S., Molecular Engineering of the Polarity and Interactions of Molecular Electronic Switches. *Journal of the American Chemical Society* 2005, *127* (49), 17421-17426.
35. Moore, A. M.; Dameron, A. A.; Mantooth, B. A.; Smith, R. K.; Fuchs, D. J.; Cizek, J. W.; Maya, F.; Yao, Y.; Tour, J. M.; Weiss, P. S., Molecular Engineering and Measurements To Test Hypothesized Mechanisms in Single Molecule Conductance Switching. *Journal of the American Chemical Society* 2006, *128* (6), 1959-1967.
36. Shaporenko, A.; Rössler, K.; Lang, H.; Zharnikov, M., Self-Assembled Monolayers of Ferrocene-Substituted Biphenyl Ethynyl Thiols on Gold. *The Journal of Physical Chemistry B* 2006, *110* (48), 24621-24628.
37. Ballav, N.; Schilp, S.; Zharnikov, M., Electron-Beam Chemical Lithography with Aliphatic Self-Assembled Monolayers. *Angewandte Chemie* 2008, *120* (8), 1443-1446.
38. Ballav, N.; Shaporenko, A.; Krakert, S.; Terfort, A.; Zharnikov, M., Tuning the Exchange Reaction between a Self-assembled Monolayer and Potential Substituents by Electron Irradiation. *The Journal of Physical Chemistry C* 2007, *111* (21), 7772-7782.
39. Jeyachandran, Y. L.; Zharnikov, M., Comprehensive Analysis of the Effect of Electron Irradiation on Oligo(ethylene glycol) Terminated Self-Assembled Monolayers Applicable for Specific and Nonspecific Patterning of Proteins. *The Journal of Physical Chemistry C* 2012, *116* (28), 14950-14959.

40. Ballav, N.; Terfort, A.; Zharnikov, M., Fabrication of Mixed Self-Assembled Monolayers Designed for Avidin Immobilization by Irradiation Promoted Exchange Reaction. *Langmuir* 2009, 25 (16), 9189-9196.
41. Jeyachandran, Y. L.; Terfort, A.; Zharnikov, M., Controlled Modification of Protein-Repelling Self-Assembled Monolayers by Ultraviolet Light: The Effect of the Wavelength. *The Journal of Physical Chemistry C* 2012, 116 (16), 9019-9028.
42. Winkler, T.; Ballav, N.; Thomas, H.; Zharnikov, M.; Terfort, A., Micrometer-Scale Protein-Resistance Gradients by Electron-Beam Lithography. *Angewandte Chemie International Edition* 2008, 47 (38), 7238-7241.
43. Ballav, N.; Schilp, S.; Zharnikov, M., Electron-Beam Chemical Lithography with Aliphatic Self-Assembled Monolayers. *Angewandte Chemie International Edition* 2008, 47 (8), 1421-1424.
44. Schilp, S.; Ballav, N.; Zharnikov, M., Fabrication of a Full-Coverage Polymer Nanobrush on an Electron-Beam-Activated Template. *Angewandte Chemie International Edition* 2008, 47 (36), 6786-6789.
45. Ballav, N.; Shaporenko, A.; Terfort, A.; Zharnikov, M., A Flexible Approach to the Fabrication of Chemical Gradients. *Advanced Materials* 2007, 19 (7), 998-1000.
46. Boozer, C.; Ladd, J.; Chen, S.; Yu, Q.; Homola, J.; Jiang, S., DNA Directed Protein Immobilization on Mixed ssDNA/Oligo(ethylene glycol) Self-Assembled Monolayers for Sensitive Biosensors. *Analytical Chemistry* 2004, 76 (23), 6967-6972.
47. Sassolas, A.; Leca-Bouvier, B. D.; Blum, L. J., DNA biosensors and microarrays. *Chem Rev* 2008, 108 (1), 109-139.
48. Brockman, J. M.; Frutos, A. G.; Corn, R. M., A multistep chemical modification procedure to create DNA arrays on gold surfaces for the study of protein-DNA interactions with surface plasmon resonance imaging. *Journal of the American Chemical Society* 1999, 121 (35), 8044-8051.
49. Pääbo, S.; Poinar, H.; Serre, D.; Jaenicke-Després, V.; Hebler, J.; Rohland, N.; Kuch, M.; Krause, J.; Vigilant, L.; Hofreiter, M., GENETIC ANALYSES FROM ANCIENT DNA. *Annual Review of Genetics* 2004, 38 (1), 645-679.
50. Boozer, C.; Ladd, J.; Chen, S.; Jiang, S., DNA-directed protein immobilization for simultaneous detection of multiple analytes by surface plasmon resonance biosensor. *Analytical Chemistry* 2006, 78 (5), 1515-1519.
51. Jung, Y.; Lee, J. M.; Jung, H.; Chung, B. H., Self-directed and self-oriented immobilization of antibody by protein G-DNA conjugate. *Analytical chemistry* 2007, 79 (17), 6534-6541.
52. Harder, P.; Grunze, M.; Dahint, R.; Whitesides, G. M.; Laibinis, P. E., Molecular Conformation in Oligo(ethylene glycol)-Terminated Self-Assembled Monolayers on Gold and Silver Surfaces Determines Their Ability To Resist Protein Adsorption. *The Journal of Physical Chemistry B* 1998, 102 (2), 426-436.

53. Khan, M. N.; Tjong, V.; Chilkoti, A.; Zharnikov, M., Fabrication of ssDNA/Oligo(ethylene glycol) Monolayers and Complex Nanostructures by an Irradiation-Promoted Exchange Reaction. *Angewandte Chemie International Edition* 2012, *51* (41), 10303-10306.
54. Petrovykh, D. Y.; Perez-Dieste, V.; Opdahl, A.; Kimura-Suda, H.; Sullivan, J. M.; Tarlov, M. J.; Himpel, F. J.; Whitman, L. J., Nucleobase orientation and ordering in films of single-stranded DNA on gold. *J Am Chem Soc* 2006, *128* (1), 2-3.
55. Opdahl, A.; Petrovykh, D. Y.; Kimura-Suda, H.; Tarlov, M. J.; Whitman, L. J., Independent control of grafting density and conformation of single-stranded DNA brushes. *Proc Natl Acad Sci U S A* 2007, *104* (1), 9-14.
56. Ballav, N.; Koelsch, P.; Zharnikov, M., Orientation and Ordering in Monomolecular Films of Sulfur-Modified Homo-oligonucleotides on Gold. *The Journal of Physical Chemistry C* 2009, *113* (42), 18312-18320.
57. Schreiner, S. M.; Hatch, A. L.; Shudy, D. F.; Howard, D. R.; Howell, C.; Zhao, J.; Koelsch, P.; Zharnikov, M.; Petrovykh, D. Y.; Opdahl, A., Impact of DNA-Surface Interactions on the Stability of DNA Hybrids. *Analytical Chemistry* 2011, *83* (11), 4288-4295.
58. Petrovykh, D. Y.; Kimura-Suda, H.; Tarlov, M. J.; Whitman, L. J., Quantitative Characterization of DNA Films by X-ray Photoelectron Spectroscopy. *Langmuir* 2004, *20* (2), 429-440.
59. Ballav, N.; Thomas, H.; Winkler, T.; Terfort, A.; Zharnikov, M., Making Protein Patterns by Writing in a Protein-Repelling Matrix. *Angewandte Chemie International Edition* 2009, *48* (32), 5833-5836.
60. Ballav, N.; Terfort, A.; Zharnikov, M., Making Gradient Patterns by Electron Beam Chemical Lithography with Monomolecular Resists. In *Soft matter gradient surfaces: Methods & applications*, Genzer, J., Ed. Wiley-VCH: Weinheim, Germany, 2012; pp 199-228.
61. Jeyachandran, Y. L.; Weber, T.; Terfort, A.; Zharnikov, M., Application of Long Wavelength Ultraviolet Radiation for Modification and Patterning of Protein-Repelling Monolayers. *The Journal of Physical Chemistry C* 2013, *117* (11), 5824-5830.
62. Montague, M.; Ducker, R. E.; Chong, K. S. L.; Manning, R. J.; Rutten, F. J. M.; Davies, M. C.; Leggett, G. J., Fabrication of Biomolecular Nanostructures by Scanning Near-Field Photolithography of Oligo(ethylene glycol)-Terminated Self-Assembled Monolayers. *Langmuir* 2007, *23* (13), 7328-7337.
63. Ducker, R. E.; Janusz, S.; Sun, S.; Leggett, G. J., One-Step Photochemical Introduction of Nanopatterned Protein-Binding Functionalities to Oligo(ethylene glycol)-Terminated Self-Assembled Monolayers. *Journal of the American Chemical Society* 2007, *129* (48), 14842-14843.
64. Adams, J.; Tizazu, G.; Janusz, S.; Brueck, S. R. J.; Lopez, G. P.; Leggett, G. J., Large-Area Nanopatterning of Self-Assembled Monolayers of Alkanethiolates by Interferometric Lithography. *Langmuir* 2010, *26* (16), 13600-13606.

65. Hutt, D. A.; Cooper, E.; Leggett, G. J., Structure and Mechanism of Photooxidation of Self-assembled Monolayers of Alkylthiols on Silver Studied by XPS and Static SIMS. *The Journal of Physical Chemistry B* 1998, *102* (1), 174-184.
66. Rieley, H.; Kendall, G. K.; Zemicael, F. W.; Smith, T. L.; Yang, S., X-ray Studies of Self-Assembled Monolayers on Coinage Metals. 1. Alignment and Photooxidation in 1,8-Octanedithiol and 1-Octanethiol on Au. *Langmuir* 1998, *14* (18), 5147-5153.
67. Ballav, N.; Weidner, T.; Zharnikov, M., UV-Promoted Exchange Reaction as a Tool for Gradual Tuning the Composition of Binary Self-Assembled Monolayers and Chemical Lithography. *The Journal of Physical Chemistry C* 2007, *111* (32), 12002-12010.
68. Leggett, G. J., Scanning near-field photolithography-surface photochemistry with nanoscale spatial resolution. *Chemical Society Reviews* 2006, *35* (11), 1150-1161.
69. Haq, E. u.; Liu, Z.; Zhang, Y.; Ahmad, S. A. A.; Wong, L.-S.; Armes, S. P.; Hobbs, J. K.; Leggett, G. J.; Micklefield, J.; Roberts, C. J.; Weaver, J. M. R., Parallel Scanning Near-Field Photolithography: The Snomipede. *Nano Lett* 2010, *10* (11), 4375-4380.
70. Chen, S.; Smith, L. M., Photopatterned Thiol Surfaces for Biomolecule Immobilization. *Langmuir* 2009, *25* (20), 12275-12282.
71. Waldbaur, A.; Waterkotte, B.; Schmitz, K.; Rapp, B. E., Maskless Projection Lithography for the Fast and Flexible Generation of Grayscale Protein Patterns. *Small* 2012, *8* (10), 1570-1578.
72. Chow, D. C.; Chilkoti, A., Surface-Initiated Enzymatic Polymerization of DNA. *Langmuir* 2007, *23* (23), 11712-11717.
73. Chow, D. C.; Lee, W.-K.; Zauscher, S.; Chilkoti, A., Enzymatic Fabrication of DNA Nanostructures: Extension of a Self-assembled Oligonucleotide Monolayer on Gold Arrays. *Journal of the American Chemical Society* 2005, *127* (41), 14122-14123.
74. Tjong, V.; Yu, H.; Hucknall, A.; Rangarajan, S.; Chilkoti, A., Amplified On-Chip Fluorescence Detection of DNA Hybridization by Surface-Initiated Enzymatic Polymerization. *Analytical Chemistry* 2011, *83* (13), 5153-5159.
75. Howell, C.; Hamoudi, H.; Zharnikov, M., Thymine/adenine diblock-oligonucleotide monolayers and hybrid brushes on gold: a spectroscopic study. *Biointerphases* 2013, *8* (1), 6.
76. Howell, C.; Jeyachandran, Y. L.; Koelsch, P.; Zharnikov, M., Orientation and Ordering in Sequence- and Length-Mismatched Surface-Bound DNA Hybrids. *The Journal of Physical Chemistry C* 2012, *116* (20), 11133-11140.
77. Howell, C.; Hamoudi, H.; Heissler, S.; Koelsch, P.; Zharnikov, M., Orientation changes in surface-bound hybridized DNA undergoing preparation for ex situ spectroscopic measurements. *Chemical Physics Letters* 2011, *513* (4-6), 267-270.
78. Howell, C.; Zhao, J.; Koelsch, P.; Zharnikov, M., Hybridization in ssDNA films--a multi-technique spectroscopy study. *Physical chemistry chemical physics : PCCP* 2011, *13* (34), 15512-15522.

79. Saprigin, A. V.; Thomas, C. W.; Dulcey, C. S.; Patterson, C. H.; Spector, M. S., Spectroscopic quantification of covalently immobilized oligonucleotides. *Surf Interface Anal* 2004, *37* (1), 24-32.
80. Gaines, G. L., In *Insoluble Monolayers at Liquid-Gas Interfaces*, Interscience Publishers: New York, 1966.
81. Whitesides, G. M.; Mathias, J. P.; Seto, C. T., Molecular self-assembly and nanochemistry: a chemical strategy for the synthesis of nanostructures. *Science* 1991, *254* (5036), 1312-9.
82. Nuzzo, R. G.; Allara, D. L., Adsorption of bifunctional organic disulfides on gold surfaces. *Journal of the American Chemical Society*, 1983, *105* (13), 4481-4483.
83. Ulman, A., Formation and Structure of Self-Assembled Monolayers. *Chem Rev* 1996, *96* (4), 1533-1554.
84. Jaschke, M.; Schönherr, H.; Wolf, H.; Butt, H. J.; Bamberg, E.; Besocke, M. K.; Ringsdorf, H., Structure of Alkyl and Perfluoroalkyl Disulfide and Azobenzenthiole Monolayers on Gold(111) Revealed by Atomic Force Microscopy. *The Journal of Physical Chemistry* 1996, *100* (6), 2290-2301.
85. Liu, G.-y.; Salmeron, M. B., Reversible Displacement of Chemisorbed n-Alkanethiol Molecules on Au(111) Surface: An Atomic Force Microscopy Study. *Langmuir* 1994, *10* (2), 367-370.
86. Nuzzo, R. G.; Zegarski, B. R.; Dubois, L. H., Fundamental studies of the chemisorption of organosulfur compounds on gold(111). Implications for molecular self-assembly on gold surfaces. *Journal of the American Chemical Society* 1987, *109* (3), 733-740.
87. Khan, M. N.; Zharnikov, M., Irradiation Promoted Exchange Reaction with Disulfide Substituents. *J Phys Chem C* 2013, *117* (28), 14534-14543.
88. Dubois, L. H.; Nuzzo, R. G., Synthesis, Structure, and Properties of Model Organic Surfaces. *Annu Rev Phys Chem* 1992, *43* (1), 437-463.
89. Sellers, H.; Ulman, A.; Shnidman, Y.; Eilers, J. E., Structure and binding of alkanethiolates on gold and silver surfaces: implications for self-assembled monolayers. *Journal of the American Chemical Society* 1993, *115* (21), 9389-9401.
90. Bain, C. D.; Whitesides, G. M., Modeling Organic Surfaces with Self-Assembled Monolayers. *Angewandte Chemie International Edition in English* 1989, *28* (4), 506-512.
91. Hähner, G.; Kinzler, M.; Thümmel, C.; Wöll, C.; Grunze, M., Structure of self-organizing organic films: A near edge x-ray absorption fine structure investigation of thiol layers adsorbed on gold. *Journal of Vacuum Science & Technology A* 1992, *10* (4), 2758-2763.
92. Poirier, G. E.; Tarlov, M. J., The c(4X2) Superlattice of n-Alkanethiol Monolayers Self-Assembled on Au(111). *Langmuir* 1994, *10* (9), 2853-2856.
93. Kind, M.; Woll, C., Organic surfaces exposed by self-assembled organothiol monolayers: Preparation, characterization, and application. *Prog Surf Sci* 2009, *84* (7-8), 230-278.

94. Camillone, N.; Chidsey, C. E. D.; Liu, G. y.; Scoles, G., Superlattice structure at the surface of a monolayer of octadecanethiol self-assembled on Au(111). *The Journal of Chemical Physics* 1993, *98* (4), 3503-3511.
95. Laibinis, P. E.; Whitesides, G. M.; Allara, D. L.; Tao, Y. T.; Parikh, A. N.; Nuzzo, R. G., Comparison of the structures and wetting properties of self-assembled monolayers of n-alkanethiols on the coinage metal surfaces, copper, silver, and gold. *Journal of the American Chemical Society* 1991, *113* (19), 7152-7167.
96. Himmelhaus, M.; Gauss, I.; Buck, M.; Eisert, F.; Wöll, C.; Grunze, M., Adsorption of docosanethiol from solution on polycrystalline silver surfaces: an XPS and NEXAFS study. *Journal of Electron Spectroscopy and Related Phenomena* 1998, *92* (1-3), 139-149.
97. Alexiadis, O.; Harmandaris, V. A.; Mavrantzas, V. G.; Site, L. D., Atomistic Simulation of Alkanethiol Self-Assembled Monolayers on Different Metal Surfaces via a Quantum, First-Principles Parametrization of the Sulfur-Metal Interaction. *The Journal of Physical Chemistry C* 2007, *111* (17), 6380-6391.
98. Allara, D., Self-Assembled Molecular Films as Polymer Surface Models In *Polymer Surfaces and Interfaces II*, Feast, W. J.; Munro, H. S.; Richards, R. W., Eds. Wiley & Sons: 1993.
99. Prime, K. L.; Whitesides, G. M., Adsorption of Proteins onto Surfaces Containing End-Attached Oligo(ethylene oxide): A Model System Using Self-Assembled Monolayers. *J Am Chem Soc* 1993, *115*, 10714-10721.
100. Bain, C. D.; Troughton, E. B.; Tao, Y.-T.; Evall, J.; Whitesides, G. M.; Nuzzo, R. G., Formation of Monolayer Films by the Spontaneous Assembly of Organic Thiols from Solution onto Gold. *J Am Chem Soc* 1989, *111*, 321-335.
101. Bain, C. D.; Whitesides, G. M., Formation of two-component surfaces by the spontaneous assembly of monolayers on gold from solutions containing mixtures of organic thiols. *J. Am. Chem. Soc.* 1988, *110* (19), 6560-1.
102. Tamada, K.; Hara, M.; Sasabe, H.; Knoll, W., Surface Phase Behavior of n-Alkanethiol Self-Assembled Monolayers Adsorbed on Au(111): An Atomic Force Microscope Study. *Langmuir* 1997, *13* (6), 1558-1566.
103. Troughton, E. B.; Bain, C. D.; Whitesides, G. M.; Nuzzo, R. G.; Allara, D. L.; Porter, M. D., Monolayer films prepared by the spontaneous self-assembly of symmetrical and unsymmetrical dialkyl sulfides from solution onto gold substrates: structure, properties, and reactivity of constituent functional groups. *Langmuir* 1988, *4* (2), 365-85.
104. Smith, R. K.; Lewis, P. A.; Weiss, P. S., Patterning self-assembled monolayers. *Prog Surf Sci* 2004, *75* (1-2), 1-68.
105. Kumar, A.; Whitesides, G. M., Patterned condensation figures as optical diffraction gratings. *Science* 1994, *263* (5143), 60-62.

106. Chou, S. Y.; Krauss, P. R.; Renstrom, P. J., Nanoimprint lithography. *Journal of Vacuum Science Technology B* 1996, *14* (6), 4129-4133.
107. Guo, L. J., Nanoimprint lithography: Methods and material requirements. *Advanced Materials* 2007, *19* (4), 495-513.
108. de Gans, B. J.; Duineveld, P. C.; Schubert, U. S., Inkjet printing of polymers: State of the art and future developments. *Advanced Materials* 2004, *16* (3), 203-213.
109. Bardea, A.; Naaman, R., Submicrometer Chemical Patterning with High Throughput Using Magnetolithography. *Langmuir* 2009, *25* (10), 5451-5454.
110. Kumar, T. A.; Bardea, A.; Shai, Y.; Yoffe, A.; Naaman, R., Patterning Gradient Properties from Sub-Micrometers to Millimeters by Magnetolithography. *Nano Lett* 2010, *10* (6), 2262-2267.
111. Ito, T.; Okazaki, S., Pushing the limits of lithography. *Nature* 2000, *406* (6799), 1027-31.
112. Lopez, G. P.; Biebuyck, H. A.; Whitesides, G. M., Scanning electron microscopy can form images of patterns in self-assembled monolayers. *Langmuir* 1993, *9* (6), 1513-1516.
113. Vieu, C.; Carcenac, F.; Pepin, A.; Chen, Y.; Mejias, M.; Lebib, A.; Manin-Ferlazzo, L.; Couraud, L.; Launois, H., Electron beam lithography: resolution limits and applications. *Applied Surface Science* 2000, *164* (1-4), 111-117.
114. Kubena, R. L.; Ward, J. W.; Stratton, F. P.; Joyce, R. J.; Atkinson, G. M., A Low Magnification Focused Ion-Beam System with 8 Nm Spot Size. *J Vac Sci Technol B* 1991, *9* (6), 3079-3083.
115. Glass, R.; Arnold, M.; Blummel, J.; Kuller, A.; Moller, M.; Spatz, J. P., Micro-nanostructured interfaces fabricated by the use of inorganic block copolymer micellar monolayers as negative resist for electron-beam lithography. *Advanced Functional Materials* 2003, *13* (7), 569-575.
116. Liu, J.-F.; Cruchon-Dupeyrat, S.; Garno, J. C.; Frommer, J.; Liu, G.-Y., Three-Dimensional Nanostructure Construction via Nanografting: Positive and Negative Pattern Transfer. *Nano Lett* 2002, *2* (9), 937-940.
117. Xu, S.; Miller, S.; Laibinis, P. E.; Liu, G., Fabrication of nanometer scale patterns within self-assembled monolayers by nanografting. *Langmuir* 2002, *15* (21), 937-940.
118. Kleineberg, U.; Brechling, A.; Sundermann, M.; Heinzmann, U., STM lithography in an organic self-assembled monolayer. *Advanced Functional Materials* 2001, *11* (3), 208-212.
119. Ehrfeld, W.; Lehr, H., Deep x-ray lithography for the production of three-dimensional microstructures from metals, polymers and ceramics. *Radiation Physics and Chemistry*, 1995, *45* (3), 349-365.
120. Piner, R. D.; Zhu, J.; Xu, F.; Hong, S.; Mirkin, C. A., "Dip-Pen" nanolithography. *Science* 1999, *283* (5402), 661-3.

121. Hidber, P. C.; Helbig, W.; Kim, E.; Whitesides, G. M., Microcontact printing of palladium colloids: Micron-scale patterning by electroless deposition of copper. *Langmuir* 1996, *12* (5), 1375-1380.
122. Xia, Y. N.; Whitesides, G. M., Soft lithography. *Angew Chem Int Edit* 1998, *37* (5), 551-575.
123. Ruiz, S. A.; Chen, C. S., Microcontact printing: A tool to pattern. *Soft Matter* 2007, *3* (2), 168-177.
124. Götzhäuser, A.; Eck, W.; Geyer, W.; Stadler, V.; Weimann, T.; Hinze, P.; Grunze, M., Chemical Nanolithography with Electron Beams. *Advanced Materials* 2001, *13* (11), 803-806.
125. Henzler, M.; Göpel, W., Oberflächenphysik des Festkörpers. Vieweg & Teubner Verlag: 1994.
126. Eck, W.; Stadler, V.; Geyer, W.; Zharnikov, M.; Götzhäuser, A.; Grunze, M., Generation of Surface Amino Groups on Aromatic Self-Assembled Monolayers by Low Energy Electron Beams— A First Step Towards Chemical Lithography. *Advanced Materials* 2000, *12* (11), 805-808.
127. Geyer, W.; Stadler, V.; Eck, W.; Zharnikov, M.; Golzhauser, A.; Grunze, M., Electron-induced crosslinking of aromatic self-assembled monolayers: Negative resists for nanolithography. *Applied Physics Letters* 1999, *75* (16), 2401-2403.
128. Zharnikov, M.; Grunze, M., Modification of thiol-derived self-assembling monolayers by electron and x-ray irradiation: Scientific and lithographic aspects. *Journal of Vacuum Science & Technology B: Microelectronics and Nanometer Structures* 2002, *20* (5), 1793-1807.
129. Heister, K.; Zharnikov, M.; Grunze, M.; Johansson, L. S. O.; Ulman, A., Characterization of X-ray Induced Damage in Alkanethiolate Monolayers by High-Resolution Photoelectron Spectroscopy. *Langmuir* 2000, *17* (1), 8-11.
130. Zhou, F.; Shu, W.; Welland, M. E.; Huck, W. T., Highly reversible and multi-stage cantilever actuation driven by polyelectrolyte brushes. *Journal of the American Chemical Society* 2006, *128* (16), 5326-5327.
131. Ryan, A.; Crook, C.; Howse, J.; Topham, P.; Jones, R.; Geoghegan, M.; Parnell, A.; Ruiz-Perez, L.; Martin, S.; Cadby, A., Responsive brushes and gels as components of soft nanotechnology. *Faraday discussions* 2005, *128*, 55-74.
132. Feng, W.; Zhu, S.; Ishihara, K.; Brash, J. L., Adsorption of fibrinogen and lysozyme on silicon grafted with poly (2-methacryloyloxyethyl phosphorylcholine) via surface-initiated atom transfer radical polymerization. *Langmuir* 2005, *21* (13), 5980-5987.
133. Ballav, N.; Weidner, T.; Zharnikov, M., UV-Promoted Exchange Reaction as a Tool for Gradual Tuning the Composition of Binary Self-Assembled Monolayers and Chemical Lithography. *J. Phys. Chem. C* 2007, *111* (32), 12002-12010.
134. Barbey, R.; Lavanant, L.; Paripovic, D.; Schüwer, N.; Sugnaux, C.; Tugulu, S.; Klok, H.-A., Polymer Brushes via Surface-Initiated Controlled Radical Polymerization: Synthesis, Characterization, Properties, and Applications. *Chem Rev* 2009, *109* (11), 5437-5527.

135. England, R. M.; Rimmer, S., Hyper/highly-branched polymers by radical polymerisations. *Polym Chem-Uk* 2010, *1* (10), 1533-1544.
136. Solomon, D.; Rizzardo, E.; Cacioli, P., US Patent 4,581,-429. *P. Eur. Pat. Appl* 1985, 135280.
137. Matyjaszewski, K.; Wang, J.-S., (Co) polymers and a novel polymerization process based on atom (or group) transfer radical polymerization. Google Patents: 1998.
138. Jones, D. M.; Brown, A. A.; Huck, W. T. S., Surface-Initiated Polymerizations in Aqueous Media: Effect of Initiator Density. *Langmuir* 2002, *18* (4), 1265-1269.
139. Kamigaito, M.; Ando, T.; Sawamoto, M., Metal-catalyzed living radical polymerization. *Chem Rev* 2001, *101* (12), 3689-3745.
140. Matyjaszewski, K.; Miller, P. J.; Shukla, N.; Immaraporn, B.; Gelman, A.; Luokala, B. B.; Siclovan, T. M.; Kickelbick, G.; Vallant, T.; Hoffmann, H.; Pakula, T., Polymers at Interfaces: Using Atom Transfer Radical Polymerization in the Controlled Growth of Homopolymers and Block Copolymers from Silicon Surfaces in the Absence of Untethered Sacrificial Initiator. *Macromolecules* 1999, *32* (26), 8716-8724.
141. Huang, W.; Kim, J.-B.; Bruening, M. L.; Baker, G. L., Functionalization of Surfaces by Water-Accelerated Atom-Transfer Radical Polymerization of Hydroxyethyl Methacrylate and Subsequent Derivatization. *Macromolecules* 2002, *35* (4), 1175-1179.
142. Wenxi Huang, G. L. B., and Merlin L. Bruening, Controlled Synthesis of Cross-Linked Ultrathin Polymer Films by Using Surface-Initiated Atom Transfer Radical Polymerization. *Angew. Chem.* 2001, (133), 1558-1560.
143. Bollum, F.; Setlow, R., Ultraviolet inactivation of DNA primer activity: I. Effects of different wavelengths and doses. *Biochimica et Biophysica Acta (BBA)-Specialized Section on Nucleic Acids and Related Subjects* 1963, *68*, 599-607.
144. Kato, K.; Goncalves, J. M.; Houts, G. E.; Bollum, F. J., Deoxynucleotide-polymerizing Enzymes of Calf Thymus Gland: II. PROPERTIES OF THE TERMINAL DEOXYNUCLEOTIDYLTRANSFERASE. *Journal of Biological Chemistry* 1967, *242* (11), 2780-2789.
145. Deng, G.-r.; Wu, R., An improved procedure for utilizing terminal transferase to add homopolymers to the 3' termini of DNA. *Nucleic acids research* 1981, *9* (16), 4173-4188.
146. Buddy Ratner; Castner, D., Electron Spectroscopy for Chemical Analysis. In *Surface Analysis: The Principal Techniques*, John C. Vickerman; Wilson, R., Eds. John Wiley & Sons: 1997.
147. Fitzpatrick, L. E., *Materials Characterization Series*. Manning Publications Co.: Greenwich, 1992.
148. Stöhr, J., NEXAFS Spectroscopy. Springer-Verlag: Berlin, 1992.
149. Bachrach, R. Z., In *Synchrotron Radiation Research Advances in Surface and Interface Science*, Plenum press: New York, 1992.

150. Tompkins, H. G., In *A User's Guide to Ellipsometry*, Academic Press Inc: San Diego, CA, 2006.
151. Fujiwara., H., In *Spectroscopic Ellipsometry: Principles and Applications*, Wiley & Sons: 2007.
152. Woollam, J. A., Light & Materials - Part 1. <http://www.jawoollam.com/tutorial2.html> access on 15-12-2013.
153. Bordo, V. G.; Rubahn., H. G., In *Optics and Spectroscopy at Surfaces and Interfaces*, Wiley & Sons: 2008.
154. Goldstein., D. H., Polarized Light. In *Optical Engineering Series* [Online] Dekker, M., Ed. 2003.
155. Singh, J., Optical Properties of Condensed Matter and Applications. In *Wiley Series in Materials for Electronic & Optoelectronic Applications*, Wiley & Sons: 2006.
156. Stokes., D., In *Principles and Practice of Variable Pressure: Environmental Scanning Electron Microscopy (VP-ESEM)*. RMS - Royal Microscopical Society. Wiley & Sons: 2008.
157. Egerton, R. F., An introduction to microscopy. In *Physical Principles of Electron Microscopy*, Springer US, 2005.
158. R. Winter, F. N., and C. Czeslik., In *Methoden der Biophysikalischen Chemie.*, Vieweg & Teubner Verlag: 2011.
159. Walther, P., Das Rasterelektronenmikroskop (REM). <http://www.uni-ulm.de/elektronenmikroskopie/2003REM.htm>, access 15.12.2013.: 2008.
160. Binnig, G.; Rohrer, H.; Gerber, C.; Weibel, E., Tunneling through a controllable vacuum gap. *Applied Physics Letters* 1982, 40 (2), 178-180.
161. Binnig, G.; Rohrer, H.; Gerber, C.; Weibel, E., Surface Studies by Scanning Tunneling Microscopy. *Physical Review Letters* 1982, 49 (1), 57-61.
162. Binnig, G.; Quate, C. F.; Gerber, C., Atomic Force Microscope. *Physical Review Letters* 1986, 56 (9), 930-933.
163. Bhushan, B., Part B Scanning probe microscopy. In *Springer Handbook of Nanotechnology*, Springer: 2010.
164. Braet, F.; De Zanger, R.; Kämmer, S.; Wisse, E., Noncontact versus contact imaging: An atomic force microscopic study on hepatic endothelial cells in vitro. *International Journal of Imaging Systems and Technology* 1997, 8 (2), 162-167.
165. Binnig, G.; Quate, C. F.; Gerber, C., Atomic force microscope. *Phys Rev Lett* 1986, 56 (9), 930-933.
166. Hölscher, H.; Schwarz, U. D.; Wiesendanger, R., Calculation of the frequency shift in dynamic force microscopy. *Applied Surface Science* 1999, 140 (3-4), 344-351.

167. Magonov, S. N.; Elings, V.; Whangbo, M. H., Phase imaging and stiffness in tapping-mode atomic force microscopy. *Surf Sci* 1997, 375 (2–3), L385-L391.
168. Friedbacher, G.; Fuchs, H., Classification of scanning probe microscopies - (Technical report). *Pure and Applied Chemistry* 1999, 71 (7), 1337-1357.
169. W. A. Z., Relation of the Equilibrium Contact Angle to Liquid and Solid Constitution. In *Contact Angle, Wettability, and Adhesion*, ACS: 1964; Vol. 43, pp 1-51.
170. Dubois, L. H.; Nuzzo, R. G., Synthesis, structure, and properties of model organic surfaces. *Annual Review of Physical Chemistry*, 1992, 43 (1), 437–463.
171. Gennes., P. G. d., Wetting: statics and dynamics. *Review of Modern Physics* 1985, 57 (3), 827–863.
172. Young, T., An essay on the cohesion of fluids. *Philosophical Transactions of the Royal Society of London*, 1805, 95, 65–87.
173. Genzer, J.; Efimenko, K., Recent developments in superhydrophobic surfaces and their relevance to marine fouling: a review. *Biofouling* 2006, 22 (5), 339–360.
174. Wenzel., R. N., Resistance of solid surfaces to wetting by water. *Industrial & Engineering Chemistry*, 1936, 28 (8), 988–994.
175. Cassie, A. B. D.; Baxter, S., Wettability of porous surfaces. *Transactions of the Faraday Society* 1944, 40, 546–551.
176. Storhoff, J. J.; Mirkin, C. A., What Controls the Optical Properties of DNA-linked Gold Nanoparticle Assemblies? *Chem. Rev.* 1999, 99, 1849–1862.
177. Seeman, N. C., Nanomaterials based on DNA. *Annual review of biochemistry* 2010, 79, 65-87.
178. Singh, V.; Zharnikov, M.; Gulino, A.; Gupta, T., DNA immobilization, delivery and cleavage on solid supports. *Journal of Materials Chemistry* 2011, 21 (29), 10602-10618.
179. Boozer, C.; Chen, S.; Jiang, S., Controlling DNA Orientation on Mixed ssDNA/OEG SAMs. *Langmuir* 2006, 22 (10), 4694-4698.
180. Herne, T. M.; Tarlov, M. J., Characterization of DNA Probes Immobilized on Gold Surfaces. *Journal of the American Chemical Society* 1997, 119 (38), 8916-8920.
181. Gong, P.; Lee, C.-Y.; Gamble, L. J.; Castner, D. G.; Grainger, D. W., Hybridization Behavior of Mixed DNA/Alkylthiol Monolayers on Gold: Characterization by Surface Plasmon Resonance and 32P Radiometric Assay. *Analytical Chemistry* 2006, 78 (10), 3326-3334.
182. Kick, A.; Bönsch, M.; Kummer, K.; Vyalikh, D. V.; Molodtsov, S. L.; Mertig, M., Controlling structural properties of self-assembled oligonucleotide–mercaptohexanol monolayers. *Journal of Electron Spectroscopy and Related Phenomena* 2009, 172 (1–3), 36-41.

183. Steel, A. B.; Levicky, R. L.; Herne, T. M.; Tarlov, M. J., Immobilization of Nucleic Acids at Solid Surfaces: Effect of Oligonucleotide Length on Layer Assembly. *Biophysical Journal* 2000, *79* (2), 975-981.
184. Lee, C.-Y.; Gong, P.; Harbers, G. M.; Grainger, D. W.; Castner, D. G.; Gamble, L. J., Surface Coverage and Structure of Mixed DNA/Alkylthiol Monolayers on Gold: Characterization by XPS, NEXAFS, and Fluorescence Intensity Measurements. *Analytical Chemistry* 2006, *78* (10), 3316-3325.
185. Chen, W. Y.; Hu, W. P.; Su, Y. D.; Taylor, A.; Jiang, S.; Chang, G. L., A multispot DNA chip fabricated with mixed ssDNA/oligo (ethylene glycol) self-assembled monolayers for detecting the effect of secondary structures on hybridization by SPR imaging. *Sensors and Actuators B: Chemical* 2007, *125* (2), 607-614.
186. Bamdad, C., A DNA Self-Assembled Monolayer for the Specific Attachment of Unmodified Double- or Single-Stranded DNA. *Biophysical Journal* 1998, *75* (4), 1997-2003.
187. Zhang, X.; Yadavalli, V. K., Surface immobilization of DNA aptamers for biosensing and protein interaction analysis. *Biosensors and Bioelectronics* 2011, *26* (7), 3142-3147.
188. Nagasaki, Y., Construction of a densely poly(ethylene glycol)-chain-tethered surface and its performance. *Polym J* 2011, *43* (12), 949-958.
189. Hu, W.-P.; Huang, L.-Y.; Kuo, T.-C.; Hu, W.-W.; Chang, Y.; Chen, C.-S.; Chen, H.-C.; Chen, W.-Y., Optimization of DNA-directed immobilization on mixed oligo(ethylene glycol) monolayers for immunodetection. *Analytical Biochemistry* 2012, *423* (1), 26-35.
190. Ladd, J.; Taylor, A. D.; Piliarik, M.; Homola, J.; Jiang, S., Hybrid Surface Platform for the Simultaneous Detection of Proteins and DNAs Using a Surface Plasmon Resonance Imaging Sensor. *Analytical Chemistry* 2008, *80* (11), 4231-4236.
191. Schilp, S.; Rosenhahn, A.; Pettitt, M. E.; Bowen, J.; Callow, M. E.; Callow, J. A.; Grunze, M., Physicochemical Properties of (Ethylene Glycol)-Containing Self-Assembled Monolayers Relevant for Protein and Algal Cell Resistance. *Langmuir* 2009, *25* (17), 10077-10082.
192. Zubavichus, Y.; Shaporenko, A.; Korolkov, V.; Grunze, M.; Zharnikov, M., X-ray Absorption Spectroscopy of the Nucleotide Bases at the Carbon, Nitrogen, and Oxygen K-Edges. *The Journal of Physical Chemistry B* 2008, *112* (44), 13711-13716.
193. Zharnikov, M.; Frey, S.; Heister, K.; Grunze, M., An extension of the mean free path approach to X-ray absorption spectroscopy. *Journal of Electron Spectroscopy and Related Phenomena* 2002, *124* (1), 15-24.
194. Steenackers, M.; Küller, A.; Ballav, N.; Zharnikov, M.; Grunze, M.; Jordan, R., Morphology Control of Structured Polymer Brushes. *Small* 2007, *3* (10), 1764-1773.
195. Olsen, C.; Rowntree, P. A., Bond-selective dissociation of alkanethiol based self-assembled monolayers adsorbed on gold substrates, using low-energy electron beams. *The Journal of Chemical Physics* 1998, *108* (9), 3750-3764.

196. Huels, M. A.; Dugal, P.-C.; Sanche, L., Degradation of functionalized alkanethiolate monolayers by 0–18 eV electrons. *The Journal of Chemical Physics* 2003, *118* (24), 11168-11178.
197. Laibinis, P. E.; Whitesides, G. M., .omega.-Terminated alkanethiolate monolayers on surfaces of copper, silver, and gold have similar wettabilities. *Journal of the American Chemical Society* 1992, *114* (6), 1990-1995.
198. Liedberg, B.; Tengvall, P., Molecular Gradients of .omega.-Substituted Alkanethiols on Gold: Preparation and Characterization. *Langmuir* 1995, *11* (10), 3821-3827.
199. Flores, S. M.; Shaporenko, A.; Vavilala, C.; Butt, H.-J.; Schmittel, M.; Zharnikov, M.; Berger, R., Control of surface properties of self-assembled monolayers by tuning the degree of molecular asymmetry. *Surf Sci* 2006, *600* (14), 2847-2856.
200. Arnold, R.; Azzam, W.; Terfort, A.; Wöll, C., Preparation, Modification, and Crystallinity of Aliphatic and Aromatic Carboxylic Acid Terminated Self-Assembled Monolayers. *Langmuir* 2002, *18* (10), 3980-3992.
201. Hamoudi, H.; Chesneau, F.; Patze, C.; Zharnikov, M., Chain-Length-Dependent Branching of Irradiation-Induced Processes in Alkanethiolate Self-Assembled Monolayers. *The Journal of Physical Chemistry C* 2010, *115* (2), 534-541.
202. Müller, H. U.; Zharnikov, M.; Völkel, B.; Schertel, A.; Harder, P.; Grunze, M., Low-Energy Electron-Induced Damage in Hexadecanethiolate Monolayers. *The Journal of Physical Chemistry B* 1998, *102* (41), 7949-7959.
203. Chen, C. H.; Huang, M. L.; Wang, S. C.; Klauser, R.; Shaporenko, A.; Zharnikov, M., Exposure of Monomolecular Lithographic Patterns to Ambient: An X-ray Photoemission Spectromicroscopy Study. *The Journal of Physical Chemistry B* 2006, *110* (36), 17878-17883.
204. Ahn, S. J.; Kaholek, M.; Lee, W. K.; LaMattina, B.; LaBean, T. H.; Zauscher, S., Surface-Initiated Polymerization on Nanopatterns Fabricated by Electron-Beam Lithography. *Advanced Materials* 2004, *16* (23-24), 2141-2145.
205. Huang, W.; Baker, G. L.; Bruening, M. L., Controlled Synthesis of Cross-Linked Ultrathin Polymer Films by Using Surface-Initiated Atom Transfer Radical Polymerization. *Angewandte Chemie* 2001, *113* (8), 1558-1560.
206. Kaholek, M.; Lee, W.-K.; Ahn, S.-J.; Ma, H.; Caster, K. C.; LaMattina, B.; Zauscher, S., Stimulus-Responsive Poly(N-isopropylacrylamide) Brushes and Nanopatterns Prepared by Surface-Initiated Polymerization. *Chemistry of Materials* 2004, *16* (19), 3688-3696.
207. Plunkett, K. N.; Zhu, X.; Moore, J. S.; Leckband, D. E., PNIPAM Chain Collapse Depends on the Molecular Weight and Grafting Density. *Langmuir* 2006, *22* (9), 4259-4266.
208. Chen, T.; Zhang, J.; Chang, D. P.; Garcia, A.; Zauscher, S., Fabrication of Micropatterned Stimulus-Responsive Polymer-Brush 'Anemone'. *Advanced Materials* 2009, *21* (18), 1825-1829.
209. Chen, T.; Chang, D. P.; Jordan, R.; S, Z., Colloidal Lithography for Fabricating Patterned Polymer-Brush Microstructures. *Beilstein J. Nanotechnol* 2012, *3*, 397-403.

210. Olivier, A.; Meyer, F.; Raquez, J.-M.; Damman, P.; Dubois, P., Surface-initiated controlled polymerization as a convenient method for designing functional polymer brushes: From self-assembled monolayers to patterned surfaces. *Progress in Polymer Science* 2012, *37* (1), 157-181.
211. Vericat, C.; Vela, M. E.; Benitez, G.; Carro, P.; Salvarezza, R. C., Self-assembled monolayers of thiols and dithiols on gold: new challenges for a well-known system. *Chemical Society Reviews* 2010, *39* (5), 1805-1834.
212. Li, L.; Zhu, Y.; Li, B.; Gao, C., Fabrication of Thermoresponsive Polymer Gradients for Study of Cell Adhesion and Detachment. *Langmuir* 2008, *24* (23), 13632-13639.
213. Lee, W.-K.; Patra, M.; Linse, P.; Zauscher, S., Scaling Behavior of Nanopatterned Polymer Brushes. *Small* 2007, *3* (1), 63-66.
214. Kimura-Suda, H.; Petrovykh, D. Y.; Tarlov, M. J.; Whitman, L. J., Base-dependent competitive adsorption of single-stranded DNA on gold. *J Am Chem Soc* 2003, *125* (30), 9014-5.
215. Ratner, B. D.; Castner, D. G., Electron Spectroscopy for Chemical Analysis. In *Surface Analysis: The Principal Techniques*, Vickerman, J. C.; Gilmore, I. S., Eds. Wiley & Sons: Chichester, 2009; pp 43-98.
216. Khan, M. N.; Tjong, V.; Chilkoti, A.; Zharnikov, M., Spectroscopic Study of a DNA Brush Synthesized in Situ by Surface Initiated Enzymatic Polymerization. *The Journal of Physical Chemistry B* 2013, *117* (34), 9929-9938.
217. Petrovykh, D. Y.; Kimura-Suda, H.; Whitman, L. J.; Tarlov, M. J., Quantitative Analysis and Characterization of DNA Immobilized on Gold. *Journal of the American Chemical Society* 2003, *125* (17), 5219-5226.
218. Vilar, M. R.; Botelho do Rego, A. M.; Ferraria, A. M.; Jugnet, Y.; Nogue, C.; Peled, D.; Naaman, R., Interaction of self-assembled monolayers of DNA with electrons: HREELS and XPS studies. *The journal of physical chemistry. B* 2008, *112* (23), 6957-64.
219. Jeyachandran, Y. L.; Zharnikov, M., Fabrication of Protein Patterns on the Basis of Short-Chain Protein-Repelling Monolayers. *The Journal of Physical Chemistry C* 2013, *117* (6), 2920-2925.
220. Moulder, J. F.; Stickle, W. E.; Sobol, P. E.; Bomben, K. D., In *Handbook of X-ray Photoelectron Spectroscopy*, Chastian, J., Ed. Perkin Elmer Corp.: Eden Prairie, MN, 1992.
221. Zharnikov, M.; Grunze, M., Spectroscopic characterization of thiol-derived self-assembling monolayers. *Journal of Physics: Condensed Matter* 2001, *13* (49), 11333-11365.
222. Zharnikov, M., High-resolution X-ray photoelectron spectroscopy in studies of self-assembled organic monolayers. *Journal of Electron Spectroscopy and Related Phenomena* 2010, *178-179* (0), 380-393.
223. Zwahlen, M.; Herrwerth, S.; Eck, W.; Grunze, M.; Hähner, G., Conformational Order in Oligo(ethylene glycol)-Terminated Self-Assembled Monolayers on Gold Determined by Soft X-ray Absorption. *Langmuir* 2003, *19* (22), 9305-9310.

224. Zubavichus, Y.; Shaporenko, A.; Grunze, M.; Zharnikov, M., Is X-ray Absorption Spectroscopy Sensitive to the Amino Acid Composition of Functional Proteins? *The Journal of Physical Chemistry B* 2008, *112* (15), 4478-4480.
225. Meyerbröker, N.; Zharnikov, M., Modification and Patterning of Nanometer-Thin Poly(ethylene glycol) Films by Electron Irradiation. *ACS Applied Materials & Interfaces* 2013, *5* (11), 5129-5138.
226. May, C. J.; Canavan, H. E.; Castner, D. G., Quantitative X-ray Photoelectron Spectroscopy and Time-of-Flight Secondary Ion Mass Spectrometry Characterization of the Components in DNA. *Analytical Chemistry* 2004, *76* (4), 1114-1122.
227. Ptasinska, S.; Stypczyńska, A.; Nixon, T.; Mason, N. J.; Klyachko, D. V.; Sanche, L., X-ray induced damage in DNA monitored by X-ray photoelectron spectroscopy. *J Chem Phys* 2008, *129* (6), 065102.
228. Zubavichus, Y.; Shaporenko, A.; Grunze, M.; Zharnikov, M., Innershell Absorption Spectroscopy of Amino Acids at All Relevant Absorption Edges. *The Journal of Physical Chemistry A* 2005, *109* (32), 6998-7000.
229. Zubavichus, Y.; Shaporenko, A.; Grunze, M.; Zharnikov, M., NEXAFS Spectroscopy of Homopolypeptides at All Relevant Absorption Edges: Polyisoleucine, Polytyrosine, and Polyhistidine. *The Journal of Physical Chemistry B* 2007, *111* (33), 9803-9807.
230. Zubavichus, Y.; Shaporenko, A.; Grunze, M.; Zharnikov, M., NEXAFS spectroscopy of biological molecules: From amino acids to functional proteins. *Nuclear Instruments and Methods in Physics Research Section A: Accelerators, Spectrometers, Detectors and Associated Equipment* 2009, *603* (1-2), 111-114.
231. Kaznacheyev, K.; Osanna, A.; Jacobsen, C.; Plashkevych, O.; Vahtras, O.; Ågren; Carravetta, V.; Hitchcock, A. P., Innershell Absorption Spectroscopy of Amino Acids. *The Journal of Physical Chemistry A* 2002, *106* (13), 3153-3168.
232. Lamont, C. L. A.; Wilkes, J., Attenuation length of electrons in self-assembled monolayers of n-alkanethiols on gold. *Langmuir* 1999, *15* (6), 2037-2042.
233. Heister, K.; Zharnikov, M.; Grunze, M.; Johansson, L. S. O., Adsorption of Alkanethiols and Biphenylthiols on Au and Ag Substrates: A High-Resolution X-ray Photoelectron Spectroscopy Study. *The Journal of Physical Chemistry B* 2001, *105* (19), 4058-4061.
234. Zubavichus, Y.; Zharnikov, M.; Yang, Y.; Fuchs, O.; Heske, C.; Umbach, E.; Tzvetkov, G.; Netzer, F. P.; Grunze, M., Surface Chemistry of Ultrathin Films of Histidine on Gold As Probed by High-Resolution Synchrotron Photoemission. *The Journal of Physical Chemistry B* 2004, *109* (2), 884-891.
235. Zubavichus, Y.; Zharnikov, M.; Yang, Y.; Fuchs, O.; Umbach, E.; Heske, C.; Ulman, A.; Grunze, M., X-ray Photoelectron Spectroscopy and Near-Edge X-ray Absorption Fine Structure Study of Water Adsorption on Pyridine-Terminated Thiolate Self-Assembled Monolayers. *Langmuir* 2004, *20* (25), 11022-11029.

236. Samuel, N. T.; Lee, C. Y.; Gamble, L. J.; Fischer, D. A.; Castner, D. G., NEXAFS characterization of DNA components and molecular-orientation of surface-bound DNA oligomers. *Journal of Electron Spectroscopy and Related Phenomena* 2006, 152 (3), 134-142.
237. Köhn, F. Angle Dependent X-Ray Photoelectron Spectroscopy of Organic Monolayers on Gold Surfaces. Diploma Thesis, Universität Heidelberg, Heidelberg, Germany, 1998.
238. Yeh, J. J.; Lindau, I., Atomic subshell photoionization cross sections and asymmetry parameters: $1 \leq Z \leq 103$. *Atomic Data and Nuclear Data Tables* 1985, 32 (1), 1-155.
239. Jager, B.; Schurmann, H.; Muller, H. U.; Himmel, H. J.; Neumann, M.; Grunze, M.; Woll, C., X-ray and low energy electron induced damage in alkanethiolate monolayers on Au-substrates. *Phys Chem* 1997, 202, 263-272.
240. Wirde, M.; Gelius, U.; Dunbar, T.; Allara, D. L., Modification of self-assembled monolayers of alkanethiols on gold by ionizing radiation. *Nuclear Instruments and Methods in Physics Research Section B: Beam Interactions with Materials and Atoms* 1997, 131 (1-4), 245-251.
241. Nefedov, A.; Wöll, C., Advanced Applications of NEXAFS Spectroscopy for Functionalized Surfaces, in Surface Science Techniques. In *Springer Series in Surface Science*, Bracco, G.; Holst, B., Eds. Springer-Verlag: Berlin, Heidelberg, New York, Tokyo, 2013; Vol. 51, pp 277-306.
242. Weiss, K. Analysis of X-ray Absorption Fine Structure for Long Chain Alkanes in Ultrathin Films. Universität Heidelberg, Heidelberg, Germany, 1994.

Acknowledgement

First I would like to express my deepest gratitude and admiration to my supervisor Prof. apl Dr. Michael Zharnikov not only for excellent guidance, patience and encouragement to accomplish this research, but also for many opportunities to present my work at conferences and for scientific freedoms granted to me while writing this thesis.

I thank, Prof. Dr. Petra Tegeder for her willingness to examine this work.

I thank, Prof. Dr. Michael Grunze for the acceptance to the department of Applied Physical Chemistry.

A great appreciation goes to Prof. Dr. Ashutosh Chilkoti and his team member Vinalia Tjong for thoughtful discussions and combined experiments of SIEP.

I would like to thank also all the members of Zharnikov group and department, who contributed to the success of this work. In particular, these are:

My office fellow, Hao Lu for supports and sharing chemistry lab instruments with me. It should be mentioned quite explicitly about Anna Grab. Not only that, we have lunch and sports together but also a lots of useful tips in pursuing this work. Of course, I thank Thomas and Leo for introducing me with AFM instrument.

My heartiest thank goes to my office fellow Dr. Nikolaus Meyerbröcker for always inspiring discussions and stimulating evening's parties.

I thank Günther Meinsch for his prompt and competent repair of instruments related to this research and advice on many issues concerning electronics. I also thank Peter Jeschka for his solution to computer problems. Many thanks to George Albert for the realization of requests for the production of the fresh gold (111) wafer with 100 nm gold on silicon in short notice. I am grateful to Reinhold Jehle for the support in the lab as well as for the technical development and implementation of numerous special requests related to XPS and electron lithography.

I would like to recognize the contributions made by undergraduate and graduate students Carina Ammerlahn, Eric Sauter, Martin Kuhn and Silke Koser, whom I had supervised during the time of my thesis.

I would like to thank Svetlana Duchnay and Benjamin Scherke, who had always managed to support administrative work in a fraction of the time.

Finally, I would like to thank my parents and sister who have enabled me to perform these studies through their supports.

Financial Supports

- DAAD scholarship.
- DFG financial grant.
- Graduate academy teaching assistantship grant.

Ich erkläre hiermit, dass ich die vorgelegte Dissertation selbst verfasst und mich keiner anderen als der von mir ausdrücklich bezeichneten Quellen und Hilfen bedient habe.



Heidelberg, im Januar 2014 Md. Nuruzzaman Khan Hira

**Eidesstattliche Versicherung gemäß § 8 der Promotionsordnung
der Naturwissenschaftlich-Mathematischen Gesamtfakultät
der Universität Heidelberg**

1. Bei der eingereichten Dissertation zu dem Thema

CHEMICAL LITHOGRAPHY with
MONOMOLECULAR TEMPLATES

handelt es sich um meine eigenständig erbrachte Leistung.

2. Ich habe nur die angegebenen Quellen und Hilfsmittel benutzt und mich keiner unzulässigen Hilfe Dritter bedient. Insbesondere habe ich wörtlich oder sinngemäß aus anderen Werken übernommene Inhalte als solche kenntlich gemacht.

3. Die Arbeit oder Teile davon habe ich wie folgt/bislang nicht¹⁾ an einer Hochschule des In- oder Auslands als Bestandteil einer Prüfungs- oder Qualifikationsleistung vorgelegt.

Titel der Arbeit: _____

Hochschule und Jahr: _____

Art der Prüfungs- oder Qualifikationsleistung: _____

4. Die Richtigkeit der vorstehenden Erklärungen bestätige ich.

5. Die Bedeutung der eidesstattlichen Versicherung und die strafrechtlichen Folgen einer unrichtigen oder unvollständigen eidesstattlichen Versicherung sind mir bekannt.

Ich versichere an Eides statt, dass ich nach bestem Wissen die reine Wahrheit erklärt und nichts verschwiegen habe.

Heidelberg, 08.01.2014
Ort und Datum


Unterschrift

¹⁾ Nicht Zutreffendes streichen. Bei Bejahung sind anzugeben: der Titel der andernorts vorgelegten Arbeit, die Hochschule, das Jahr der Vorlage und die Art der Prüfungs- oder Qualifikationsleistung.